



Julia Hassler, BSc

**Study of point defects in proton implanted silicon pn-junctions by means of electrically detected magnetic resonance**

**MASTER'S THESIS**

to achieve the university degree of

Diplom-Ingenieurin

Master's degree programme: Advanced Materials Science

submitted to

**Graz University of Technology**

Supervisor

Univ.-Prof. Peter Hadley

Institute of Solid State Physics



## **EIDESSTATTLICHE ERKLÄRUNG**

### ***AFFIDAVIT***

Ich erkläre an Eides statt, dass ich die vorliegende Arbeit selbstständig verfasst, andere als die angegebenen Quellen/Hilfsmittel nicht benutzt, und die den benutzten Quellen wörtlich und inhaltlich entnommenen Stellen als solche kenntlich gemacht habe. Das in TUGRAZonline hochgeladene Textdokument ist mit der vorliegenden Masterarbeit/Diplomarbeit/Dissertation identisch.

*I declare that I have authored this thesis independently, that I have not used other than the declared sources/resources, and that I have explicitly indicated all material which has been quoted either literally or by content from the sources used. The text document uploaded to TUGRAZonline is identical to the present master's thesis/diploma thesis/doctoral dissertation.*

---

Datum / Date

---

Unterschrift / Signature



---

# Abstract

---

This master thesis deals with the investigation of point defects in proton implanted silicon pn-junctions to contribute to a better understanding of proton implantation related defects. Three different types of devices were investigated by means of electrically detected magnetic resonance (EDMR). Differences in the EDMR spectra of the implanted samples were observed in comparison to an unimplanted reference sample. The proton implantation evidently leads to an introduction of recombination centres in the pn-junctions. Moreover, changes in the EDMR responses depending on the implantation dose ( $10^{14}$  H<sup>+</sup>cm<sup>-2</sup> and  $10^{15}$  H<sup>+</sup>cm<sup>-2</sup>) as well as after the application of different annealing treatments were observed. In all investigated samples an isotropic EDMR signal (termed A) with a  $g$ -value of about 2.0055(3) was recorded. This EDMR response is most likely due to silicon dangling bonds at the surface that exist because of a missing edge termination. In the samples implanted with the higher dose, a doublet with a hyperfine splitting of 115 G and a  $g$ -value of 2.0093(4) was observed. The doublet signal disappeared at annealing temperatures higher than 400 °C and there is a strong suspicion that the underlying defect is hydrogen related.



---

# Kurzfassung

---

Diese Masterarbeit befasst sich mit der Untersuchung von Punktdefekten in protonenimplantierten Silizium pn-Übergängen. Ziel dieser Arbeit ist es, zu einem besseren Verständnis der durch diesen Implantationsprozess entstehenden Defekte beizutragen. Im Zuge dieser Arbeit wurden drei verschiedene Bauteile unter Anwendung der elektrisch detektierten Magnetresonanzmethode untersucht. Dabei können paramagnetische Punktdefekte, welche sich im mittleren Bereich der Bandlücke befinden, detektiert werden. Im Vergleich zu einer nicht implantierten Referenzprobe konnten in den implantierten Proben Unterschiede in den resultierenden Spektren detektiert werden. Durch die Protonenimplantation werden also offensichtlich Rekombinationszentren in den pn-Übergängen erzeugt. Des Weiteren konnten Unterschiede in den Spektren der untersuchten Proben je nach implantierter Dosis ( $10^{14} \text{ H}^+ \text{ cm}^{-2}$  bzw.  $10^{15} \text{ H}^+ \text{ cm}^{-2}$ ) sowie nach der Anwendung von verschiedenen Temperaturbehandlungen beobachtet werden. In allen untersuchten Bauteilen trat ein isotropes Signal (A genannt) mit einem Landé-Faktor von  $2.0055(3)$  auf. Dieses Signal ist auf ungesättigte Siliziumbindungen an den Oberflächen zurückzuführen, welche aufgrund von fehlenden Randabschlüssen existieren. In jenen Proben, welche mit einer hohen Dosis implantiert wurden, konnten zusätzlich zu Signal A weitere Signale beobachtet werden. Ein Doublet wurde detektiert mit einer Hyperfeinaufspaltung von 115 G und einem Landé-Faktor von  $2.0093(4)$ . Dieses Doublet Signal verschwindet bei Temperaturbehandlungen höher als  $400 \text{ }^\circ\text{C}$ . Der diesem Signal zugrunde liegende Defekt ist höchstwahrscheinlich wasserstoffkorreliert.



---

# Acknowledgement

---

Without the help of many people, this work would not have been possible. It is my pleasure to thank all of these people for their support.

First of all, I would like to thank my thesis advisor Univ.-Prof. Peter Hadley for guiding me through this thesis. The door to Prof. Hadley's office was always open whenever I ran into problems or had a question about my research or writing.

In addition, I owe great thanks to Gernot Gruber for sharing his expertise and experience with me and for supporting me with useful hints from far away.

I am deeply grateful to Martin Faccinelli for many interesting and informative discussions, for all his help and in particular, for his very useful advice.

I would also like to thank Robert Meszaros for being such a good colleague and for the great cooperation.

Moreover, I want to thank Prof. Roland Resel, Prof. Markus Koch and Prof. Leising for letting me use their scientific equipment and for the scientific support.

Surely do I want to thank my whole family, in particular my mum Ruth Hassler and my dad Adolf Astner, for always standing behind me and supporting me during my whole study and throughout my entire life.

Finally, I want to thank Philipp Wassermann for his love, patience and overall support during the last years and especially in the time of my master thesis.

This work has been performed in the project EPPL, co-funded by grants from Austria, Germany, The Netherlands, Italy, France, Portugal- ENIAC member States and the ENIAC Joint Undertaking. The samples investigated in this thesis were provided by Infineon Technologies Austria AG in Villach.



---

# List of Figures

---

2.1	Conventional unit cell of silicon . . . . .	4
2.2	Point defects in silicon . . . . .	7
2.3	Recombination mechanisms in a semiconductor . . . . .	12
2.4	Ion implantation setup . . . . .	15
2.5	Concentration profiles of point defects due to proton implantation . . . . .	16
3.1	Zeeman splitting . . . . .	20
3.2	Hyperfine interaction . . . . .	22
3.3	Schematic diagram of an ESR setup . . . . .	23
3.4	Resonance condition for EDMR . . . . .	26
3.5	Schematic diagram of an EDMR setup . . . . .	27
3.6	Schematic diagram of a pn-junction in thermal equilibrium . . . . .	29
3.7	Schematic representation of a pn-junction without bias, under forward and under reverse bias . . . . .	30
3.8	Ideal current-voltage characteristic of a diode . . . . .	31
3.9	Scheme of a real current-voltage characteristic of a silicon diode in the forward bias . . . . .	32
4.1	EDMR setup based on a continuous wave EPR setup. . . . .	35
4.2	Analysis of the modulation amplitude dependence on modulation current. . . . .	37
4.3	DPPH Calibration . . . . .	38
4.4	Sample holder for EDMR . . . . .	39
4.5	SEM pictures of the conventional silver paste and of the silver paste with the adhesive property . . . . .	40
4.6	Schematic representation of the ideal doping concentrations for EDMR investigations. . . . .	42
4.7	Doping profiles of sample 1, sample 2 and the reference sample measured by spreading resistance profiling with a bevel angle of 0.847 degrees. . . . .	45

4.8	Logarithmic display of the IV-characteristics of the reference diodes outside the cavity and inside the cavity . . . . .	48
4.9	Dependence of EDMR signal height and signal-to-noise ratio on the bias conditions for the reference sample . . . . .	49
4.10	EDMR signal of the reference samples subjected to the basic annealings . .	50
4.11	EDMR signals of the reference sample for the investigation of the emergence of defect A . . . . .	52
4.12	Arrhenius plot of the recombination currents of the reference sample . . . .	53
4.13	Tilt series of the reference sample annealed at 350 °C for 60 min . . . . .	54
4.14	$g$ -value dependence of defect A in the reference sample. . . . .	54
4.15	Logarithmic display of the IV-characteristics of sample 1 outside the cavity and inside the cavity . . . . .	55
4.16	Dependence of EDMR signal height and signal-to-noise ratio on the bias conditions for sample 1 . . . . .	56
4.17	EDMR signals of sample 1 subjected to the basic annealings . . . . .	57
4.18	EDMR signals (1G, 3G) of sample 1 annealed at 350 °C for 15 min. . . . .	58
4.19	Recombination currents of sample 2 depending on the annealing parameters.	59
4.20	Tilt series of the sample 1 annealed at 350 °C for 60 min . . . . .	60
4.21	$g$ -value dependence of defect A in sample 1. . . . .	61
4.22	Logarithmic display of the IV-characteristics of sample 2 outside the cavity and inside the cavity . . . . .	61
4.23	Dependence of EDMR signal height and signal-to-noise ratio on the bias conditions for sample 2 . . . . .	62
4.24	EDMR signals of sample 2 subjected to the basic annealings . . . . .	63
4.25	EDMR results of the annealing sequence applied to sample 2 to determine the evolution of the doublet . . . . .	65
4.26	EDMR results of the annealing sequence to determine the evolution of the doublet in an enlarged representation . . . . .	65
4.27	Recombination current corresponding to the doublet in sample 2 depending on the annealing parameters. . . . .	66
4.28	Ratio of recombination currents of defect A and the doublet in terms of the annealing parameters . . . . .	67
4.29	Tilt series of sample 2 annealed at 350 °C for 60 min . . . . .	68
4.30	$g$ -value dependence of defect A in sample 2. . . . .	69
4.31	Tilt series of the sample 2 annealed at 450 °C for 15 min . . . . .	70
4.32	EDMR spectra of sample 2 for various annealing steps to determine the emergence of defect A . . . . .	71

---

4.33	Recombination currents corresponding to sample 2 annealed at various annealing steps. . . . .	72
4.34	IV characteristics of sample 1 annealed at 350 °C for 60 min . . . . .	73
4.35	Logarithmic display of the reverse bias current for different microwave power settings of sample 1 annealed at 350 °C for 60 min . . . . .	74
5.1	Comparison of the reference sample annealed at 350°C for 15 min with a newly cut and a HF etched analogous sample. . . . .	77
5.2	Fitting sequence to fit the double peak signal obtained in the reference sample annealed at 350 °C for 60 min with lorentzian derivatives . . . . .	79
5.3	Attempt to fit the recorded EDMR signals of the reference sample with 3 Lorentzian derivatives. . . . .	81
5.4	Attempt to fit the recorded EDMR signals of sample 1 where the double peak is visible with 3 Lorentzian derivatives. . . . .	82
5.5	Comparison of the tilt series obtained for sample 2 annealed at 350°C for 60 min with the comparable tilt series published in [1] . . . . .	84



---

# List of Tables

---

4.1	Main components of the EDMR setup . . . . .	34
4.2	Overview of the investigated samples . . . . .	42
4.3	Tabular display of the various annealing steps applied to the samples under investigation . . . . .	46
5.1	Zero crossings and corresponding $g$ -values of the three lorentzian fit curves to approximate the double peak EDMR signals of the reference samples . .	82
5.2	Zero crossings and corresponding $g$ -values of the three lorentzian fit curves to approximate the double peak EDMR signals of sample 1 . . . . .	83
7.1	Measuring parameters of sample 1. . . . .	89
7.2	Measuring parameters of the reference sample. . . . .	90
7.3	Measuring parameters of sample 2. . . . .	91



---

# Contents

---

<b>1</b>	<b>Introduction</b>	<b>1</b>
<b>2</b>	<b>Defects in Silicon</b>	<b>3</b>
2.1	Silicon . . . . .	3
2.1.1	Silicon crystal structure . . . . .	3
2.2	Basic defects . . . . .	4
2.2.1	Point defects . . . . .	5
2.3	How defects affect electrical and mechanical properties . . . . .	7
2.4	Defect complexes . . . . .	9
2.4.1	Thermal donors . . . . .	9
2.4.2	Hydrogen related thermal donors . . . . .	10
2.4.3	Recombination centres . . . . .	12
2.5	Defect generation and annihilation . . . . .	13
2.5.1	Ion Implantation . . . . .	13
2.5.2	Annealing . . . . .	16
<b>3</b>	<b>Electrically detected magnetic resonance</b>	<b>17</b>
3.1	ESR - Electron Spin Resonance . . . . .	17
3.1.1	Paramagnetism . . . . .	18
3.1.2	Zeeman Effect . . . . .	19
3.1.3	Hyperfine Interaction . . . . .	21
3.1.4	ESR Setup . . . . .	22
3.2	EDMR - Electrically detected magnetic resonance . . . . .	24
3.2.1	Spin Dependent Recombination . . . . .	24
3.2.2	EDMR Setup . . . . .	26

3.3 Diodes . . . . .	28
3.3.1 Basic operation . . . . .	28
3.3.2 Diode equation . . . . .	31
<b>4 Experimental results</b>	<b>33</b>
4.1 Experimental setup . . . . .	33
4.1.1 Modulation amplitude. . . . .	36
4.1.2 Calibration with DPPH . . . . .	37
4.1.3 Sample holder . . . . .	38
4.2 Sample description. . . . .	41
4.3 EDMR . . . . .	47
4.3.1 Reference sample. . . . .	47
4.3.2 Sample 1 . . . . .	55
4.3.3 Sample 2 . . . . .	61
4.4 Discussion of electrical characteristics. . . . .	73
<b>5 Discussion and Outlook</b>	<b>75</b>
5.1 Defect A . . . . .	75
5.2 Double Peak in the reference sample and sample 1 . . . . .	78
5.3 Doublet defect. . . . .	83
<b>6 Conclusion</b>	<b>87</b>
<b>7 Appendix</b>	<b>89</b>
7.1 Measuring parameters . . . . .	89
<b>Bibliography</b>	<b>93</b>

# CHAPTER 1

---

## Introduction

---

Proton implantation is a process used for various applications in silicon device manufacturing. Due to their small mass protons can travel deep into the material and locally create large concentrations of defects. During a subsequent anneal, these defects as well as the implanted hydrogen diffuse and can react to form a variety of defect complexes. Depending on the implantation dose, some of these defects can act as recombination centres used to locally adjust the carrier lifetime [2]. Another kind of defect complexes, the so-called hydrogen related thermal donor complexes, are electrically active generating  $n$ -type doping [3]. When high doses of protons are implanted, the formation of plate-like defects is initiated [4]. Annealing at elevated temperatures has been shown to have significant effects on the doping profiles introduced by proton implantation. Furthermore, transformations of the defects upon annealing have been observed. The structure of many hydrogen related defects and the processes causing their different behaviour are still somewhat unclear.

The aim of this work is to study proton implanted silicon pn-junctions by means of electrically detected magnetic resonance (EDMR), that has been proved to be a powerful technique to study point defects in fully processed devices. Hereby, the device is put in a magnetic field and electron spin resonance of the defects is induced by microwaves. Due to interactions of the spin-active defects with the conduction electrons, the ESR parameters of the defects can be measured in the device current. EDMR measurements can provide microscopic information about defect complexes with energy levels close to the mid band gap. However, only paramagnetic defects can be detected.

Preliminary studies have already shown the feasibility of EDMR measurements on proton implanted silicon pn-junctions. Changes in the EDMR patterns were observed for different proton implantation doses as well as after an annealing treatment [1]. The goal of this

thesis is to follow-up on these encouraging results and to continue the studies on proton implanted silicon pn-junctions. In the course of this study, different proton doses and annealing parameters were inspected in order to get a better understanding of the defects and the mechanisms involved. The study is performed at the Institute of Solid State Physics and the Institute of Experimental Physics at the Graz University of Technology in cooperation with Infineon Technologies Villach.

# CHAPTER 2

---

## Defects in Silicon

---

The aim of this chapter is to provide the necessary background for the understanding of this thesis. First, some basics of silicon are presented, in particular the microscopic structure and the electrical properties of this material which form the basis for the following section on defects. After presenting the basic defects to be found in crystalline materials, a special focus is set on defect complexes. In particular, hydrogen related thermal donor complexes are discussed. Subsequently, a further important issue is treated which exerts influence on the investigated diodes, namely defect generation and annihilation.

### 2.1 Silicon

Silicon is the second most common element in the earth's crust after oxygen. It constitutes an important semiconducting material that has been and still is dominating the semiconductor industry. Due to this fact silicon has already been investigated very well and in the following section some important properties of this material are presented.

#### 2.1.1 Silicon crystal structure

Silicon is a group IV element in the periodic table which implies that it has 4 electrons in the outermost shell. While the 1s, 2s, 2p and 3s shells are completely filled, there are 2 unpaired electrons in the 3p shell. Due to this arrangement, silicon tends to form 4 covalent bonds in a tetrahedral surrounding to its neighbours. This arrangement is known as the sp<sup>3</sup>-hybridisation. The 3s and 3p electrons participate in this bonding system.

Under standard conditions silicon crystallises in the diamond structure. In addition, there are some high pressure phases [5]. However, they are not relevant for this study as common

industrially produced devices are investigated which are made of the diamond structure silicon. The Bravais lattice of the diamond structure is face centred cubic (fcc) with two atoms in the basis, one at position  $(0,0,0)$  and the other one at  $(\frac{1}{4}, \frac{1}{4}, \frac{1}{4})$ . The diamond structure can also be thought of as two fcc lattices where one is displaced by a quarter of the length of the unit cell in the 3 main directions x, y and z. The lattice constant of silicon is 0.357 nm. In 2.1 the conventional unit cell of silicon can be seen.

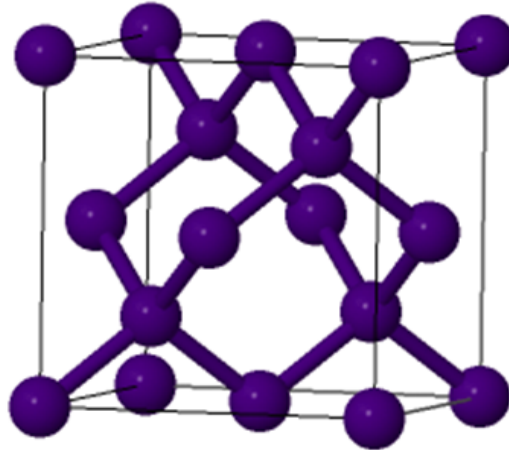


**Figure 2.1:** Conventional unit cell of silicon

## 2.2 Basic defects

Some of the basic concepts regarding defects are introduced in this section. Good references to this subject are the books of Peter Pichler on "Intrinsic Point Defects, Impurities and Their Diffusion in Silicon" [6] and "Physikalische Grundlagen der Materialkunde" by Günter Gottstein [7].

In the previous section 2.1.1 the ideal crystal structure of silicon was introduced. However, defects are always present and the concentration of these defects is rarely in thermodynamic equilibrium. This means that the defect concentrations evolve in time. Not only do the defects give silicon crystals new properties, but they also play a major role for the processing as well as in the functioning of semiconductor devices. Defects are often intentionally introduced to add dopants, to reduce the minority carrier lifetime, or to modify the mechanical properties. However, defects can also exert negative influence on the device performance and are therefore unfavourable.

There are different ways to categorise the various defects appearing in the silicon crystal. As a first approximation, defects can be distinguished by their dimensionality. The defects with the lowest dimensionality are called "point defects" and in their simplest

form they only influence their nearest neighbour atoms and are not extended in space (zero-dimensional). However, point defects can agglomerate in the crystal and thereby expand, but there is no accurate limit for the extent of point defects in the crystal lattice. Point defects are particularly important with regard to diffusion processes in crystals as the diffusion constant of impurity atoms depends highly on the concentration of vacancies present. One-dimensional defects are termed "line defects" and there are two basic types, namely edge dislocations and screw dislocations. An edge dislocation is basically an extra half-plane in the regular crystal structure. The screw dislocation can be thought of as the result of cutting the crystal along a plane and then shifting the atoms along the cut line by a lattice vector. In both cases the crystal structure is interrupted along a line. Dislocations have an impact on the fracture behaviour of silicon under strain. Two-dimensional defects like stacking faults, grain and phase boundaries usually do not appear in silicon. Finally, there are volume defects also called three-dimensional defects like precipitations or voids that can form by the agglomeration of point defects.

### 2.2.1 Point defects

Point defects can basically be distinguished between intrinsic and extrinsic. An intrinsic point defect means that there are no impurity atoms involved. In the silicon crystal there are two basic types of intrinsic defects: vacancies and self-interstitials.

A vacancy is an unoccupied lattice site and since silicon is a monoatomic crystal, this means that a silicon atom is missing. Vacancies are denoted with the abbreviation "V" and they can arise due to several reasons. One cause relies on the fact that a near-surface atom jumps to the surface and thereby leaves a vacancy behind. This vacancy subsequently moves to the bulk of the crystal by swapping places with silicon atoms in the bonding network. Another possibility is the shift of a silicon atom from its lattice site into an interstitial site whereby not only a vacancy but also a self-interstitial defect is created. This point defect pair is referred to as a Frenkel-defect. Both processes discussed rely on thermal activation at which the activation energy for the creation of a vacancy in silicon lies at about 2.6 eV [8]. To push a silicon atom to an interstitial site needs an activation energy of about 4.5 eV [8]. However, the most important source of vacancies in the investigated samples is implantation. This process is also the major source for interstitials and extrinsic defects which are explained below. Apart from the mono-vacancy, more complicated arrangements like a two-vacancy complex called "di-vacancy" or even vacancy clusters can appear.

A self-interstitial defect describes the situation where the host atom silicon sits at a normally unoccupied interstitial site and it is denoted with the abbreviation "I". In every crystal structure there exist small voids that can serve as possible sites for atoms, whereby

those interstitial sites are well-defined locations. Silicon with its relatively open crystal structure offers five interstitial sites per unit cell [9]. As it is the case for vacancies there are more complex arrangements also for interstitials, like di-interstitials or larger self-interstitial agglomerates. In the local surrounding of both defects, vacancies and self-interstitials, the regular crystal arrangement is slightly distorted because of the missing or additional atoms which is indicated in 2.2.

Extrinsic point defects are defined by the participation of impurity atoms. Among these defects it can be further distinguished between substitutional impurities and interstitial impurities. A substitutional impurity is represented by an impurity atom that replaces a silicon atom by residing on a regular lattice site. The possibility of introducing foreign atoms into the silicon lattice is particularly important for the essential doping process during device manufacturing, as the electrical properties of silicon can be altered in this way. Atoms from group III and V are primarily incorporated, because due to their atomic structures they can either act as donors or acceptors of electrons. Effects of these defects on the electrical properties of silicon are discussed in the following section (2.3). The designation of the substitutional impurity defect is most easily explained with an example: a carbon atom substituting a silicon atom is denoted with " $C_S$ " where the first character is related to the type of impurity atom and the second character specifies the position within the crystal arrangement. Possible defect complexes containing substitutional impurities could be an impurity-vacancy pair or an impurity-self interstitial pair. Interstitial impurity atoms behave in analogy to their intrinsic counterpart and occupy a normally vacant interstitial site. The designation of this defect is again clarified with an example: a carbon atom occupying an interstitial site in the silicon lattice is denoted with " $C_i$ ". Extrinsic point defects also cause a local distortion of the regular crystal arrangement. The impact of this distortion is highly dependent on the size of the impurity atoms. The basic defects described above cannot be considered to be independent of each other, because they can all interact and thereby form new defect species. A schematic representation of the main point defects in silicon is given in the figure 2.2.

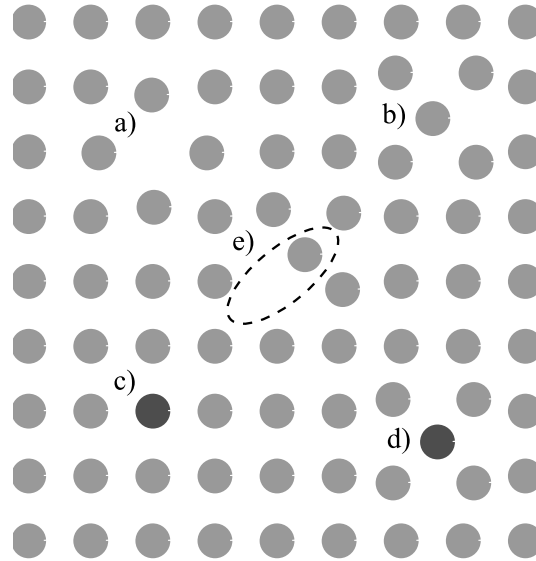


**Figure 2.2:** Point defects in silicon: a) Vacancy "V" b) Self-interstitial "I" c) Substitutional Impurity d) Interstitial impurity e) Frenkel-pair

### 2.3 How defects affect electrical and mechanical properties

Small concentrations of defects can already have a significant impact on electrical and mechanical properties. Among the present defects, especially the electrically active ones with energy states within the band gap have the ability to affect electrical properties dramatically. Energy states close to the conduction and valence band act as electron or hole donors, respectively. In contrast, the energy states in the middle of the band gap rather act as recombination or generation centres.

Already the growth of the single crystal material out of which electronic devices are produced is a crucial step regarding the introduction of point defects that can influence electrical and mechanical properties. The influence of the manufacturing process on defect concentrations is discussed below.

There are two common processes which are used to fabricate single crystal silicon: the Czochralsky process (Cz) [10] and the Floating zone process (Fz) [11]. In the Czochralsky process, silicon single crystals are produced by dipping a seed crystal into liquid silicon and then pulling this seed crystal slowly out of the melt while rotating it. Dopant atoms can be incorporated into the melt in order to adjust the doping type and concentration. Impurities that are incorporated into the silicon wafers resulting from this process are mainly oxygen originating from the crucible ( $\text{SiO}_2$ ) and carbon. Typical concentrations are:  $[\text{O}] = 5 - 10 \times 10^{17} \text{ 1/cm}^3$  and  $[\text{C}] = 5 - 50 \times 10^{15} \text{ 1/cm}^3$  [12]. Most of the oxygen atoms occupy interstitial sites in silicon and the relatively high concentration can have various effects on the device properties. Heat treatments around  $450 \text{ }^\circ\text{C}$  can lead to the formation of electrically active defect complexes due to oxygen. These so called

oxygen related thermal donors (2.4.1) can change the resistivity of the material just like substitutional dopants. There is a difference in the mechanical strengths of Cz-grown silicon and Fz-grown silicon. The higher concentration of oxygen atoms seems to cause a higher yield strength in Cz silicon, since oxygen atoms have the ability to pin unintentionally introduced dislocations during wafer processing, whose migration is responsible for deformation and fracture [13]. In addition, oxygen has the ability to make the silicon more resistant to thermal stress and oxygen precipitates can suppress stacking faults. Furthermore, a high oxygen concentration contributes to an increased radiation stability [12]. Unfavourable effects of oxygen are the defect generation if precipitates are formed and further on the lattice mismatch that arises when the precipitates grow in size. Impurity carbon favours the occupation of substitutional lattice sites and has the negative property of aiding the formation of defects.

Silicon wafers produced with the crucible-free float zone method provide a lower defect concentration compared to Cz silicon. In this process, a poly-crystalline silicon rod is locally heated with a heater ring moving slowly from one end of the rod to the other. A seed crystal is in contact with the rod determining the crystalline orientation of the resulting single crystal. The fact that the concentration of impurities is higher in the liquid than in the solid phase leads to an accumulation of impurities at one end of the rod which can be cut off at the end. By repeating this process several times, the silicon can be further rendered. In contrast to the Czochralsky process doping cannot be executed simultaneously with crystal growth, since the desired dopant atoms are also eliminated. This is a major drawback of the float zone method because additional processes need to be performed to dope the silicon. The value of the impurity concentrations for oxygen and carbon in this process is below  $5 \times 10^{15} \text{ 1/cm}^3$  [12].

The fact that already small concentrations of impurity atoms can change electrical properties is used in the fundamental doping process. Doping means that impurity atoms are intentionally introduced by either adding the dopants directly into the melt (Cz silicon) or by performing additional processes like ion implantation, neutron transmutation doping or gas phase diffusion. The impurity atoms that occupy substitutional lattice sites, can subsequently add electrons or holes to the conduction and valence band, respectively. Thereby the respective conductivities are enhanced. Donor atoms mainly originate from group V, where phosphorus is a prominent donor in silicon technology (*n*-type doping). Atoms from group V have five valence electrons, but only four of them are needed for the binding with silicon. Therefore, one extra electron is present which is in fact weakly localised due to Coulomb interaction with the nucleus. However, it can be easily ionised and thereby contribute to the conductivity. Considering the band structure of silicon, the donor atoms generate energy states located close to the conduction band. While donor atoms contribute electrons to the conduction band, acceptor atoms contribute holes to

the valence band (*p*-type doping). Acceptor atoms are mostly group III elements, where boron is an important representative. These elements have three valence electrons meaning that one electron is missing for the binding with the silicon atoms in the fourfold binding system. The missing electron is per definition considered as a hole. The energy states generated by acceptor atoms are located just above the valence band. Therefore, an electron from the valence band can easily get trapped in the acceptor state. As a consequence, a hole is created in the valence band where it contributes to the transport analogous to an electron in the conduction band. Besides this common method of introducing impurity atoms, defect complexes can also act as donors or acceptors in silicon which is discussed later on. The change of resistivity due to the incorporation of donor and acceptor atoms is utilised in the so-called spreading resistance profiling (SRP). This method enables the determination of charge carrier concentration profiles by measuring the resistivity of semiconducting samples as a function of position. [14] [15]

## 2.4 Defect complexes

The term "defect complex" refers to the association of basic defects, whereby new defect species are created. In principle, all defects present in silicon can interact with each other and thereby form a range of defect complexes, which can exhibit different properties compared to their constituent parts. Depending on the position of their energy states in the band gap, the defect complexes can act as donors, acceptors or recombination centres and have the ability to change material properties. They can exist in various charge states (neutral, negative, positive or even doubly ionised) and their formation is mainly initiated by diffusion due to heat treatments. Some defect complexes can also have several charge states in the band gap. In many cases, the presence of defect complexes in semiconducting devices is undesirable because the formation processes and structures are not sufficiently understood and therefore not controllable. Important examples in silicon are the thermal donors, at which one species has been related to the presence of oxygen and another group is related to the participation of hydrogen. These two important defect complexes are discussed in the following subsections.

### 2.4.1 Thermal donors

Thermal donors (TD) are a group of electrically active donor complexes containing oxygen atoms. The term "thermal donor" refers to the fact that this defect species is formed due to heat treatments in the range of 350 - 550 °C. Especially in lightly doped silicon, the impact of thermal donors can be serious, since changes of the effective doping concentrations or a majority carrier type conversion from *p* to *n* can appear. In device manufacturing

annealing steps are inevitable and during these heat treatments donor formation can be initiated. It is important to avoid or at least control this process. In 1955, Fuller first discovered the formation of electrically active centres upon annealing [16], which later turned out to be donors. Since then, a lot of research has been performed to investigate this group of defects and a series of different models was proposed, but until now the electrical and structural properties of oxygen related thermal donors are not fully understood. Oxygen usually occupies interstitial sites in silicon and in this configuration it is electrically inactive. Otherwise it would not be possible to fabricate electronic devices based on Cz silicon with its high oxygen concentration. At elevated temperatures the oxygen atoms become mobile, start to diffuse and can react to defect complexes. The diffusivity of oxygen in silicon, however, does not suffice to explain the formation of donor complexes. Therefore, diffusion of molecular oxygen  $O_2$  or even longer oxygen chains is proposed. It was found that the presence of hydrogen can accelerate the oxygen diffusion due to a pair diffusion mechanism and promote the diffusion limited formation of thermal donors in this way [17]. The most important parameters controlling the formation of thermal donors are the annealing temperature, the annealing time and the initial oxygen concentration present in silicon. The overall rate of formation at 450 °C was found to depend on the fourth power and the maximum concentration of TD on the third power of the oxygen concentration [18]. By now it has become clear that the species of oxygen related thermal donors can be subdivided into three families: the shallow thermal donors (STD's) or single donors, thermal double donors (TDD's) and the high temperature thermal donors or new thermal donors (ND's). There are at least 16 TDD's reported which are proposed to have the same core but differ in the number of participating oxygen atoms [12]. However, the exact structure is still unknown. While the existence of TDD's and STD's can be reversed at heat treatments higher than 500 °C, the so-called new donors are generated in this temperature range, but also little is known about this species. Further details regarding thermal donors can be found in references [12] and [18] where most of the information above is taken from.

#### **2.4.2 Hydrogen related thermal donors**

From a technological perspective hydrogen is a very important impurity in silicon. Intentionally or unintentionally introduced into silicon, the very reactive hydrogen can affect the electrical properties in various ways. The implantation of hydrogen generates a high number of defects in the material. If a subsequent annealing is applied, the defects can diffuse and react to form a variety of defects complexes. Some electrically active complexes have the ability to influence the concentration of charge carriers and others can affect the charge carrier lifetime by acting as recombination centres. Hydrogen interacts

with intrinsic as well as extrinsic defects. It readily saturates and thereby deactivates electrically active deep level states that could serve as potential recombination centres. It can occur in different charge states (neutral,  $H^+$ ,  $H^-$ ) which enables the formation of ionic bonds with ionised dopants. In this way the respective donor or acceptor atoms can be passivated. The outcome is a decrease of charge carriers. However, this effect is only relevant at low temperatures since the complexes formed become instable at temperatures above 150 °C. In the following section, a focus is set on the explanation of the so-called hydrogen related thermal donors (HTD), a group of defect complexes linked with hydrogen and the property of contributing to the electron conductivity. Hydrogen related thermal donors are of special interest for this thesis, since the investigated samples have been doped with hydrogen using parameters that should allow for the formation of these donor complexes. An increase of electron conductivity in proton irradiated silicon was the first time reported in 1970 by Schwuttke *et al.* who attributed the increase of conductivity to the formation of a donor associated with hydrogen [19]. A lot of research has been performed since then whereof a very good and detailed overview can be found in the dissertation of J. Laven [15], where most of the information for this section is taken from. The creation of HTD's is based on the decoration of radiation induced defect complexes with hydrogen. The existence of crystal damage produced by irradiation and the presence of hydrogen are necessary preconditions for the formation of HTD's. The name "thermal donor" already indicates the fact that an annealing step is required to form the desired shallow donor level. During this annealing step, the hydrogen is mobilised and can interact with the available defect complexes. The fact that both, defect complexes as well as hydrogen need to be present in order to allow for the donor formation, has been shown in several exclusion experiments. Proton implantation has the advantage that the necessary crystal damage as well as hydrogen are simultaneously introduced. The maximum of the formed donor distribution coincides with the maximum of the damage profile after the implantation. Donor formation was also observed after the implantation of deuterium and tritium. However, the maximum of the donor distribution was shifted towards the surface according to the higher masses of the implanted ions compared to protons. Besides proton implantation, it is also possible to create the crystal damage with other particles like neutrons, electrons or with helium irradiation. In these cases, a subsequent hydrogen supply is essential which can be provided for example by a hydrogen plasma. There is not one specific hydrogen related thermal donor defect, but rather a group of defects with similar structures all with relatively low ionisation energies but each with an individual healing behaviour. The formation of HTD's starts at temperatures of about 300 °C. When exceeding temperatures higher than 500 - 600 °C the thermal donors decompose irreversibly. In between this temperature range the respective contribution of the HTD's to the electron conductivity reaches a maximum at different temperatures. In addition, it

has been shown that also without an annealing step there are donors present in implanted samples, but they do not exhibit a high thermal stability and vanish at 200 °C. In the reference [15] on page 24, a table of already known HTD's can be found together with the temperature ranges where they exist, the ionisation energies, the production process and the corresponding references.

### 2.4.3 Recombination centres

Recombination is a process where charge carriers of both types, electrons and holes, are lost leading to a decrease in the conductivity. The dominant recombination mechanisms in semiconductors are the band-to-band recombination and trap assisted recombination where the latter is associated with a recombination centre being a deep level state located in the middle of the band gap. Recombination centres have their origin in structural defects as well as impurity atoms. To complete the possibilities of recombination mechanisms, the Auger recombination has to be mentioned. In figure 2.3 a schematic illustration of the relevant recombination processes is provided.

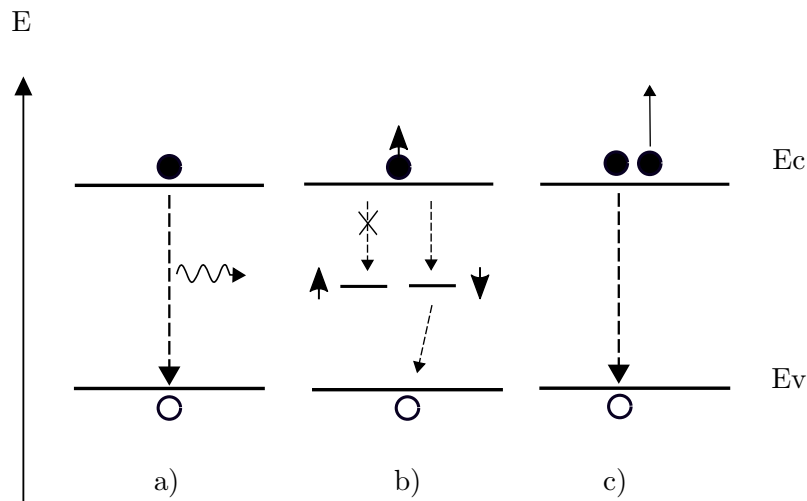


**Figure 2.3:** Recombination mechanisms: **a)**Band-to-band recombination **b)**Trap assisted recombination and **c)**Auger recombination

The band-to-band recombination (a) signifies the radiative recombination of an electron from the conduction band with a hole in the valence band emitting the energy difference in form of a photon. This process is favourable in direct semiconductors where the momentum is conserved due to the transition of the electron. If the energy available from the recombination is subsequently given off to another charge carrier in the form of kinetic energy one refers to Auger recombination (c). In indirect semiconductors like silicon, the trap assisted recombination (b) is more probable where electrons and holes are successively trapped and annihilated in a state located around the middle of the band

gap acting as a recombination centre. This process is accompanied by the emission of a phonon to dissipate the excess energy leading to heat generation in the lattice [20]. Since electrons have a spin the relative orientation of the recombination centre spin if existing, for example in the case of a dangling bond, relative to the conduction band electron spin is of relevance when it comes to the recombination process. If the spins are aligned parallel the recombination is not allowed, if the spins are aligned anti-parallel the electron can recombine over the recombination centre. Trap assisted recombination is a non-radiative two step process and the transition rate is described by the Shockley-Read-Hall equation.

$$R^{\text{SRH}} = \frac{n \cdot p - n_i^2}{\tau_p \cdot (n + n_1) + \tau_n \cdot (p + p_1)}, \quad n_i^2 = n_1 \cdot p_1 \quad (2.1)$$

$$n_1 = N_c \cdot \exp\left(\frac{-E_C + E_T}{k_B \cdot T_L}\right), \quad (2.2)$$

$$p_1 = N_v \cdot \exp\left(\frac{-E_T + E_V}{k_B \cdot T_L}\right). \quad (2.3)$$

The variables  $\tau_p$  and  $\tau_n$  describe the recombination lifetimes of electrons and holes, respectively.  $E_T$  represents the trap energy level whereby the recombination rate reaches its maximum if this level is located in the middle of the band gap.  $N_c$  and  $N_v$  are the effective densities of states in the conduction and valence band, respectively. The variable  $T_L$  describes the lattice temperature. [21]

## 2.5 Defect generation and annihilation

In a solid defects can develop in many ways. Processes like doping, particle irradiation as well as annealing play a role in defect generation. However, one major source of defects is the implantation process. In this context, defect generation is the consequence of energy transfer from the particles irradiating the material towards the irradiated solid whereby permanent damages can occur. In order to reduce the crystal damage which can cause serious degradation of device performance, the implantation process is commonly followed by heat treatments where an annealing of the crystal structure is initiated. In this way, the number of crystal defects is reduced and the electrical properties can be restored.

### 2.5.1 Ion Implantation

Ion implantation is a method frequently used in semiconductor industry to intentionally introduce dopant impurity atoms into a semiconducting material. The desired ions are

extracted from an ion source and accelerated in an electric field after which the ion beam is deflected by a magnetic system. Subsequently, the ions are implanted into the target material. A very basic representation of how an ion implanter is arranged can be found in figure 2.4. The high energy process of ion implantation is accompanied by plenty of crystal damage and structural changes in the target crystal lattice due to the penetrating ions. The ions are decelerated and finally stopped in the target medium due to various interactions. On the one hand, the ions interact with the electrons in the material referred to as electronic deceleration. On the other hand, there is an interaction with the atomic cores that can be elastic or inelastic called nuclear deceleration. The latter interaction is mainly responsible for the emergence of the damage profile induced by the energy transport of the ions to the lattice atoms. The electronic deceleration is based on Coulomb interactions and can be considered continuously as any time a huge number of electrons participates in this process. Besides electronic excitations, ionisations or the creation of electron-hole-pairs can occur. Especially for ions with a low atomic number or high energies, the electronic deceleration is the dominant mechanism. Like for the electronic part the nuclear deceleration is also based on Coulomb forces. The ions are decelerated by transferring parts of their kinetic energy to the interaction partners. The amount of transferred energy is crucial concerning the emergence of crystal damage. The threshold energy that is needed to move an atom from a regular lattice site to an interstitial site is called  $E_{Frenkel}$ . It is composed of the energy needed in order to separate chemical bonds and of the displacement energy to overcome the energy barrier to the interstitial site. The result is a Frenkel-pair that is only stable if the spacing between the vacancy and the interstitial atom is large enough to prevent recombination. In order to ensure this condition the shifted atom requires some additional kinetic energy. The energy of formation of a stable Frenkel-pair in silicon is about  $E_d = 14$  meV [22] and shows a dependence on temperature. A detailed description on implantation physics is offered by J. Laven's dissertation [15], which serves as a reference for this section.

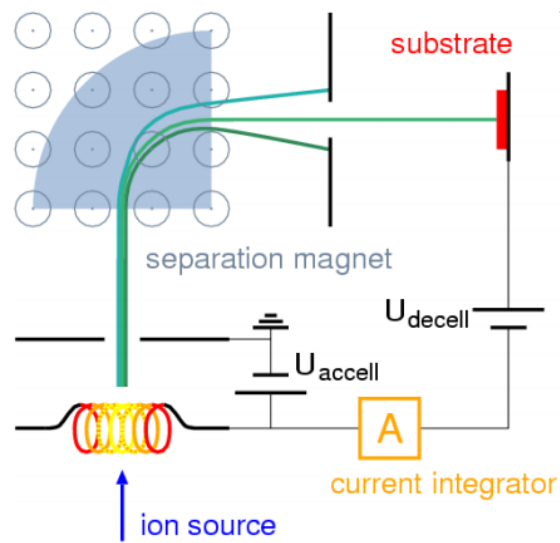


**Figure 2.4:** Ion implantation setup. Taken from reference [23]

### 2.5.1.1 Hydrogen implantation

During the hydrogen implantation process ionised hydrogen atoms (protons)  $\text{H}^+$  are implanted into silicon. Due to their light weight protons can penetrate deeper into materials compared to other commonly used ions and locally create large concentrations of defects. Important parameters in the hydrogen implantation process are on the one hand, the implantation energy determining the depth of the implanted ions and on the other hand, the implantation dose that corresponds to the amount of protons implanted. In figure 2.5 a Monte-Carlo-Simulation of a concentration profile of point defects originating from proton implantation can be seen. As shown in this figure, there is a peak in the concentration of hydrogen, vacancies and interstitials at the projected implantation depth of the protons. This projected range depends on the energy of the implanted protons. Mainly vacancies and interstitials are generated during the implantation process. The higher the implantation energy, the deeper the protons penetrate into the material. The concentration of the damage is rather localised and distinct in the region where the protons are finally stopped.

Depending on the implantation dose there are several applications for the incorporation of hydrogen into silicon. Low implantation doses are used to locally introduce recombination centres, used to adjust the carrier lifetime [2]. Low implantation doses correspond to the range up to about  $10^{13} \text{ H}^+ \text{ cm}^{-2}$ . In the range of middle implantation doses, from  $10^{13} \text{ H}^+ \text{ cm}^{-2}$  to  $10^{15} \text{ H}^+ \text{ cm}^{-2}$ , the electrically active hydrogen related thermal donor defects are created if a subsequent heat treatment between  $300 \text{ }^\circ\text{C}$  and  $500 \text{ }^\circ\text{C}$  is applied [3]. In the present work the investigated samples have been implanted with doses that al-

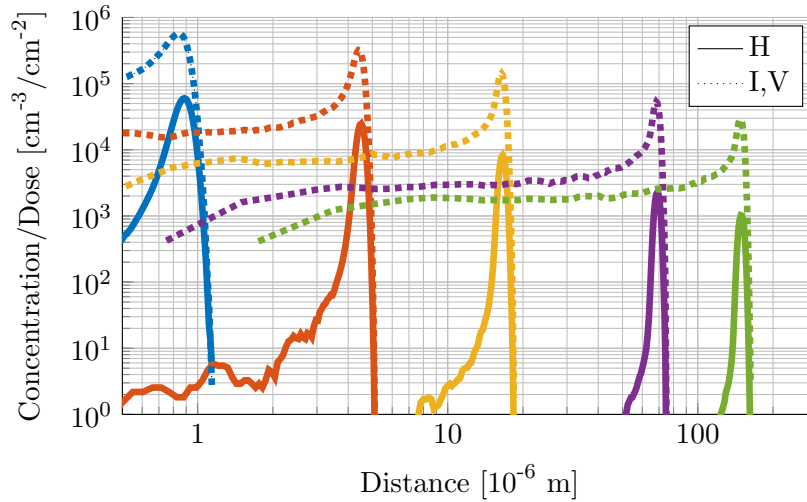


**Figure 2.5:** Log-log plot of point defect concentration profiles normalised to the proton dose for different implantation energies. Simulated implantation energies (from left to right): 100 keV, 400 keV, 1 MeV, 2.5 MeV, 4 MeV. In the simulation an incidence angle of  $7^\circ$  was used. The concentration profiles were calculated by Martin Faccinelli.

low for the formation of this HTD's. Implantation doses above  $10^{16} \text{ H}^+ \text{ cm}^{-2}$  can be used to cleave the substrate due to the formation of platelet-like defects resulting from high damage concentrations induced by the protons [4].

### 2.5.2 Annealing

Annealing is an important thermal process in semiconductor manufacturing that has several important functions. Besides the effect of curing radiation damages generated by implantation, the annealing can also initiate the electrical activation of dopant atoms and the formation of defect complexes that act as dopants like HTD's. The mechanism of annealing is basically composed of the three processes migration, defect formation and dissociation. Each of these processes is characterised by an activation energy. At room temperature defects are rather immobile and only diffuse very slowly. Due to the supply of energy by the annealing process, migration is accelerated as the energy barrier of diffusion can be overcome. On the one hand, this allows for the formation of defect complexes with other atoms or defects in the material. On the other hand, annihilation of interstitials and vacancies can be initiated. Defect complexes are formed if an energetically more favourable energy state can be achieved and the energy suffices to reach this state. At high temperatures dissociation of defect complexes occurs after which the constituents themselves can further migrate and react or get trapped. Energetically this means that the amount of energy supplied, in fact the lattice vibrational energy, suffices to overcome the dissociation energy of the respective defect complex [12].

## CHAPTER 3

---

### Electrically detected magnetic resonance

---

This chapter provides the principles of Electron Paramagnetic Resonance (EPR) which form the basis of electrically detected magnetic resonance (EDMR), the main method applied in this thesis. First, paramagnetism and the fundamental Zeeman effect are described. This effect serves as the basis for the concept of spin resonance in an applied magnetic field under microwave irradiation. Thereafter, the EDMR method is defined with the main theories describing it, the detection principle used and the experimental setup. The final section is dedicated to the application of EDMR to silicon diodes.

#### 3.1 ESR - Electron Spin Resonance

Electron spin resonance (ESR) also known as electron paramagnetic resonance (EPR) is a spectroscopic method used to study paramagnetic substances. As described in the previous chapter, point defects can have several charge states in the band gap out of which some are paramagnetic. That is why ESR is a powerful method applicable to investigate defects in semiconductors. The characterisation of defects is conducted by analysing the  $g$ -values as well as the hyperfine interactions arising due to nearby nuclei with a nuclear spin  $I \neq 0$ . Since the first ESR measurements in 1945 by Zavoisky [24], this method has been used frequently to identify paramagnetic defects in solids. However, the detection limit of  $\approx 10^{10}$  defects is the technique's major problem. The limiting factor of sensitivity in ESR is the rather small Zeeman splitting together with the limited sensitivity of the detector diode [25]. Therefore, methods with higher sensitivities such as EDMR or optically detected magnetic resonance (ODMR) have been developed over time. It is the former method that is in the focus of this thesis. In order to understand the principles

of EDMR it is necessary to provide an introduction to the fundamentals of ESR with the underlying physical principles first. As a detailed description of ESR would exceed the scope of the thesis, further information can be found in the textbooks [26] and [27]. These sources cover most of the information given below.

### 3.1.1 Paramagnetism

Substances are referred to as paramagnetic when they contain atoms, molecules or ions with permanent magnetic dipoles. When exposed to an externally applied magnetic field, the magnetic moments in paramagnetic materials align in the direction of the field inducing an additive field in the direction of the external one. This behaviour is in contrast to diamagnetic materials where the induced field is aligned in the opposite direction of the external field, thus lowering the total field. In the absence of a magnetic field both paramagnetic and diamagnetic materials do not exhibit any net magnetisation.

Generally, the magnetic moment of a system can be composed of two contributions: one resulting from the motion of charges and the other one from the intrinsic magnetic moment of elementary particles. Consider a single electron. According to classical electrodynamics, a magnetic dipole arises if an electron located in an orbital is moving around a nucleus, which can easily be imagined in the case of a hydrogen atom. The orbital angular momentum  $\mathbf{L}$  then results in an orbital magnetic moment

$$\boldsymbol{\mu}_L = -\mu_B \mathbf{L} \quad (3.1)$$

with  $\mu_B$  being the Bohr magneton.

By considering the fact that electrons possess the quantum mechanical property of spin ( $S = \frac{1}{2}$ ), the spin angular momentum  $\mathbf{S}$  also gives rise to a magnetic moment. This spin magnetic dipole moment is defined by

$$\boldsymbol{\mu}_S = -g_e \mu_B \mathbf{S} \quad (3.2)$$

where  $g_e$  is the  $g$ -factor of the free electron ( $g_e \approx 2$ ). Consequently, the total magnetic dipole moment  $\boldsymbol{\mu}_J$  is the sum of both, orbital and spin angular momentum:

$$\boldsymbol{\mu}_J = \boldsymbol{\mu}_L + \boldsymbol{\mu}_S \quad (3.3)$$

If two electrons are paired in the same orbital, they need to differ in their spin quantum number. As a result, their magnetic moments balance each other out resulting in a net moment of zero, thus diamagnetic behaviour. Everything has a diamagnetic response regardless of the type of material or number of electrons. Paramagnetic behaviour is observed in systems that contain unpaired electrons. These materials contain permanent

dipole moments that can be aligned. If the paramagnetic response is larger than the diamagnetic response the total response is paramagnetic. This applies for paramagnetic point defects and enables their investigation by the application of ESR. The method is limited to the investigation of paramagnetic defects, since a net magnetic moment is necessary for interactions with a magnetic field.

For a detailed description of ESR it is important to understand the behaviour of magnetic moments in a magnetic field. Besides electrons also atomic nuclei can be associated with a spin  $I$  depending on the number of protons and neutrons in the corresponding nucleus. The resulting magnetic moment is defined by

$$\boldsymbol{\mu}_N = g_N \mu_N \mathbf{I} \quad (3.4)$$

where  $g_N$  is the nuclear  $g$ -factor and  $\mu_N$  the nuclear magneton. The interactions of the magnetic moments defined in equations (3.1) - (3.4) with an externally applied magnetic field are described by the following Hamiltonian

$$\mathcal{H} = \mathcal{H}_{Z,e} + \mathcal{H}_{Z,N} + \mathcal{H}_{HF} + \mathcal{H}_{e,e} \quad (3.5)$$

where the first term describes the electron Zeeman interaction, the second term the nuclear Zeeman interaction, the third term the hyperfine interaction and the last term the electron-electron interaction. Equation (3.5) is mentioned for the sake of completeness but in the following only the electron Zeeman interaction and the hyperfine term are discussed in more detail. The remaining terms do not have specific relevance with respect to the experiments conducted.

### 3.1.2 Zeeman Effect

The electron Zeeman interaction concerns the interaction of the electron magnetic moment with an externally applied static magnetic field  $B_0$ . Electrons are particles with a spin of  $S = \frac{1}{2}$  and if no magnetic field is applied the energies corresponding to the respective spin states are degenerate. By applying a magnetic field  $B_0$  the energy states split into two different Zeeman levels due to the two possible alignments for the spins in the external magnetic field (parallel or anti-parallel). The resulting difference in energy is referred to as the Zeeman splitting  $\Delta E$ . The two possible states correspond to the magnetic quantum numbers  $m_s = +\frac{1}{2}$  or  $m_s = -\frac{1}{2}$  and the energies for an electron in the magnetic field become

$$E_m = g\mu_B B m_s \quad (3.6)$$

The energy level separation  $\Delta E = E(m_s = 1/2) - E(m_s = -1/2)$  between these two levels can be changed by varying the strength of the applied magnetic field. Under conditions of thermal equilibrium the number of spins in the lower Zeeman level exceeds the number of

spins in the higher one [28]. In figure 3.1 the energy level diagram for a spin 1/2 particle exposed to a magnetic field can be seen together with the ESR signal that would result from this system.

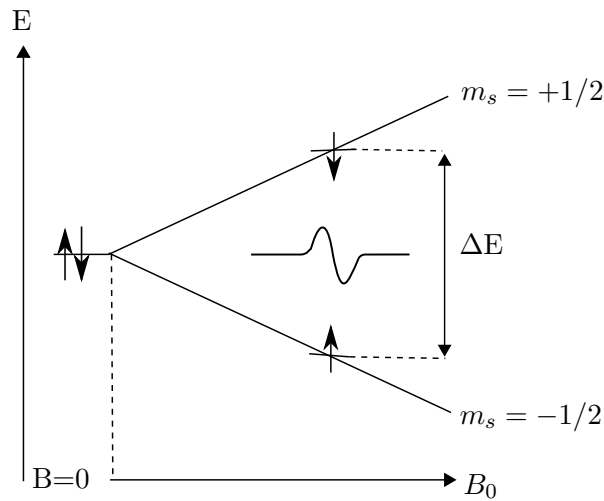


**Figure 3.1:** Energy level diagram for a spin 1/2 particle exposed to a magnetic field together with the ESR signal.

Transitions between the two Zeeman levels can be induced by applying a second alternating magnetic field  $B_1$  in addition to the field  $B_0$ . Two conditions must be met in order to induce transitions from the lower energy state into the upper energy state and thereby let resonant absorption occur. On the one hand, the additional magnetic field  $B_1$  has to have a suitable frequency  $\nu$  to match the energy difference between the Zeeman levels so that  $\Delta E = h\nu$ . On the other hand, the magnetic component of field  $B_1$  must be able to interact with the magnetic dipole moment to allow for magnetic dipole transitions. Therefore, the field  $B_1$  has to be oriented perpendicular to field  $B_0$ . The essential condition for resonance is given by

$$h\nu = g\mu_B B_0 \quad (3.7)$$

with  $h$  being Planck's constant,  $\nu$  the frequency of the alternating field  $B_1$ , the  $g$ -factor  $g$  used to identify defects, the Bohr magneton  $\mu_B$  and the field  $B_0$  that causes the splitting in energy. If this resonance condition is fulfilled, the system absorbs the energy from the incoming radiation in order to flip the electron spin, i.e., a photon is absorbed. In a standard ESR setup the resonant field  $B_1$  is applied in the form of microwave radiation because the energies needed to induce transitions require frequencies in the microwave range. As can be calculated from equation (3.7) transitions appear at a frequency of around 9 GHz if a magnetic field of 3000 G is applied assuming a  $g$ -value of 2. This frequency belongs to the X-Band range of the microwave radiation (8 - 12 GHz) that is

commonly used in ESR measurements. Usually, the frequency of the microwave source is kept constant while the magnetic field is slowly swept over a certain range. This method is called continuous-wave (cw) ESR. The detection principle of ESR is based on the fact that under resonance an increased absorption of microwaves occurs, which is indicated by a change in the detector current. Out of the resulting absorption spectrum the  $g$ -value can be determined by using (3.7). The  $g$ -value constitutes an important parameter to characterise and identify the defects observed. The  $g$ -values determined by ESR measurements are all found to be close to the  $g$ -value of the free electron  $g_e$ . Nevertheless, all of them differ slightly for different materials. It is the orientation of the defect under observation towards the magnetic field and the local magnetic surrounding in individual materials that offer the explanation of these differences. Apart from the externally applied magnetic field  $B_0$  additional local magnetic fields can arise in a material. These two magnetic fields add up to form an effective magnetic field that is influencing the  $g$ -values. In fact, the  $g$ -value is not a single value but a  $3 \times 3$  matrix describing the angular dependence of the Zeeman splitting with regard to the static magnetic field applied. By performing measurements with different orientations between the static magnetic field and the crystal, the symmetry of defects can be revealed. In order to identify defects, the  $g$ -matrix is usually diagonalised to obtain the three characteristic  $g$ -values  $g_{xx}, g_{yy}, g_{zz}$  that can be compared with literature. Generally, these three values differ from each other describing anisotropic symmetry conditions. However, in the isotropic case the  $g$ -values are independent from the crystal orientation, thus  $g_{xx} = g_{yy} = g_{zz}$ .

### 3.1.3 Hyperfine Interaction

Another important aspect to gain information on defects and their chemical environment is the study of the so-called hyperfine structure. Hyperfine interactions occur if the magnetic moment of the unpaired electron interacts with nearby nuclei that show magnetic properties ( $I > 0$ ). In this case, the magnetic field that is effective at the position of the unpaired electron consists of two contributions. Firstly, the one from the externally applied magnetic field and secondly, the other one generated from the magnetic moments of the surrounding nuclei having a non-zero nuclear spin. The hyperfine energy depends on the quantum numbers  $m_s$  and  $m_I$  and is given by

$$E(m_s, m_I) = g\mu_B B m_s + a m_s m_I - g_N \mu_N B m_I \quad (3.8)$$

where  $a$  is the hyperfine coupling constant corresponding to the spacing between the absorption lines. [27] In fact, the hyperfine coupling constant is another  $3 \times 3$  matrix that describes the angular dependence of the hyperfine interaction and is a measure of the electron-nuclear spin interaction. The result of the hyperfine interaction is that each

$m_s$ -level generally splits up into  $(2I + 1)$  levels depending on the nuclear spin quantum number  $I$ . Assuming that an electron ( $S = \frac{1}{2}$ ) is interacting with a nucleus with  $I = \frac{1}{2}$ , each  $m_s$ -level is split into two levels, corresponding to  $m_I = +\frac{1}{2}$  and  $m_I = -\frac{1}{2}$ . Figure 3.2 shows the resulting energy diagram together with the corresponding ESR spectrum.

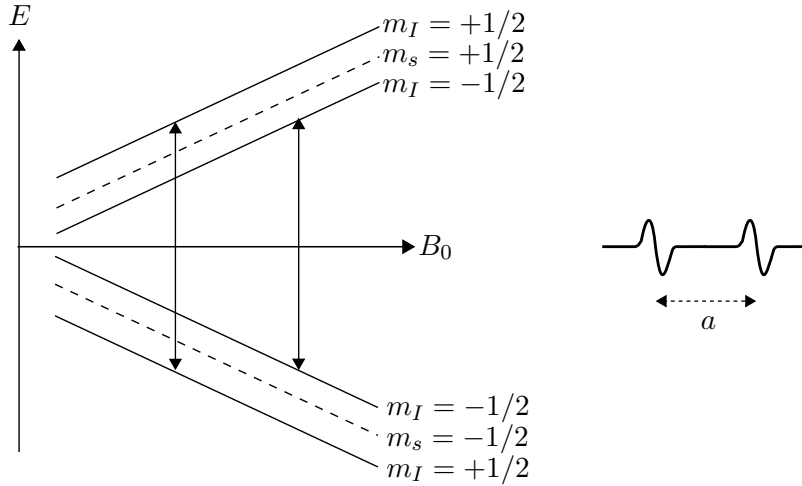


**Figure 3.2:** Energy level scheme and resulting ESR spectrum for an electron interacting with a nucleus with  $I = 1/2$ . The parameter  $a$  is the hyperfine constant describing the hyperfine splitting.

According to the selection rules  $\Delta m_s = 1$  and  $\Delta m_I = 0$ , two transitions are possible during the sweep of the magnetic field. The separation between the two absorption lines corresponds to the hyperfine splitting whose symmetry dependence can be analysed by rotation measurements. The magnitude of the splitting constant  $a$  is proportional to the probability of the electron localisation at the nucleus. The number of peaks and relative intensities give clues about which atoms and how many are interacting with the electron. Since electrons cannot be localised at a certain position but rather spread over several nuclei, there can always be a sum of nuclei interacting with the defect electron. The more nuclei affect the local magnetic field of the electron, the more complex the absorption spectrum becomes with lots of overlapping absorption lines.

### 3.1.4 ESR Setup

The aim of this section is to provide a schematic diagram of a basic ESR setup used and to explain the most important components. In figure 3.3 a schematic representation of a standard ESR setup is given. In order to establish the necessary conditions for resonance in the first instance a static magnetic field  $\mathbf{M}$  and a microwave generator  $\mathbf{G}$  have to be available. In conventional ESR setups the microwave source is a klystron usually operating in the X-band range at around 9 GHz. With the use of equation 3.7 it can be found that the magnetic field for this frequency range has to provide a value of about

0.3 T corresponding to 3000 G to allow for resonance. This static magnetic field, that has to be very stable to avoid fluctuations, is produced by an electromagnet driven with a constant current source. Apart from the static magnetic field, a second magnet is needed to sweep the magnetic field over the desired range. This second magnet is indicated in black on the right magnetic component in 3.3 and is controlled by an appropriate software.

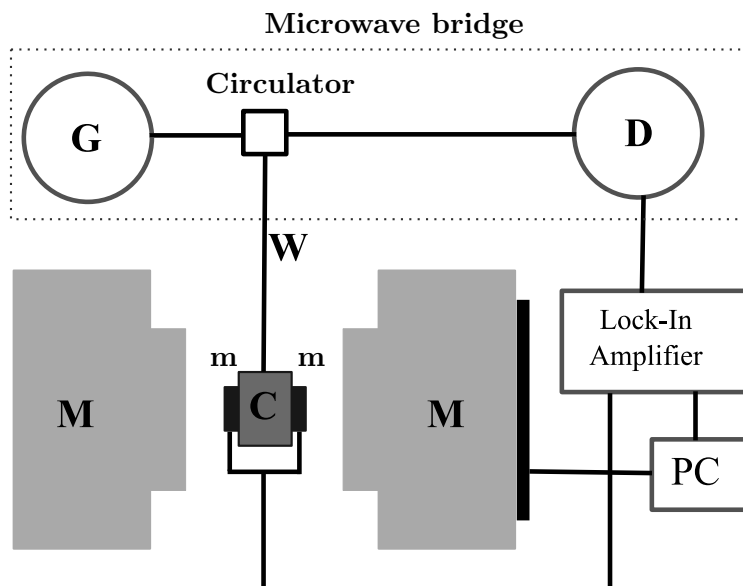


**Figure 3.3:** Schematic diagram of an ESR setup with the cavity **C** situated between the magnets **M** producing the static magnetic field and the modulation coils **m** that are used to modulate the signal. The microwave bridge is composed of the microwave generator **G**, a circulator and the signal detector **D**. The Lock-In amplifier is used to detect and measure very small AC signals.

In between the magnetic system the resonator cavity **C** connected to the microwave bridge is located. The microwave bridge consists of the microwave generator, the circulator and the detector unit. Inside the cavity, the sample is positioned at a point of maximum magnetic field and almost zero electric field, as it is the magnetic field that induces the magnetic dipole transitions between Zeeman levels. A waveguide **W** transmits the microwaves from the generator to the cavity via an iris. In order to maximise the energy density in the cavity and thereby the probability of resonance, the frequency is tuned to the resonant value. The resonance frequency is related to the dimensions of the cavity. There are always some microwaves that are reflected back from the cavity. These microwaves are then transmitted by passing the circulator towards the detector unit **D**. The detection principle is based on the measurement of changes in the intensity of the reflected radiation by means of a suitable detector, mostly a solid-state diode. If the resonance condition is fulfilled, the microwaves in the cavity are partly absorbed and as a result, a change

in detector current can be observed. Since these changes are rather small compared to the noise, a Lock-In detection is used. With a Lock-In amplifier very small AC signals can be detected and amplified based on a method known as phase-sensitive detection. Thereby, the measuring signal is filtered out at a specific reference frequency and phase while all other components are rejected. In order to get an AC signal suitable for Lock-in detection, the DC signal to the detector diode has to be modulated. This is realised by the modulation coils  $\mathbf{m}$  producing an additional third magnetic field that modulates the signal with a reference signal from the Lock-In amplifier. It has to be taken into account that the resulting signal from this detection method represents the first derivative of the absorption spectrum. Thus, the important  $g$ -value is found to be the zero-crossing of the signal. For more detailed information on the Lock-In detection principle the reader is referred to reference [29].

## 3.2 EDMR - Electrically detected magnetic resonance

After having discussed the fundamentals of ESR, the basis is set to explain the technique of electrically detected magnetic resonance. EDMR is a powerful method combining conventional ESR with the analysis of electrical transport characteristics, in particular spin-dependent electrical properties. There are different ways that the spin can affect charge carriers on their way through a semiconducting sample. These processes include spin-dependent scattering, spin-dependent tunnelling [28], and spin-dependent recombination (SDR). The latter one is the most commonly observed process for EDMR and also the one used for this work. While in ESR the resonant absorption of microwave radiation serves as a means of detection, a common method of EDMR is to observe resonant current changes due to spin-dependent recombination. Thereby the impact of paramagnetic defects along the current path through the device is detected with a selectivity for those defects directly influencing the electronic transport and recombination [30]. The measurement of a current is far more sensitive and accurate which is why the sensitivity of EDMR is elevated by orders of magnitude ( $10^6$  times [31]) compared to ESR. Moreover it can be applied on fully processed semiconductor devices independent of the sample size. Still, the spectrum and microscopic information on defects gained from EDMR measurements is equivalent to the results obtained from ESR. Thus, the results of both methods can be compared.

### 3.2.1 Spin Dependent Recombination

As the essential transport mechanism in EDMR measurements on semiconducting devices is the spin-dependent recombination, this process is explained in more detail.

---

The first model describing the phenomenon of SDR was given by Lepine, who investigated changes in the photoconductivity due to recombination of photocarriers on a silicon surface [32]. His explanation of SDR is based on the combination of the Shockley-Read-Hall recombination with the Pauli exclusion principle. The main statement of the Lepine-model of SDR is that recombination through an intermediate state can only take place if the conduction band electron and the paramagnetic defect electron do not have the same spin state. Otherwise recombination is prohibited since two electrons with the same spin state cannot occupy the same defect site. Under the condition of resonance, the spins of either electron can be flipped by absorbing a photon from the microwave source. Therefore, the number of recombination possibilities increases and a change in recombination current is observed. By using this model the predicted relative signal change was estimated to be about  $10^{-6}$  with standard X-Band conditions and at room temperature. However, this value did not match with experimental results that turned out to be orders of magnitude higher around  $10^{-4}$ . Obviously, the simple model of Lepine is too basic to explain the magnitude of the SDR effect. For more information on the Lepine model the reader is referred to reference [28] where a detailed derivation as well as a discussion is provided.

A further and more convenient model describing SDR was proposed by Kaplan, Solomon and Mott who defined the so-called KSM-model [33]. In this model the concept of a spin-pair is introduced. It is assumed that before recombination can take place, an electron and a hole get trapped in closely located states that allow for weak interaction, forming a spin-pair. This pair can recombine depending on whether it is in a singlet or a triplet state. In order to understand the behaviour of this pair-state, a two-electron-system has to be considered. Two electrons forming a pair can arrange in four possible spin configurations resulting in one singlet and three triplet states. The four configuration possibilities - each with the same probability of  $1/4$  - lead to an equilibrium concentration for the singlet and triplet states of  $1/4$  and  $3/4$ , respectively. The total spin of the triplet system has a value of  $S = 1$  while the total spin of the singlet system is  $S = 0$ . Since the spin-orbit coupling in silicon is rather weak, singlet and triplet states coexist separately and in addition recombination transitions will conserve the total spin. After a recombination event the system is without spin. Therefore, the initial configuration has to be without spin as well. This important spin conservation condition restricts the permitted state for recombination to the singlet state with  $S = 0$ . As a consequence, in a steady-state condition the portion of singlet states is less than  $1/4$  because those states readily recombine. On the contrary, the portion of triplet states exceeds its equilibrium concentration of  $3/4$  since recombinations over these states are not allowed and so these pairs remain. Under resonance the microwaves lead to spin transitions if the photon energy matches the Zeeman splitting of either the electron or the hole. Due to this flipping of the spins the

triplet pairs can be converted to singlet pairs and thereby the concentration of singlets declines to its equilibrium concentration of 1/4 implying that newly created singlet states are available for recombination. The increased population of singlets is accompanied by an enhanced possibility of recombination events. For this reason, under resonance a higher recombination rate can be achieved. Due to the resonant recombination, the total change in current constitutes the basis for the detection principle used in EDMR [34]. In general, triplet states can also be transferred into singlet states by thermal activation. However, this process can happen any time during the experiment and therefore, it is not related to the resonance condition which makes it irrelevant for the detection principle. In figure 3.4 a schematic representation of the SDR principle is provided.

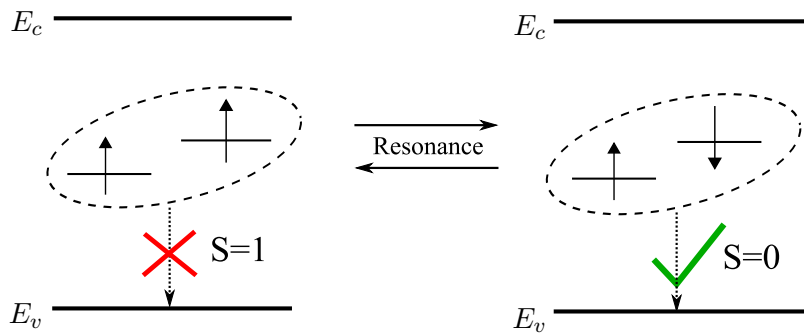


**Figure 3.4:** Resonance condition for the transfer of a triplet state into a singlet state (and vice versa) by absorption of microwave radiation.

### 3.2.2 EDMR Setup

The measurement setup for EDMR experiments is based on the setup of ESR measurements that was presented in section 3.1.4. However, it differs slightly because of the different detection principle used. In the following section, the EDMR setup used in the experiments for this thesis is described. The devices under investigation are fixed on a sample holder equipped with electrical contacts and placed in the cavity in the same manner as for ESR measurements. Instead of detecting changes in microwave absorption, current changes generated due to resonant recombination currents are recorded in EDMR. The Lock-in method is still necessary for the detection of the rather low signals. An important requirement for the detection of current changes under resonance is the generation of a constant current through the device under investigation. Therefore, the device has to be biased which is realised by using a pre-amplifier controlled by an appropriate computer program. The ideal biasing conditions of the diodes for EDMR measurements are discussed in section 3.3. The resulting current signal from the device is fed back to the pre-amplifier where it is amplified and afterwards converted into a voltage

signal. This is necessary for the lock-in detector to process the signal. In order to optimise the signal-to-noise ratio, the pre-amplifier is equipped with several band-pass, high-pass and low-pass filters that can be applied to the input current signal. In addition, an input offset is available to measure large currents in a sensitive range. After the voltage signal is transferred to the lock-in detector - where it is analysed by comparison with a reference signal - the resulting spectrum is displayed on the computer. In figure 3.5 a schematic diagram of an EDMR setup is given. The detailed measuring parameters, instruments and instrument settings used for the performed experiments can be found in the chapter on experimental results.

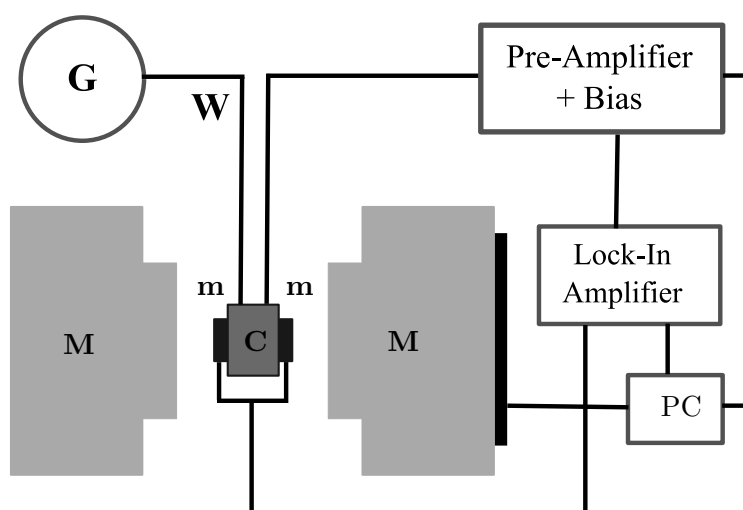


**Figure 3.5:** Schematic diagram of an EDMR setup with the cavity **C** situated between the magnets **M** producing the static magnetic field and the modulation coils **m** that are used to modulate the signal. From the microwave generator **G** the microwaves are fed into the cavity via a waveguide **W**.

### 3.3 Diodes

A diode is an important electrical component that conducts current in one direction, while it almost entirely blocks it in the other direction. This behaviour is referred to as rectification. Among other things it can be used to convert an AC into a DC current. The functionality of a diode is based on the physical property of a pn-junction, the basic unit of any semiconducting device. Therefore, it is crucial to understand the underlying physical principles of this essential junction. Detailed information on pn-junctions can be found in numerous textbooks on semiconductors such as reference [20] serving as the major source for this section. In the following a short insight into the properties of pn-junctions relevant for EDMR measurements is provided.

#### 3.3.1 Basic operation

If two semiconducting materials - one with  $n$ -type doping the other with  $p$ -type doping - are brought into contact, the so-called pn-junction is established. In order to balance out the arising concentration gradients at the junction, the electrons from the  $n$ -type material diffuse into the  $p$ -type region where they recombine with the available holes. What they leave in the  $n$ -type material are positively charged donor atoms that are spatially fixed. Likewise, the holes diffuse from the  $p$ -type into the  $n$ -type region where they recombine with the electrons leaving behind negatively charged acceptors. Due to the fixed ionised donor and acceptor atoms thus present close to the junction, an electric field is created that opposes the diffusion current. The arising electric field pushes the electrons back towards the  $n$ -region and the holes towards the  $p$ -region. When the equilibrium is reached the diffusion current originating from the concentration gradients and the drift current originating from the electric field balance each other out. Hence, in the region between the  $n$ -type and  $p$ -type material the mobile charge carriers are diffused away and only immobile donor and acceptor atoms are left. This area is referred to as the depletion region or space charge region. Across the junction, a potential difference arises that leads to the formation of the built-in voltage  $V_{bi}$ . In figure 3.6 a schematic diagram of a pn-junction together with the space charge distribution, electric field distribution and potential distribution is provided.

The width  $\mathbf{W}$  of the depletion region is given by the following equation:

$$W = \sqrt{\frac{2\epsilon(N_D + N_A)V_{bi}}{eN_DN_A}} \quad (3.9)$$

where  $N_D$  and  $N_A$  correspond to the number of ionised donor and acceptor atoms, respectively. From equation 3.9 it is evident that the lighter the doping in the respective

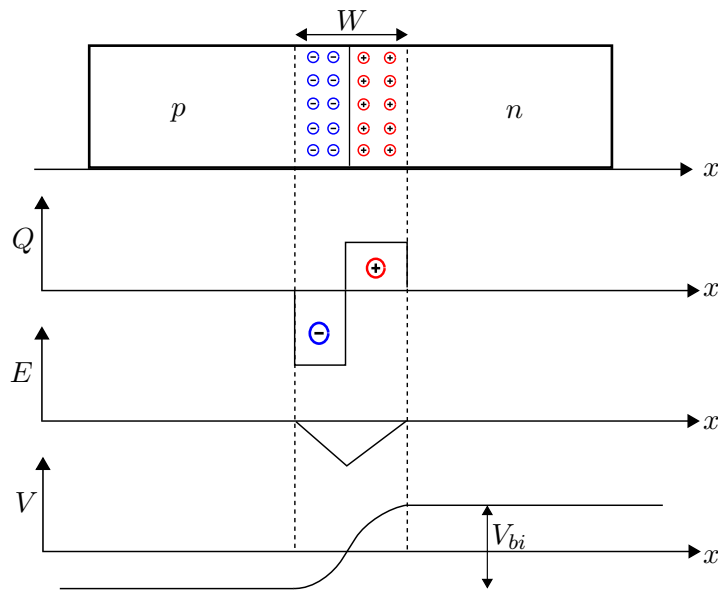


**Figure 3.6:** Schematic diagram of a pn-junction in thermal equilibrium without bias voltage. The space charge distribution, the electric field distribution as well as the potential distribution is represented.

doping region, the wider gets the depletion width in this area. These considerations are valid assuming that the diode is in a thermal equilibrium and no bias voltage is applied. However, in practice there are two important operating ranges, namely the forward and reverse bias. In figure 3.7 the discussed properties of a diode in its different operating conditions are visualised.

### Forward Bias, $V > 0$

In the forward bias state the  $n$ -doped region of the device is connected with the negative terminal and the  $p$ -doped region is connected with the positive terminal. Under these conditions, electrons and holes are driven towards the junction and the depletion region becomes narrower. The potential drop across the junction is reduced and therefore, the barrier for injection of electrons into the  $p$ -region and of holes into the  $n$ -region is lowered. By increasing the forward bias, the depletion width decreases described by equation 3.10

$$W = \sqrt{\frac{2\epsilon(N_D + N_A)(V_{bi} - V)}{eN_DN_A}} \quad (3.10)$$

where  $V$  corresponds to the applied bias voltage. Due to the reduced depletion width, the electric field decreases and so does the drift current. Thus, the current flow is dominated by the diffusion current and there is a reduced electrical resistance of the junction. A large current can flow through the device meaning that the junction is in its conducting state.

### Reverse Bias, $V < 0$

In the reverse bias state, the  $n$ -doped region of the device is connected with the positive terminal and the  $p$ -doped region is connected with the negative terminal. As a result, the electrons and holes are driven away from the junction and the depletion region becomes wider as can be seen in equation 3.10. The injection of carriers is hindered since the potential drop across the junction increases. The electric field is enhanced and thus, the drift current dominates the current flow. In the reverse bias state, only a small saturation current flows which is almost independent of the reverse bias voltage. However, the reverse saturation current shows a dependence on temperature.

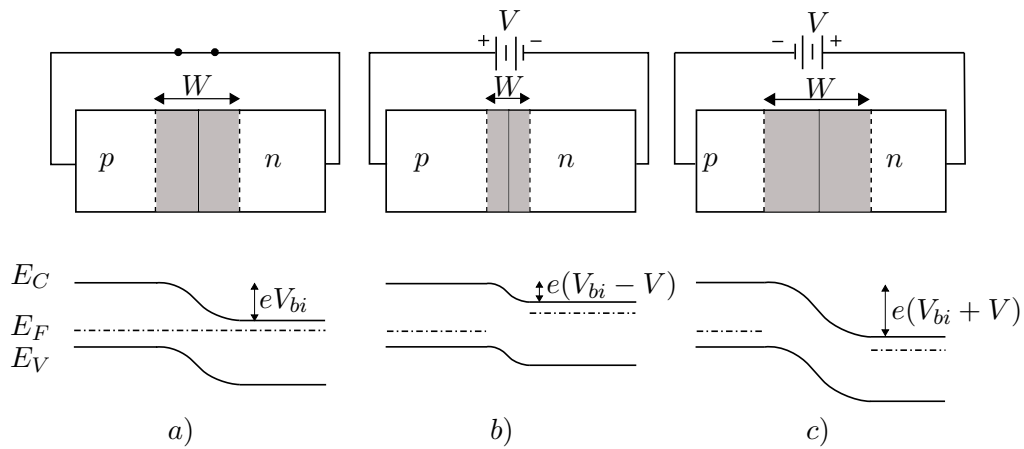


**Figure 3.7:** Schematic representation of a pn-junction and the associated energy-band diagram for **a)** zero bias, **b)** forward bias and **c)** reverse bias

### 3.3.2 Diode equation

The ideal diode equation or Shockley equation describes the current through a pn-junction as a function of the applied voltage and is given by the following expression:

$$I = I_0 \left[ \exp\left(\frac{qV}{kT}\right) - 1 \right] \quad (3.11)$$

where  $I$  is the net current flowing through the diode,  $I_0$  describes the reverse bias saturation current,  $V$  is the applied voltage and  $T$  corresponds to the temperature. Equation 3.11 describes the ideal current-voltage characteristic assuming that the only processes inducing a current through the device are drift and diffusion. In figure 3.8 the ideal current-voltage characteristic both in a linear and a semilogarithmic representation is shown.

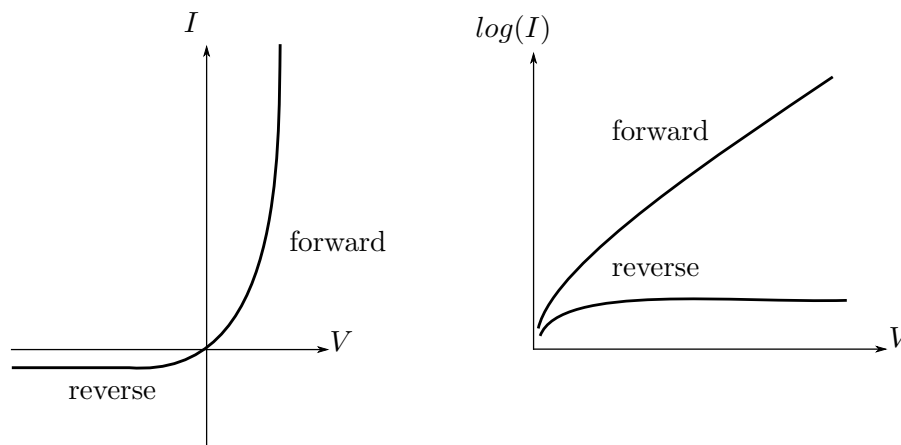


**Figure 3.8:** Ideal current-voltage characteristic in linear and semi-logarithmic dependence.

However, the relation between current and voltage shown in figure 3.8 does not correspond to the behaviour observed for real diodes (compare 3.9). The deviation from the ideal behaviour may have different reasons. Two important aspects that have to be considered in this context are the generation and recombination processes of charge carriers in the depletion region. Besides, the high injection condition as well as possible parasitic series resistances have to be taken into account in the corresponding bias regions. In addition, tunnelling, surface effects and junction breakdown have an influence on the diode characteristic [20]. The recombination processes in the depletion region have a high relevance for EDMR measurements. Generally, the net current flowing through a diode is mainly composed of two contributions: the diffusion current and the recombination current. For low diode currents - equivalent to a small forward bias - the recombination current is the dominating contribution. For higher diode currents, hence increasing forward bias, the diffusion current becomes more important [35]. The equation that describes the current

through a real diode as a function of the applied voltage more precisely yields

$$I = I_0 \left[ \exp \left( \frac{qV}{\eta kT} \right) - 1 \right] \quad (3.12)$$

where an additional parameter  $\eta$  is added. This parameter  $\eta$  is called non-ideality factor that can adopt values between 1 and 2. When  $\eta$  equals 1 the diffusion current dominates, while the recombination current dominates if  $\eta$  equals 2. For values between 1 and 2, both currents contribute comparably to the total current. In figure 3.9 a typical IV-curve in the forward bias of a real silicon diode is indicated [20]. It is important to note that only the current due to the recombination of carriers in the space charge region is spin-dependent and therefore the ideal value of  $\eta$  to maximise the EDMR signal is 2. This means that the samples under investigation need to be slightly forward biased to reach the area where the recombination current dominates and  $\eta$  approaches 2. For higher biasing voltages where the region of ideal diode behaviour is reached the EDMR signal decrease. Thus, the bias voltage regulates the diode current and hence the EDMR signal intensity can be adjusted. Apart from that, the bias voltage does also affect the area that is investigated with EDMR. The higher the forward bias, the smaller the depletion region gets and thereby the volume that can be probed decreases.

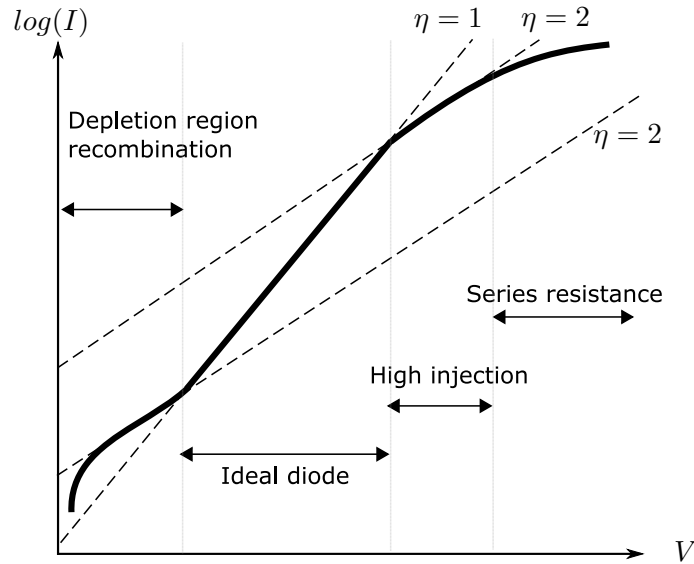


**Figure 3.9:** Semi-logarithmic scheme of a the current-voltage characteristic of a real Si diode in the forward bias regime.

## Experimental results

---

In this section, the actual measurement setup used in this work together with the utilised instruments and instrument settings are described. The devices under investigation are introduced and a description of the sample holders is given. Subsequently, the results of the SRP and EDMR measurements are presented and discussed. In addition, the IV-curves recorded to supplement the EDMR results are presented.

### 4.1 Experimental setup

The EDMR setup used to perform the experiments in this work is a self-made construction. It is composed out of several components that are arranged as presented in the previous chapter on EDMR. The whole system with the main components is shown in figure 4.1. In table 4.1 an overview of the equipment for the EDMR setup is provided. The essential details concerning the instrument settings used to achieve optimal measurement results are discussed in the following. For the calibration of the measurement system the paramagnetic substance 2,2-diphenyl-1-picrylhydrazyl (DPPH) is used. As this substance is composed of stable free-radical molecules, it provides a strong EPR signal. DPPH is a common standard used to calibrate the position of EPR signals.

**Table 4.1:** Main components of the EDMR setup

Equipment	Additional information
Microwave generator	HP 8672A Synthesized Signal Generator
Waveguide	suitable for the X-Band microwave range
Magnets	
Power supply 1	TTi QPX1200, constant current power supply for static magnetic field
Power supply 2	Laboratory power supply, to sweep magnetic field
Resonator cavity	double resonator cavity with intergrated modulation coils
Pre-amplifier	SR570 low-noise current amplifier, Stanford Research Systems
Lock-In detector	SR380 DSP Lock-in amplifier, Stanford Research Systems
Magnetometer	DRUSCH Gaussmetre
Oszilloscope	Tektronix TDS2004B
Multimeter	digital multimeter, MASTECH M3900

The frequency of the generated microwaves can be regulated with a rotary switch. For EDMR measurements, the frequency has to be tuned to its resonance value that was found to be in the range of 9.330 GHz for the present setup. Moreover, there are several possible microwave power settings. For the calibration of the system with the DPPH sample, a power of -20 dBm was used while a power of 0 dBm corresponding to 1 mW was adjusted for the measurements of the diodes. Through the waveguide, the microwaves are transmitted to the double resonator cavity where the sample is located. The modulation coils are positioned on each side of the cavity. The magnets producing the static magnetic field are driven with a constant current power supply with currents between 25 and 27 A. In order to sweep the magnetic field over the desired range, a second power supply is available. Close to the resonator cavity an NMR standard is positioned to measure the resulting field strengths that are subsequently displayed on the gaussmetre. The pre-amplifier utilised to bias the devices has a  $\pm 5V$  output and the biasing conditions are controlled by an appropriate LabView program. The resulting current signal is fed back from the diode under investigation to the pre-amplifier where it gets amplified and converted into a voltage signal. The parameters that have to be adjusted at the pre-amplifier in order to optimise the signal properties are the sensitivity range, the input offset as well as the low-pass filter settings. In general, it is intended to use the highest possible sensitivity for the measurements. In this context, the bandwidth of the respective sensitivity ranges and the signal current have to be considered. The modulation frequency of the lock-in detection was chosen to be 900 Hz for all measurements performed in this work. Since the measurement signal is modulated with this frequency, it is crucial that this frequency passes through the pre-amplifier. Therefore, the sensitivity range for all measurements was chosen to be  $10^{-7}$  A/V. From specifications in the data sheet of the pre-amplifier it is known that for this sensitivity the bandwidth corresponds to 2 kHz, meaning that a frequency of 900 Hz can still pass through. In order to measure high

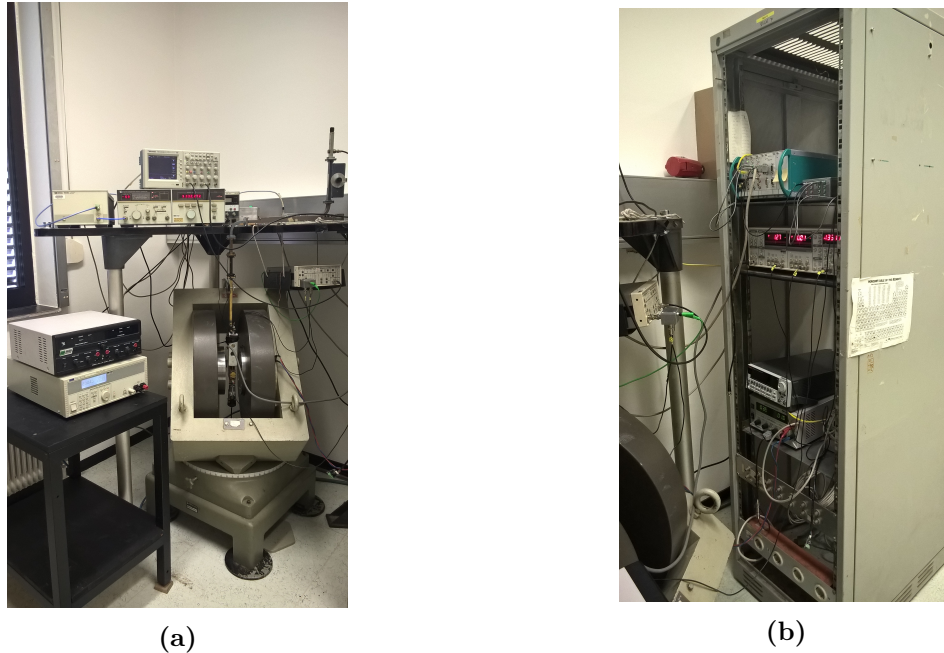


**Figure 4.1:** EDMR setup based on a continuous wave EPR setup. In picture **a** the microwave generator, the magnet system with the resonator cavity inside, the microwave bridge, the pre-amplifier and the power supply for the magnet can be seen. In picture **b** the lock-in amplifier, an analog digital converter as well as the power supply to sweep the magnetic field over the desired range can be found in the rack.

current signals in this sensitivity range, various input offsets were applied depending on the current applied. A low-pass filter was used to optimise the signal-to-noise ratio. From the pre-amplifier the signal is transmitted to the lock-in detector. In order to achieve the best results, the time constant of the lock-in detection was adjusted to 300 ms with a slope of 24 dB. Each measurement was performed by choosing the highest possible sensitivity at the lock-in detector. However, an overload status had to be avoided. The principle of the lock-in detection is based on the modulation of the measuring signal with a reference signal generated by the lock-in detector. As already mentioned before, the frequency of this reference signal was set to a value of 900 Hz. Not only the frequency of the reference signal, but also the modulation amplitude has an influence on the EDMR spectrum. Therefore, choosing an amplitude smaller than the linewidth of the EDMR signals forms a necessary precondition. Otherwise a broadening of the spectrum can be observed which is disadvantageous. In addition, the modulation amplitude affects the noise of the signal and the resolution of the spectrum. The higher the amplitude is set, the lower the noise gets because the data points are averaged over a wider range. At the same time, however, this averaging could cause a vague spectrum as signal features may disappear. A balance has to be found in the setting of the amplitude to achieve both, a good signal-to-noise ratio but at the same time a detailed spectrum without line broaden-

ing. In practice, the modulation frequency is adjusted at the lock-in detector by setting an AC voltage and measuring the corresponding AC current with a multimeter. In order to adapt the appropriate modulation amplitude, it is important to find out which current corresponds to which modulation amplitude in the unit Gauss (see 4.1.1). Concerning the lock-in detection it has to be mentioned that the signal is displayed in two channels on the computer, namely the X and Y channel. Those two output channels are phase-shifted by 90 degrees. By using a phase setting at the lock-in detector, the channel that displays the main part of the signal can be selected.

#### **4.1.1 Modulation amplitude**

In order to determine which current settings at the lock-in detector correspond to which amplitude values, an analysis of the linewidth broadening as a function of modulation current was performed. Referring to a previous study on the diodes investigated in this work [1], the appropriate modulation amplitude for EDMR measurements for these devices is 3 G. Apart from that, a modulation amplitude of 1 G is necessary for the calibration of the measurement system with DPPH. Therefore, several EPR spectra of DPPH were measured with different modulation currents ranging from 0 - 225 mA (figure 4.2a). The modulation frequency for all measurements was set to be 900 Hz. The distance between the minimum and the maximum of each spectrum  $\Delta B_{pp}$  was determined in units of the magnetic field and subsequently plotted as a function of modulation current  $I_m$  (figure 4.2b). By applying a linear fit to these data, the slope was determined exhibiting the unit of  $\frac{\text{G}}{\text{mA}}$ . The inverse value of this slope corresponds to the amount of current necessary to generate a modulation amplitude of 1 G. For the present measurement setup, an inverse slope of  $11 \frac{\text{mA}}{\text{G}}$  could be determined. The theoretical background of this measurement principle can be found in reference [26].

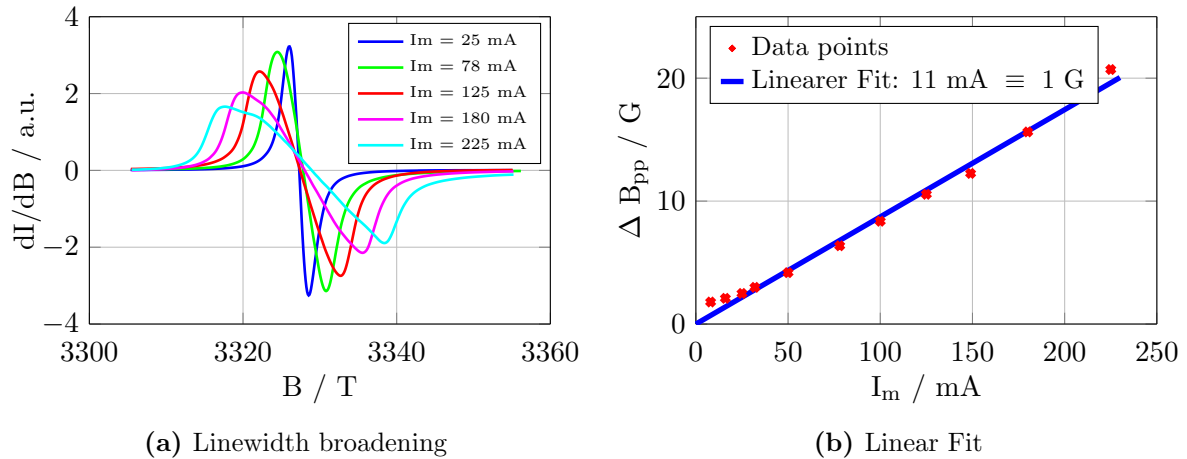


**Figure 4.2:** Analysis of modulation amplitude dependence on modulation current for a modulation frequency of 900 Hz. **a)** Several EPR spectra of a DPPH sample were measured at different modulation currents. Only 5 out of 11 curves are plotted for the sake of clarity. **b)** The distance between the maximum and minimum of each spectrum in terms of the magnetic field is plotted as a function of modulation current. With a linear fit the inverse slope that corresponds to the current yielding a modulation amplitude of 1 G can be determined.

#### 4.1.2 Calibration with DPPH

In order to receive correct results from EDMR measurements, the calibration of the measurement system forms an important requirement. A NMR standard is used to measure the magnetic field. It is positioned between the magnets close to the resonator cavity. However, the magnetic field at the position of the NMR standard does not correspond to the one effective at the position of the sample. This discrepancy in magnetic field yields a shift of the EDMR spectrum and thereby causes a  $g$ -value shift that falsifies the results. Already small differences in the magnetic field cause a shift in the zero-crossing of the EDMR signals and thereby affects the  $g$ -value determination. Since the  $g$ -value is the important parameter used to identify defects this shift has to be corrected. Therefore, a calibration has to be performed with a sample whose  $g$ -value is well known. The substance DPPH has a well known  $g$ -value of 2.0036(2) and is therefore suitable for this calibration [36]. For the calibration of the system an EPR spectrum of DPPH is recorded and the  $g$ -value determined using the resonance condition. The resulting  $g$ -value usually deviates from 2.0036. Subsequently, the spectrum is shifted until it yields again the correct  $g$ -value of DPPH. Thereupon, the shift value  $\Delta B$  is applied to the following EDMR measurements of the pn-diodes. It is crucial that the DPPH calibration is undertaken before each EDMR measurement. Otherwise, comparisons of the results for the  $g$ -values are neither comparable among each other nor with literature. To avoid any linewidth broadening, the modulation amplitude was set to be 1 G for all calibration measurements. In

figure 4.3 a DPPH spectrum without correction and the corresponding shifted spectrum after the correction are shown. In this case a shift of  $\Delta B = 2.2 \text{ G}$  has to be applied to correct the difference in the  $g$ -values.

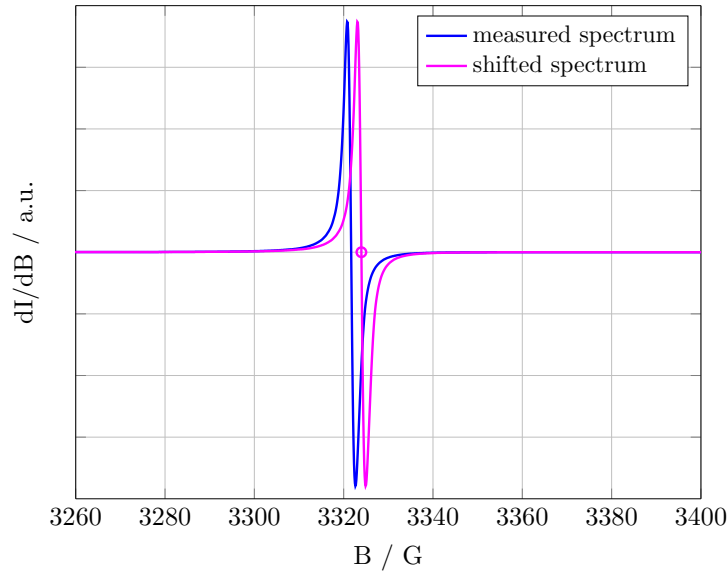


**Figure 4.3:** EPR spectrum of DPPH. The measured EPR spectrum (blue) yields a  $g$ -value of 2.0050. The whole spectrum is shifted by  $\Delta B = 2.2 \text{ G}$  (pink) in order to get a  $g$ -value of 2.0036. The pink marker indicates the position of resonance where the correct  $g$ -factor is achieved.

### 4.1.3 Sample holder

The sample holders are custom products that consist of a composite material reinforced with fibreglass. Having a length of 25 cm and a width of 4 mm wide, they are suitable to fit into the resonator cavity. There are four gold plated copper traces available for electrical contacts whereby one trace ends in a square contacting plate. On this contacting plate the device under investigation is positioned. In order to fix the diode on the sample holder an adhesive tape was used. In figure 4.4 the four metal traces on the blank sample holder as well as a pn-diode bonded to the sample holder are shown. The diodes are attached to the sample holder in a way that the pn-junction is located close to the contacting plate.

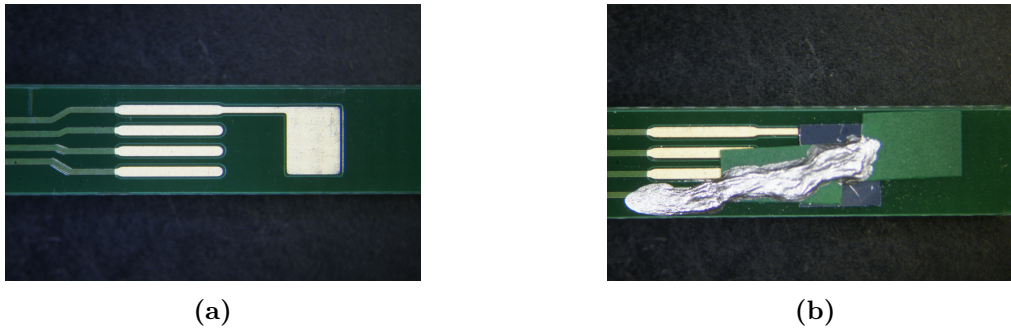


**Figure 4.4:** In figure **a)** the blank sample holder with the four metal traces and the contacting plate can be seen. In figure **b)** a pn-diode is attached to the sample holder with an adhesive tape. The electrical contacts are established with a silver paste.

Only two of the four metal traces were used to bias the diodes. In order to establish the electrical contacts, conductive silver pastes were used. Two different variants of silver pastes were available. Among the two different variants of silver pastes, one had the additional property of adhesion. Concerning the contacting of the diodes with a conductive paste it is important that the contact medium shows a low electrical resistivity and a homogeneous structure. A conventional silver paste consists of silver microparticles that are dispersed in a solvent. After the application, the solvent evaporates and a cluster of silver microparticles remains constituting the electrical contact. The contact between the individual silver particles is of vital importance in order to ensure a high electrical conductivity. The silver paste with the property of adhesion contains an additional component giving this paste the attribute of gluing. To enable a better impression of the microscopic structures, the silver pastes were investigated with a scanning electron microscope (JEOL JSM-6490LV). The resulting SEM pictures are shown in figure 4.5. In the left column of 4.5 the microscopic structure of the conventional silver paste is shown at different magnifications. Likewise, in the second column pictures of the microscopic structure of the silver paste with the adhesive property are shown at different magnifications. By comparing the overview pictures of each silver paste (4.5a and 4.5b) it becomes evident that the conventional silver paste shows a much more homogeneous structure than the silver glue where irregularities can be observed. These conditions can be confirmed by comparing 4.5c and 4.5d. Once again, the conventional paste exhibits a more homogeneous structure. In picture 4.5e and 4.5f the single particles of each paste can be observed with a high magnification. Due to the more homogeneous appearance of the conventional silver paste, it was preferably used for the sample preparation. In order to maintain optimal electrical contacts, the compliance of a rest time of at least 12 hours after application of the pastes is essential. In this way the solvents can entirely evaporate and thereby, the best possible contact is achieved.

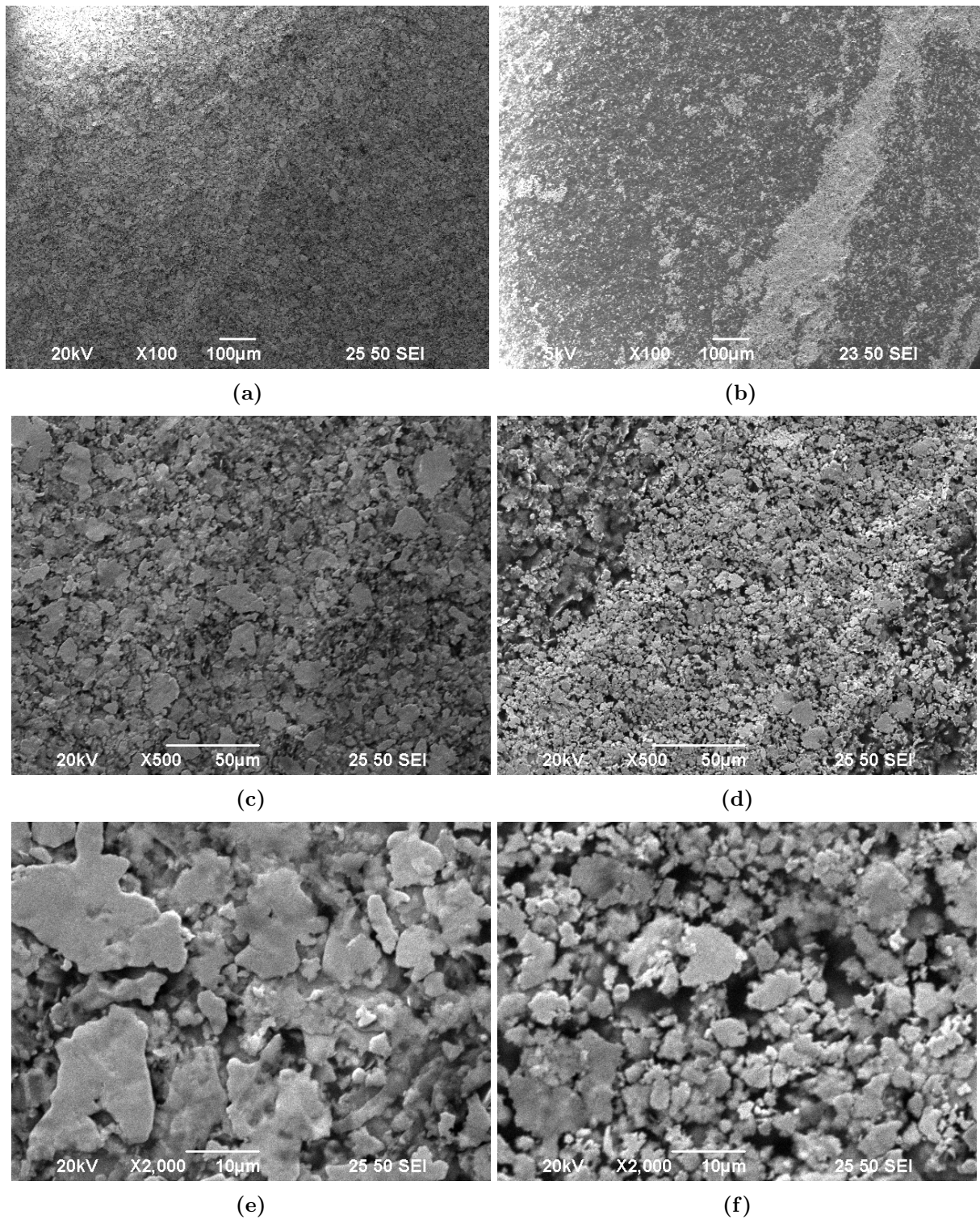


**Figure 4.5:** SEM picture of the conventional silver paste (left column: **a**, **c**, **e**) and of the silver paste with the adhesive property (right column: **b**, **d**, **f**). The pictures were taken with different magnifications and electron energies as can be seen in each picture.

## 4.2 Sample description

In the course of this study three different types of devices have been investigated that were manufactured and provided by Infineon Technologies in Villach. These devices are proton implanted silicon diodes. The objective of this work is to contribute to a better understanding of proton implantation related defects. For this reason devices were produced under conditions that should allow for the detection of these defects with EDMR. This means that a high dose of  $H^+$  has to be available in the depletion region of the diodes, since this area constitutes the volume that can be probed. A high dose of protons potentially results in an enhanced defect concentration and thereby raises the probability to detect some of the hydrogen related defects with EDMR. It has to be taken into account, that only paramagnetic defects that are directly influencing the electrical current path are detectable. The recombination probability is highest for those defects that are located in the middle of the band gap. The width of the depletion region is highly dependent on the respective doping concentrations in the  $p$ - and  $n$ -region. The higher the doping concentration, the smaller the width of the depletion region and vice versa. Therefore, it is essential that the doping of the  $p$ -region exceeds the doping of the  $n$ -region ( $p > n$ ). Nevertheless, the  $n$ -type doping should be as high as possible to allow for detection of proton implantation related defects. Otherwise the depletion region expands mainly into the  $p$ -region where the material is rather undamaged and the detection of proton related defects becomes unlikely. The high doping of the  $n$ -region close to the  $p$ -region is produced by proton implantation in a dose range that has been found to generate donors. In figure 4.6 a schematic representation how the doping concentrations allowing for defect detection with EDMR should look like is given. The detailed device parameters are presented below.

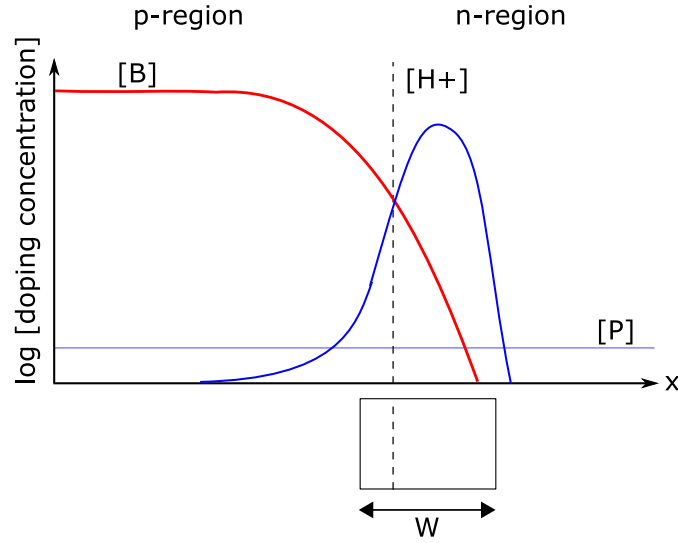


**Figure 4.6:** Example of the doping concentrations in the  $p$ - and  $n$ -region of the diodes that should allow for EDMR investigations. [B] corresponds to the boron concentration, [P] corresponds to the phosphorous concentration and [H<sup>+</sup>] indicates the proton concentration in the sample. The resulting depletion width ( $W$ ) is indicated.

The substrate of the diodes consists of float zone silicon with a thickness of  $725 \mu\text{m}$ . It exhibits a basic  $n$ -type phosphorous doping with a phosphorous concentration [P] of  $6.8 \times 10^{13} \text{ cm}^{-3}$ . The  $p$ -type doping is established by the implantation of boron with  $170 \text{ keV}$  and a dose of  $1 \times 10^{14} \text{ cm}^{-2}$ . After the implantation of boron, a heat treatment of  $1100 \text{ }^\circ\text{C}$  for  $400 \text{ min}$  is applied where boron is activated to diffuse into the bulk material. This diffusion of boron results in a  $5 \mu\text{m}$  wide  $p$ -region with a doping concentration [B] of  $10^{15} - 3 \times 10^{17} \text{ cm}^{-3}$ . Subsequently, the samples are implanted with protons ( $\text{H}^+$ ). Two different types of proton implanted pn-diodes are produced to examine whether differences in the EDMR spectra can be observed. One type of device is implanted with an implantation energy of  $450 \text{ keV}$  and a dose of  $10^{14} \text{ H}^+\text{cm}^{-2}$  (sample 1). The second type is implanted with the same implantation energy but with a higher dose of  $10^{15} \text{ H}^+\text{cm}^{-2}$  (sample 2). A third type of device is produced without any proton implantation. This sample is supposed to function as a reference enabling differentiation between proton related defects and intrinsic defects (sample REF). In table 4.2 an overview of the three different types of devices investigated in this work together with the important implantation parameters is provided.

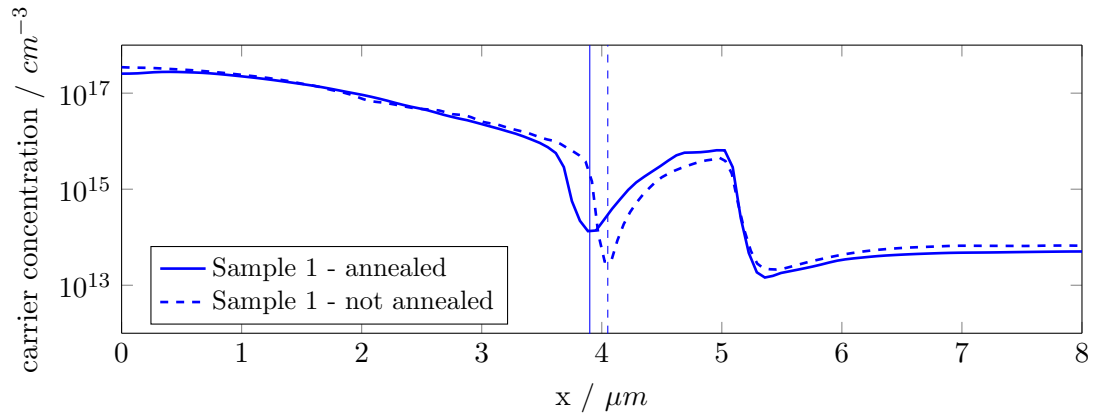
**Table 4.2:** Overview of the investigated samples

Sample	Implantation energy / keV	Implantation dose / $\text{H}^+\text{cm}^{-2}$
1	450	$10^{14}$
2	450	$10^{15}$
REF	-	-

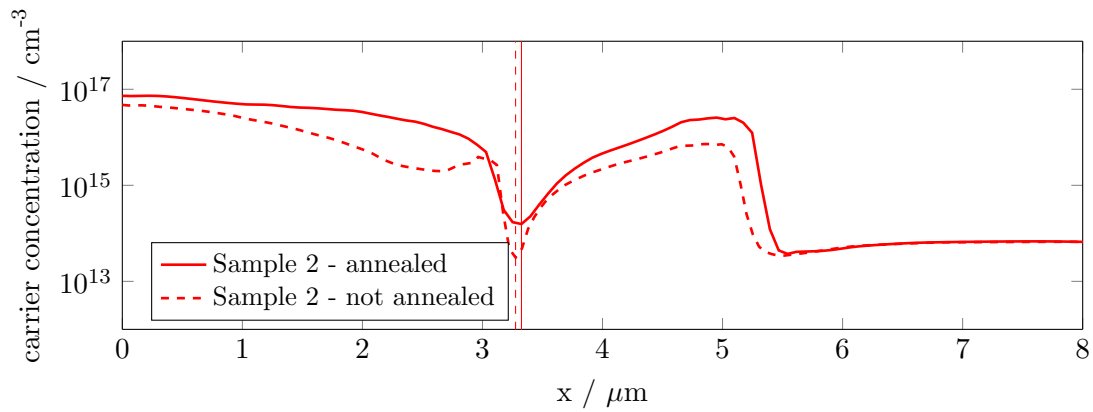
All three types of samples were measured with EDMR in the as-fabricated condition as well as after the application of different annealing steps. The annealing treatments were performed with a temperature control unit TCU 200 (prototype) from Anton Paar with a heating and cooling rate of 1 K/s. All annealing treatments were conducted under a nitrogen atmosphere. The creation of thermal donor complexes that are related to hydrogen is known to be induced by a heat treatment at temperatures around 300 °C. This is the reason why in a first step all samples were annealed at 350 °C for 15 min. In order to analyse the influence of this annealing step on the doping concentration profiles, the samples were investigated by spreading resistance profiling (SRP). The results of these SRP measurements can be found in figure 4.7. The doping profiles received with SRP show the net carrier concentration across the samples. They were obtained with a bevel angle of 0.847 degrees. The boron dopants as well as the protons were implanted from the left side into the material from the surface indicated with the x-value of 0. Hence, the *p*-region is found to be in the left area while the *n*-region is in the right area of the figures.

From the doping profile of sample REF (4.7c) it is apparent that the doping of the *p*-side clearly exceeds the one on the *n*-side implying that the depletion region will spread mainly into the *n*-region. The doping profiles of sample 1 and 2 (4.7a,4.7b) reveal that in the range of the pn-junction, hydrogen related complexes are present that are increasing the probability of hydrogen related defect detection with EDMR. However, the *n*-type doping close to the pn-junction of sample 1 and 2 is by approximately two orders of magnitude higher in comparison with the reference sample. This finding entails that the depletion regions of the proton implanted samples will be smaller and therefore, also the volume that can be probed with EDMR. The pn-junction of the reference sample (indicated by a vertical line) is located at about 5  $\mu\text{m}$  depth. The pn-junctions of sample 1 and 2, however, are shifted towards the direction of implantation. This shift is caused by the large introduction of protons in the depth of about 4 – 5  $\mu\text{m}$ . Thus, donor complexes are formed in this area and therefore, a change from *p*-type to *n*-type doping occurs. This shift is larger for sample 2 which is compatible with the 10 times higher implantation dose. By comparing the doping profiles of the annealed with the not annealed samples for each device, differences for sample 1 and 2 can be observed. In contrast, the doping profile of the reference sample seems to be rather unaffected by the annealing even though thermal donors related to oxygen may be present. In the profile of sample 1 and in particular of sample 2, it is visible that due to the annealing a shoulder on the left side of the implantation peak has developed indicating the formation of hydrogen related thermal donor complexes. In sample 1, this donor complex formation leads to a further shift of the pn-junction. By comparing the annealed and not annealed profile of sample 2 a deviation of the lines in the *p*-region can be clearly seen, which can be explained with

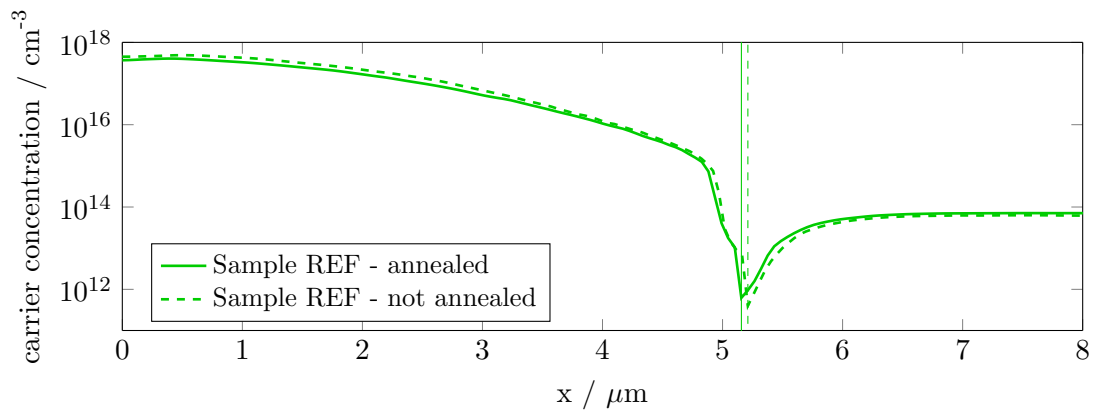
the following process. Due to the proton implantation the boron in the material is firstly deactivated and then reactivated through the annealing process. The deactivation results from the reaction of substitutional boron with silicon interstitials leading to the formation of interstitial boron known to be electrically inactive. This process is reversed by the annealing step. The reactivation of boron and the associated compensation of hydrogen related donors may be the reason for the reverse small shift of the pn-junction for sample 2. The compensation effect of boron prevails the *n*-type doping of the hydrogen related thermal donors, although the implantation dose is higher compared to sample 1.



(a) Sample 1



(b) Sample 2



(c) Sample REF

**Figure 4.7:** Doping profiles of sample 1, sample 2 and the reference sample measured by spreading resistance profiling with a bevel angle of 0.847 degrees. For each sample there is a comparison between the SRP profile of the annealed and not annealed device whereby the annealing was carried out at 350 °C for 15 min.

Subsequently, further annealing steps were applied to the three types of devices with the intention to track the defects observed and thereby determine their temperature behaviour. In total, four different annealing steps constitute the basic sequence applied to all samples in a first step. In a next step, further annealing sequences were applied to the individual samples depending on the results of the EDMR measurements of the first round. Due to the fact that the diodes have metal contacts (Al) on each side, the highest annealing temperature applied was 500 °C. For higher temperatures, diffusion processes of aluminium into the bulk of the diode may be initiated which had to be avoided. In addition to the standard EDMR measurements, tilt series were recorded to examine the symmetry of the defects observed. In table 4.3 a summary of the various annealing steps applied to the individual devices is available to provide an overview for the presentation and discussion of the EDMR results in section 4.3.

**Table 4.3:** Tabular display of the various annealing steps applied to the samples under investigation

	Sample 1		Sample 2		Sample REF	
	T / °C	t / min	T / °C	t / min	T / °C	t / min
not annealed	-	-	-	-	-	-
Basic annealings applied to all samples	350	15	350	15	350	15
	350	60	350	60	350	60
	450	15	450	15	450	15
	500	15	500	15	500	15
Annealings applied to individual samples			200	15	200	15
			300	15	300	15
			325	15	325	15
			340	15	335	15
			375	15	400	15
			400	15		
		425	15			

## 4.3 EDMR

All EDMR measurements performed in this work were carried out at room temperature. The analysis of the resulting EDMR spectra, in particular the  $g$ -value determination, was performed by using an appropriate evaluation programme written in MATLAB. The modulation amplitude was set to be 3 G with a frequency of 900 Hz for almost all measurements. Apart from the rotational measurements, all the samples were measured with the magnetic field  $B$  parallel to the crystalline [100] direction. The signals obtained from a single EDMR measurement were affected by a rather high amount of noise. In order to improve the signal-to-noise ratio and thereby enabling the analysis of the signals in terms of  $g$ -value determination, several EDMR measurements were performed successively. Subsequently, the recorded curves from each measurement were averaged. Thereby, a higher accuracy could be achieved to allow for reasonable evaluations. The error of the  $g$ -values are calculated by using the standard deviation method. In case no error is specified, the error determination was not possible due to missing data or because of a bad quality of the EDMR signal. The number of averaged curves varies from 20 up to 300 curves depending on the respective device. In particular, the proton implanted samples that did not see a temperature treatment show a very poor signal. Accordingly, the number of curves that had to be averaged was much higher. The microwave frequencies for each measurement were set to the respective resonance values that varied from sample to sample. However, they all were found to be close to 9.332 GHz. After determining the  $g$ -values of each spectrum recorded, all spectra were subjected to a frequency correction. By assuming a fixed frequency value of  $\nu = 9.332$  GHz and by using the  $g$ -value determined previously the spectra were shifted to the corresponding magnetic field values. This procedure enables a visual comparison between different spectra. All spectra presented in this chapter are frequency corrected. In the subsequent sections firstly, the EDMR results of the reference samples are discussed followed by the results of sample 1 and sample 2. The detailed measuring parameters of each measurement that are not explicitly mentioned can be found in the appendix.

### 4.3.1 Reference sample

In this section, the results of the not implanted samples are discussed. The defects observed in the reference samples are assigned to be intrinsic and not related to hydrogen. The results of the reference samples facilitate the interpretation of the EDMR results of sample 1 and 2. For reasonable EDMR measurements the diodes under investigation have to be forward biased. In order to find the optimal biasing conditions, IV-characteristics were recorded for each device. In figure 4.8a a logarithmic display of the IV-characteristics

of the reference samples subjected to the basic annealing steps is shown.

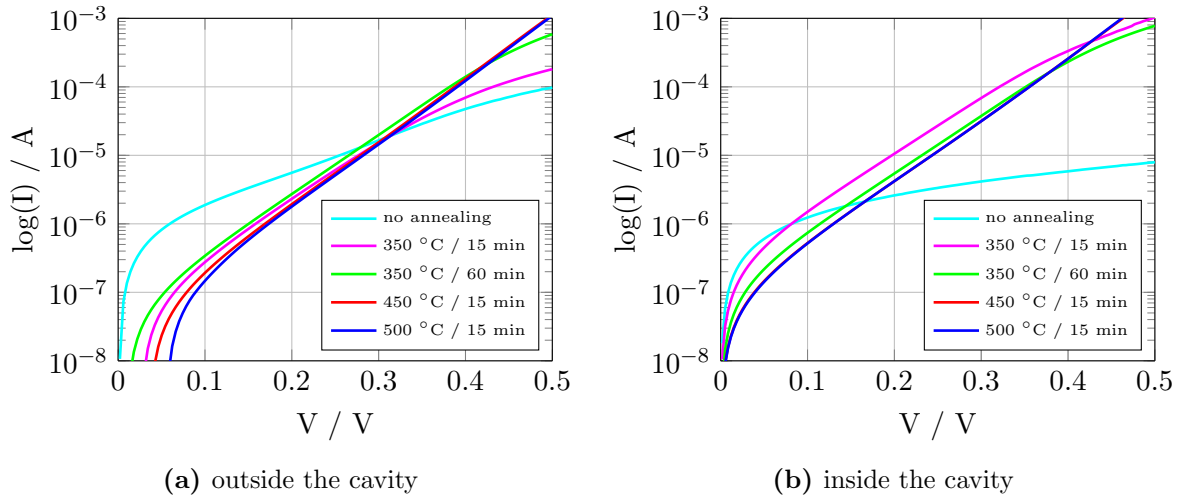


**Figure 4.8:** Logarithmic display of the IV-characteristics of the reference diodes outside the cavity and inside the cavity hence under measurement conditions.

The IV-curves of the annealed samples all show a very similar behaviour while the not annealed sample slightly differs. In order to obtain a high EDMR signal, each device is slightly forward biased to a voltage region where the non-ideality factor is close to the value of 2, meaning that recombination is dominating the current. The voltage range where this condition applies for the reference samples can be assigned between 100 and 300 mV. In order to determine the dependence of the EDMR signal on the biasing conditions more accurately, a voltage dependent EDMR measurement has been performed. This measurement is explained by using the example of the reference sample annealed at 500 °C for 15 min. In total, seven different bias voltages ranging from 78 mV up to 309 mV were applied and for each voltage setting 5 EDMR curves were averaged. The resulting signals are visible in figure 4.9a. With increasing bias voltage, the signal firstly grows but then drops after a critical value is reached. According to these results, the highest signal is achieved for bias voltages between 157 mV and 227 mV. However, a further aspect has to be taken into account concerning the optimal bias setting, namely the signal-to-noise ratio for which a high value is desirable. Therefore, in figure 4.9b the signal height (peak-to-peak) as well as the signal-to-noise ratio for the respective bias voltages are plotted. Both, a high signal and a high signal-to-noise ratio are necessary for an optimal EDMR signal output. Hence, a good balance has to be found. Consequently, the bias voltage for this sample is set to a value of 157 mV resulting in a current of 5  $\mu$ A through the device. Even though this voltage dependent measurement of the reference sample annealed at 500 °C for 15 min only serves as an example, it reflects a trend that could also be observed in the other reference samples. Generally, for the bias voltages generating a current of 5  $\mu$ A,

the highest EDMR signal as well as a good signal-to-noise ratio could be obtained. For this reason, the bias voltages in all EDMR measurements performed with the reference samples were chosen to generate a current of  $5 \mu\text{A}$  through the device.

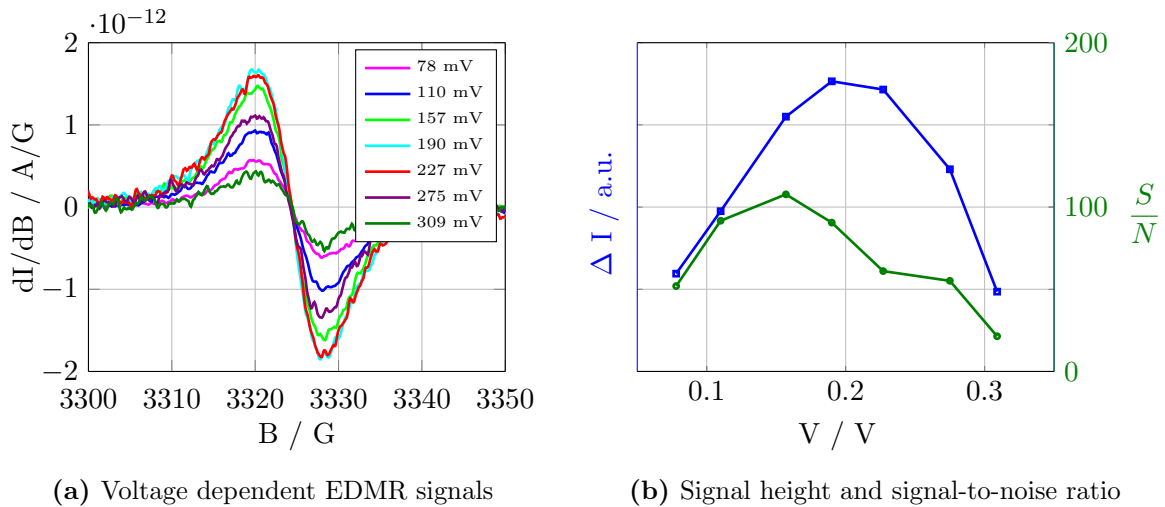


**Figure 4.9:** Dependence of EDMR signal height and signal-to-noise ratio on the bias conditions for sample REF annealed at 500 °C for 15 min

The current of  $5 \mu\text{A}$  was determined under measurement conditions, meaning that the diode is positioned in the resonator cavity and the magnetic field as well as the microwave radiation is applied. Interestingly, by considering the IV-curve of the sample annealed at 500 °C for 15 min it becomes apparent that a voltage of 157 mV does not result in a current of  $5 \mu\text{A}$ . An influence of the EDMR measurement conditions, in particular, the one of the microwave radiation is assumed. Therefore, a further IV-curve was recorded with the sample located inside the cavity under measurement conditions. The resulting IV-curves can be found in figure 4.8b. In fact, by comparing figure 4.8a and 4.8b, a slight shift of the IV-curves to higher values can be determined. A possible explanation for this shift of the IV curves towards higher values can be found in the rectification ability of diodes. In the last section of this chapter 4.4, this effect is discussed in a more detailed way.

In figure 4.10 the EDMR results of the reference samples that have been subjected to the four basic annealings and the not annealed sample are presented.

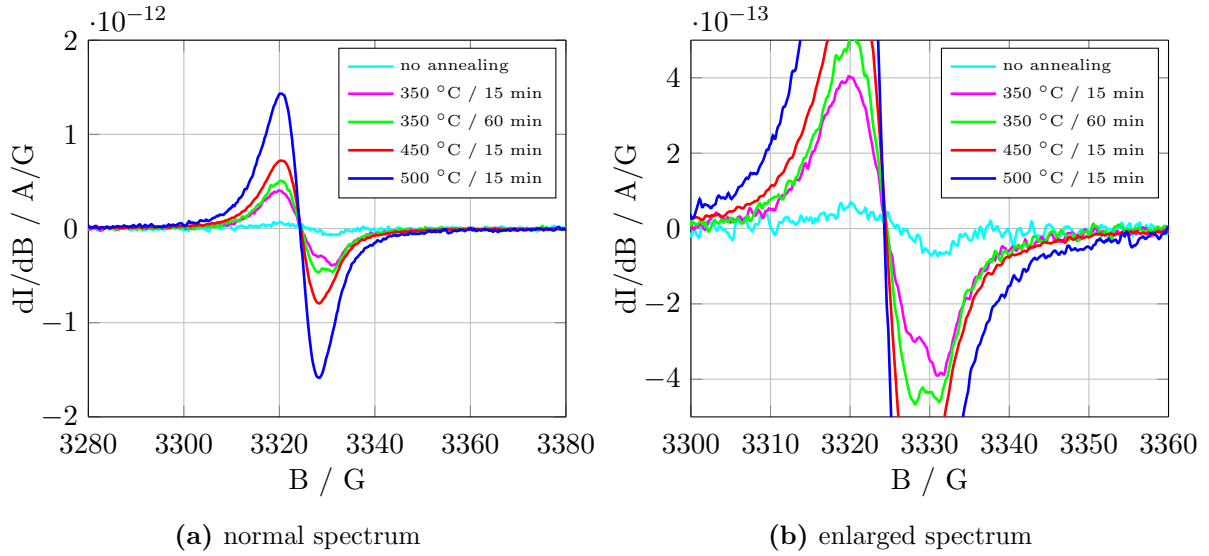


**Figure 4.10:** EDMR signal of the reference samples subjected to the basic annealings and without annealing in a normal and enlarged representation

The not annealed sample shows only a rather poor signal where the zero crossing lies at about 3326.4 G resulting in a  $g$ -value of 2.0045(4). Due to the fact that this EDMR signal exhibits a high amount of noise these values have to be treated with caution since they contain an error.

The reference sample annealed at 350 °C for 15 min has a more significant EDMR spectrum featuring a peak with a shoulder. The occurrence of this shoulder indicates that at least two different defects are present that are detectable with EDMR. One of them apparently arises due to the annealing. The zero crossing of this curve is found at 3324.9 G with a  $g$ -value of 2.0055(3). This  $g$ -value cannot be clearly assigned to one of the two defects since their spectra obviously superimpose each other.

In order to investigate the effect of a longer annealing time for the same temperature of 350 °C, a reference sample was annealed for 60 min. The resulting EDMR signal reveals again two peaks. However, the relative intensities of these two peaks have changed meaning that the shoulder on the left side has increased. More of the annealing induced defect seems to be generated relative to the other defect in the longer annealing time. For this annealing step, the  $g$ -value equals 2.0055(3) with the zero crossing at 3324.5 G. From now on, the defect that arises with temperature (left peak) is termed defect "A" to enable an easier explanation of the EDMR spectra. Unfortunately, the spectra of the defects overlap also for this sample but an attempt was made to extract the  $g$ -value of the second peak on the right. For this reason a Lorentzian fit was applied to the signal of defect A and subsequently subtracted from the whole spectrum. The EDMR signal of the second peak remains, out of which the  $g$ -value can be determined. It equals 2.0026 whereby the zero crossing is at 3329.4 G. By comparing the EDMR signal of the not

annealed sample with the samples annealed at 350 °C (pink, green), it can be assumed that the defect discovered in the not annealed sample corresponds to the second peak on the right in the annealed curves. However, the  $g$ -values do not match. Nevertheless, it cannot be excluded that these signals have the same origin, especially because the rather vague signal of the not annealed curve cannot be evaluated properly.

In the EDMR signal of the reference sample annealed at 450 °C for 15 min one peak is primarily observed. However, by taking a close look the presence of the second peak can still be recognised by the bulge of the curve in the range where the peak was located before. The  $g$ -value for this sample is determined to a value of 2.0056(3) with the zero crossing at 3324.4 G.

Finally, by considering the signal of the reference sample annealed at 500 °C for 15 min a single EDMR signal is clearly visible. At this point, the spectrum seems to be dominated by the defect termed A. The question whether the second defect has dissolved, transformed into an other defect or its signal has been just overlaid by the high signal of defect A cannot be stated without any doubt. No presumption can be made that it is only one defect generating this signal. The  $g$ -value for this sample equals 2.0057(3) with the zero crossing at 3324.3 G.

Summing up these results, one defect is present already before the annealing exhibiting a  $g$ -value of about 2.0045. This defect seems to be rather unaffected by the annealing. In the course of the annealing a second defect - termed A - arises with an associated  $g$ -value of about 2.0055. The signal intensities of defect A for each annealing step grow constantly with temperature, but cannot be used for a direct quantitative evaluation of the defect concentrations. However, a general trend can be deduced from the signal heights: with higher annealing temperature and a longer annealing time, the signal of defect A increases. For annealing temperatures up to 450 °C a second signal is present with a  $g$ -value of about 2.0026. This suggests that a second defect is present in this temperature range. At 500 °C this signal disappears and the spectrum is dominated by defect A.

### **Emergence of defect A**

As illustrated in figure 4.10 the signal of defect A seems to arise and increase with higher annealing temperatures. For a better understanding of this annealing temperature dependence, several further annealing steps were applied to the reference samples (see table 4.1). The applied temperature range extends from 200 °C up to 400 °C, while the annealing time was set constant at 15 min for each temperature. The resulting EDMR signals can be observed in figure 4.11.

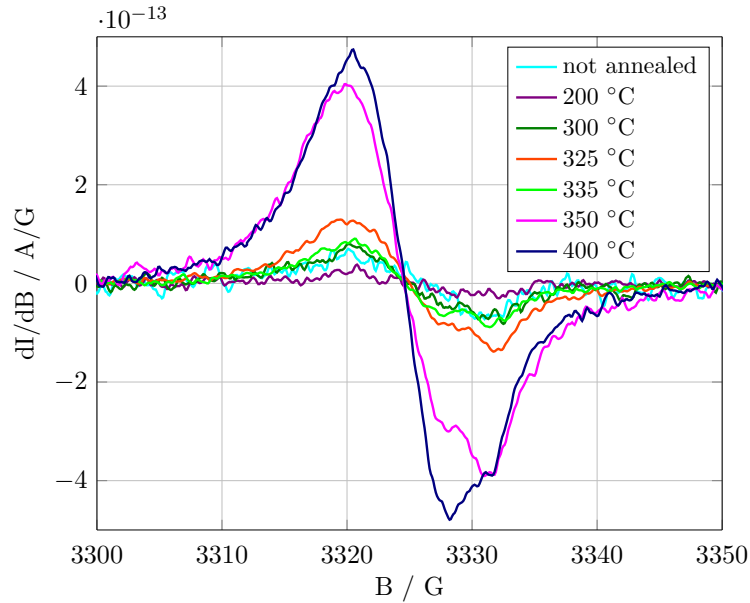


**Figure 4.11:** EDMR signals of the reference sample for the investigation of the emergence of defect A

All available EDMR signals of the reference sample up to 400 °C are displayed as in this range the development of the shoulder peak is traceable as well as the shift of the peak intensities to each other. For the annealing temperatures up to 300 °C, only a rather vague EDMR signal could be recorded. Concerning the emergence of defect A, no clear statement can be made for these annealing temperatures. However, the signals for 200 °C and 300 °C seem to correspond with the one recorded for the not annealed sample. Apparently, up to 300 °C no essential processes related to defect formation or dissociation are initiated in the devices. The EDMR signal in general, as well as the signal of defect A, start to arise at a temperature of 325 °C where a significant EDMR signal can be obtained. As expected from the previous results, the signal reveals two peaks where the right peak is significantly higher. Accordingly, the  $g$ -value equals 2.0052(3) and is rather dominated by the peak on the right. By comparing the signal for the 350 °C with the one for a 400 °C anneal a significant change in the relative intensities of the two peaks can be identified. In the case of the 350 °C anneal, the right peak is dominating the spectrum and defect A is only apparent by a small shoulder. In the case of the 400 °C anneal, the intensity relation is exactly the opposite. Interestingly, the  $g$ -values of both curves equal 2.0055(3). According to these results, it becomes evident that defect A is formed at a temperature around 325 °C. Subsequently, its concentration constantly increases for higher annealing temperatures. In all performed EDMR measurements the output signal corresponds to the first derivative of the absorption spectrum due to the lock-in detection used. By integrating this signal once the actual absorption spectrum is obtained. When this absorption signal is integrated for a second time a value for the

recombination current can be estimated. This recombination current can subsequently assumed to be proportional to the effective defect concentration in the device. In order to describe the temperature behaviour of defect A more accurately, the recombination current is evaluated for the temperature steps from 300 °C up to 500 °C and thereupon plotted logarithmically versus the inverse of the temperature. In this way an Arrhenius like plot is established as shown in figure 4.12. A clear tendency can be derived from figure

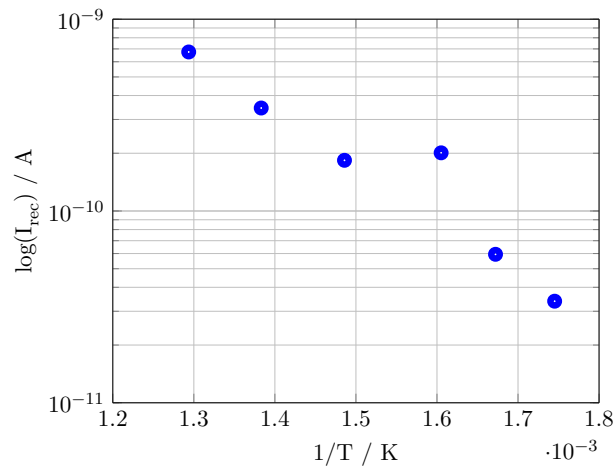


**Figure 4.12:** Arrhenius plot of the recombination currents determined for the reference sample subjected to different annealing treatments.

4.12. With increasing annealing temperature the effective defect concentration increases, thus, more of defect A is formed. A thermally activated process could be assumed from this dependence. However, it has to be taken into account that at least two different defects contribute to the EDMR signals and therefore the recombination current includes information on more than one defect. From figure 4.12 only a trend can be deduced.

### Tilt series of the reference sample

The performance of a tilt series yields information on the symmetry properties of defects. In case of two defects showing individual symmetry dependences, a tilt series can be used to deconvolve the respective EDMR signals. The evaluation of the resulting  $g$ -values of each defect can serve as a further means to identify defects. With the intention of separating the two peaks that occur in the EDMR signal of the reference samples, a tilt series was performed with the sample annealed at 350 °C for 60 min. This sample is suitable for the tilt series as in the corresponding spectrum the two peaks are clearly visible. In the course of the tilt series, the device in the resonator cavity is rotated in 10° steps from 0 - 90° between the [100] axis and the magnetic field  $B$ . An illustration of the whole tilt series is presented in figure 4.13.

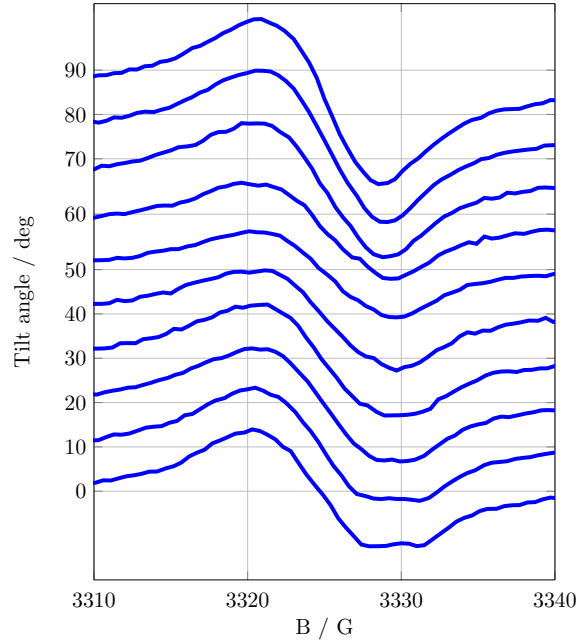


**Figure 4.13:** Tilt series of the reference sample annealed at 350 °C for 60 min. 0 deg corresponds to the [100] direction

The expectation that the two signals split up under the rotation of the sample proved to be wrong. In fact, the result was the opposite. By analysing the signals for 0-30°, a shift of the right peak into the signal of defect A can be tracked. For the tilt angles of 0° and 10° a double peak is clearly visible. For 20° and 30°, however, the two peaks start to merge. For higher angles, it is only the single signal attributed to defect A that is visible anymore. These results lead to the conclusion, that the defect generating the right peak obviously exhibits an anisotropic symmetry dependence. Unfortunately, the  $g$ -values of this defect cannot be evaluated properly from the tilt series results and therefore no further statement can be made concerning the origin of this defect. The signal of defect A, however, indicates an isotropic behaviour as all  $g$ -values evaluated from the curves shown in figure 4.13 are found to be close to a value of 2.0055. The detailed results of the  $g$ -value evolution of the tilt series can be found in figure 4.14.

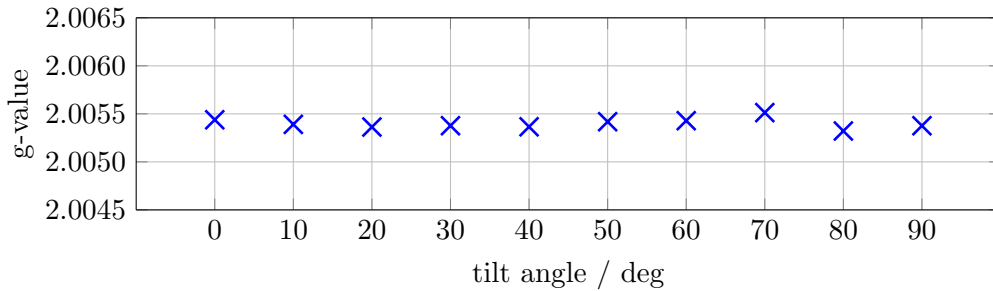


**Figure 4.14:**  $g$ -value dependence of defect A in the reference sample.

Before presenting the results of sample 1, a short summary of the results of the reference sample is provided. One defect is already present without the annealing. This defect has a  $g$ -value of 2.0045 and it is assumed to be intrinsic. One defect, termed A, is temperature induced and its emergence can be specified to a temperature of about 325 °C. The  $g$ -value of defect A equals 2.0055 and its symmetry dependence is found to be isotropic, thus independent of the rotation angle. In the temperature range between 350 °C and 450 °C, a second peak can be observed in the EDMR spectra leading to the assumption that at least a second defect is present. The  $g$ -value of this defect is evaluated to be about 2.0026. From the tilt series an anisotropic symmetry dependence of this second defect could be observed as the position of the respective signal varies under rotation. However, no more information on the  $g$ -value could be obtained since the signal merges with the one of defect A preventing a detailed  $g$ -value analysis. In addition, it cannot be clearly stated whether this second defect corresponds to the one observed without annealing, even though the positions of the peaks seem to coincide.

### 4.3.2 Sample 1

In the following, the results of sample 1 - implanted with the lower dose of  $10^{14}$  H<sup>+</sup>/cm<sup>2</sup> - are presented and discussed. Due to the implantation with protons a different IV-characteristic of these devices is expected compared with the ones of the reference sample. In order to verify and visualise this assumption and moreover to determine the optimal biasing conditions, IV curves of every device subjected to the basic annealing steps were recorded outside as well as inside the cavity. The results can be found in figure 4.15.

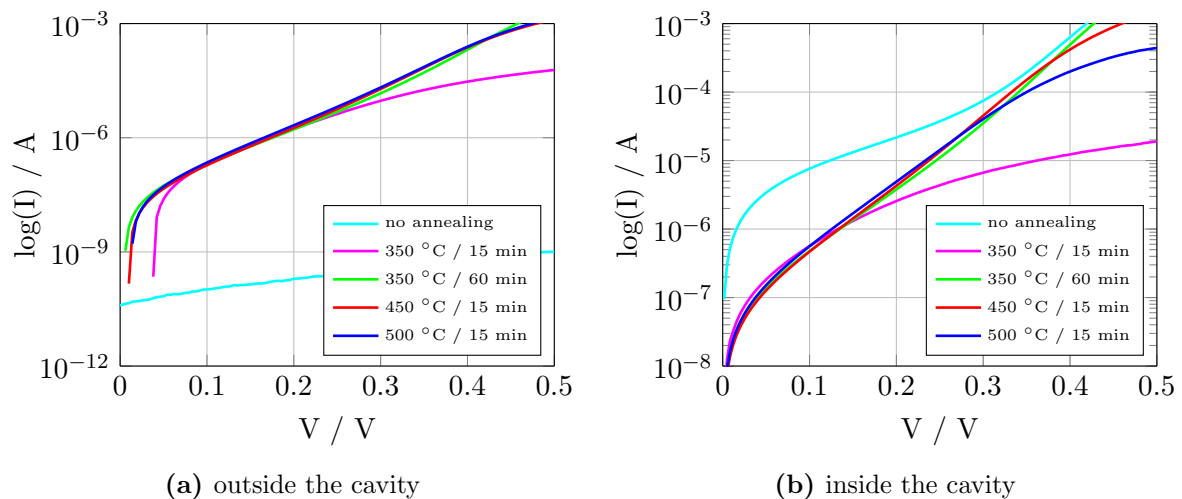


**Figure 4.15:** Logarithmic display of the IV-characteristics of sample 1 outside the cavity and inside the cavity (under measurement conditions).

A clear difference between the behaviour of the not annealed sample and the ones subjected to an annealing can be observed in both cases. Due to the implantation with protons a high amount of defects is introduced in the devices. By performing a subsequent annealing, the damaged regions of the material can be cured to a certain degree and thereby the number of defects is reduced. The annealing step is missing for the not annealed device which could be the reason why the resulting IV curve differs sharply from the ideal diode behaviour. In addition, the IV-curve of the sample annealed at 350 °C for 15 min apparently differs from the other curves. It is very likely that this behaviour is caused by a contacting problem. In order to determine the best biasing conditions for sample 1, another voltage dependent EDMR measurement was performed with the sample annealed at 350 °C for 15 min. Four different voltages were applied between 50 mV and 200 mV since this range corresponds to the area where the optimal bias conditions are expected. For each device 10 EDMR signals were averaged. The results are presented in figure 4.16. By looking at figure 4.16a a high signal for 155 mV and 188 mV can be observed. If moreover the signal-to-noise ratio is taken into account (4.16b) the optimal bias voltage for this device is found to be at 155 mV. This voltage generates a current of 5  $\mu\text{A}$  through the device. From this voltage dependent measurement a trend is deduced. Therefore, the bias voltage in all EDMR measurements of sample 1 was chosen in a way to generate a current of 5  $\mu\text{A}$  through the device. One exception is the not annealed sample, where a different voltage was found to generate an optimal signal output. This is in accordance with the data obtained for the electrical characteristics (figure 4.15b).

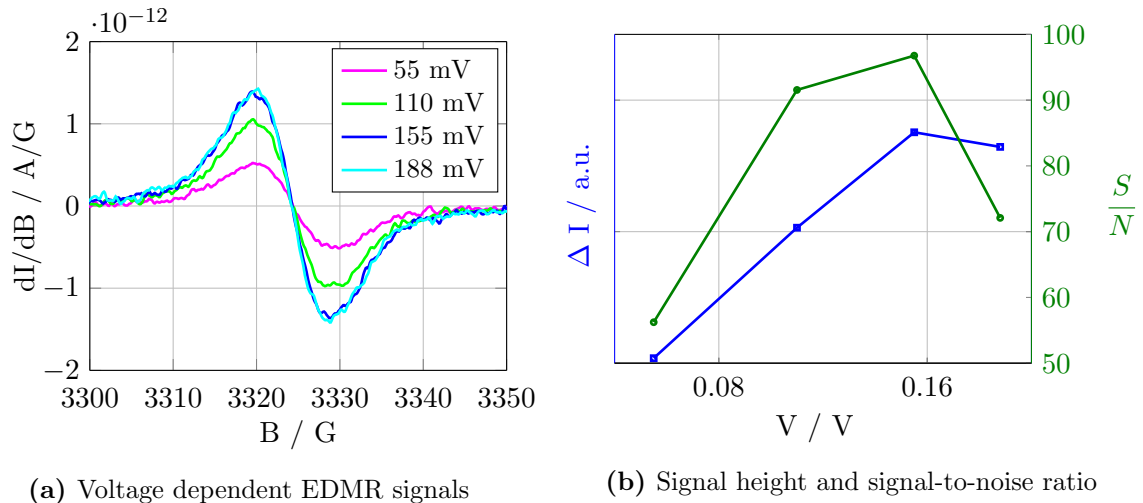


**Figure 4.16:** Dependence of EDMR signal height and signal-to-noise ratio on the bias conditions for sample 1 annealed at 350 °C for 15 min

In the following, the results of the EDMR measurements of sample 1 are presented. As in the case of the reference sample, four basic annealings were performed and the resulting

EDMR signals evaluated. The resulting EDMR spectra are displayed in figure 4.17.

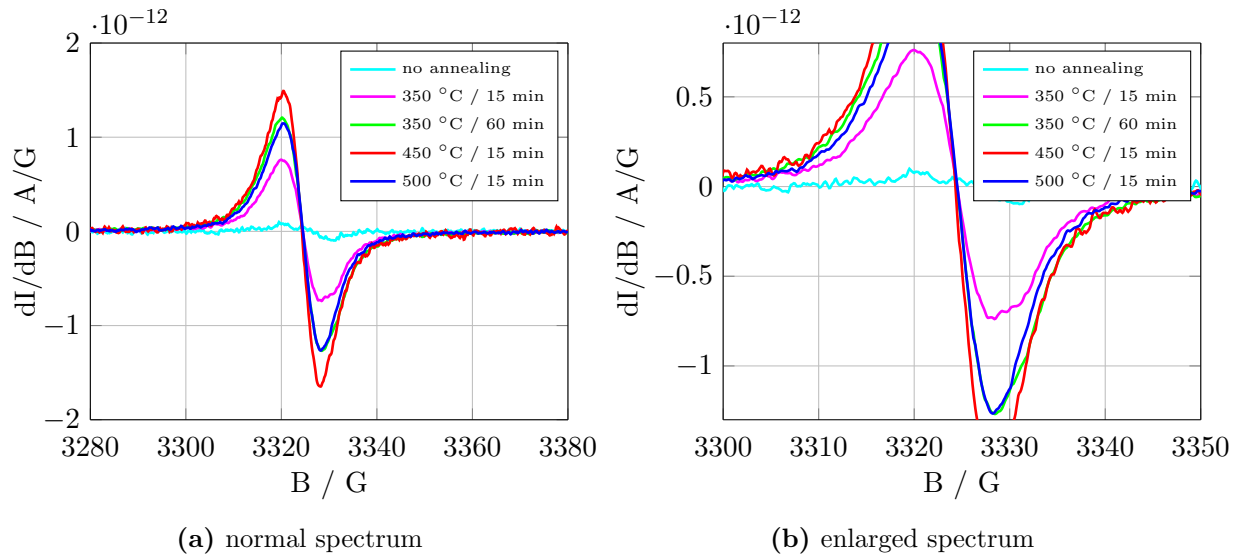


**Figure 4.17:** EDMR signals of the sample 1 subjected to the basic annealings and without annealing in a normal and enlarged representation

Analogous to the reference sample, the not annealed device shows a poor signal. The  $g$ -value can be determined to a value of 2.0044(4) with the zero-crossing at 3326.4 G. By comparing this value with the one found for the reference sample, a presence of the same defect in both not annealed devices can be assumed. Thus, this defect seems to be independent from the proton implantation, at least in case of this implantation dose.

The analysis of the sample annealed at 350 °C for 15 min reveals that also in sample 1 a defect arises with the annealing. It is very likely that it is the same defect as in the reference sample since the  $g$ -value equals 2.0056(3) with the zero-crossing at 3324.6 G. For this reason, it is assumed that defect A is also present in sample 1 created with the annealing. By taking a closer look at the EDMR signals for the respective samples annealed at 350 °C for 15 min, a further interesting similarity between the reference sample and sample 1 can be noticed. In both cases the presence of a double peak can be observed. However, the double peak is less distinct in sample 1. In order to determine whether a second peak is really present in sample 1, the EDMR measurement was repeated with a higher resolution. Hence, the modulation amplitude was set to a value of 1 G. In figure 4.18 the results of the measurements with a modulation amplitude of 3 G and 1 G are compared. The normalised EDMR signals are displayed to allow for an easier comparison of both signals. From figure 4.18b it is clearly evident that a second peak is present and in addition it seems to appear at the same position as in the reference sample. Thus, there is a strong suspicion that it is the same defect as in the reference sample. To quantify this presumption and to enable a comparison with the reference sample the

$g$ -value is evaluated as before. Therefore, a Lorentzian fit is applied to the signal of defect A and subtracted from the spectrum. As a result, the  $g$ -value of the second peak can be determined to a value of 2.0028 with the zero-crossing at 3329.1 G. This value matches with the one for the reference sample (2.0026) considering the experimental error. This confirms the assumption that in the reference sample and in sample 1 the same defects are present.

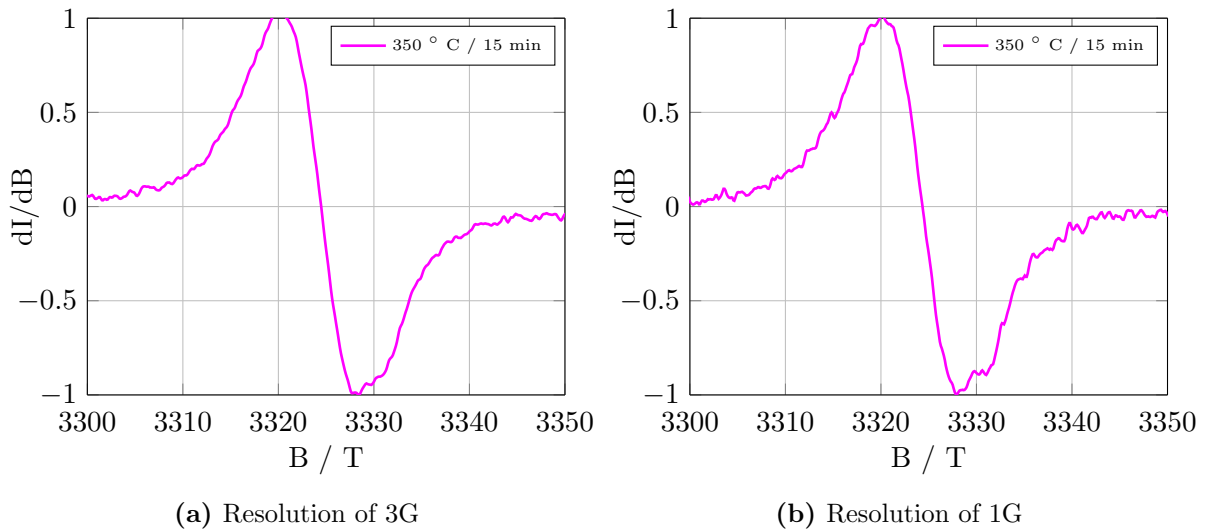


**Figure 4.18:** Comparison of EDMR signals of sample 1 annealed at 350 °C for 15 min with two different resolutions of 3G and 1G.

The effect of a longer annealing time for the same annealing temperature can be observed by analysing the EDMR signal of the sample annealed at 350 °C for 60 min. In contrast to the reference sample where the relative intensities of the two peaks changed with a longer annealing time, the second peak almost disappears in sample 1 and is barely visible in the spectrum. The zero-crossing is at 3324.4 G resulting in a  $g$ -value of 2.0056(3).

Despite a change in the signal height, a further feature cannot be obtained in the EDMR signal of sample 1 annealed at 450 °C for 15 min. The  $g$ -value of this signal is determined to be 2.0057(3). The second peak is not visible anymore. Probably, this can be explained by the fact that it is superimposed by the high signal of defect A. Finally, the EDMR signal of the sample annealed at 500 °C for 15 min delivers a  $g$ -value of 2.0056(3).

By integrating the EDMR signals displayed in figure 4.17 twice, a value for the recombination current can be estimated which in turn is assumed to be proportional to the effective defect concentrations. In figure 4.19 the results of the evaluation of these recombination currents with respect to the annealing temperature are presented. To enable an easier comparison the values for the recombination currents have been normalised to the recombination current of the sample annealed at 350 °C for 15 min. By comparing the results for the annealing temperature of 350 °C, an increase of the signal can be noticed in

case of a longer annealing time. The signal is highest at 450 °C and then drops at 500 °C. However, these results do not allow any accurate prediction on the development of the defect. More data for each annealing step would be necessary to gain a better insight into the behaviour of the defects. Only a trend of the development can be deduced.

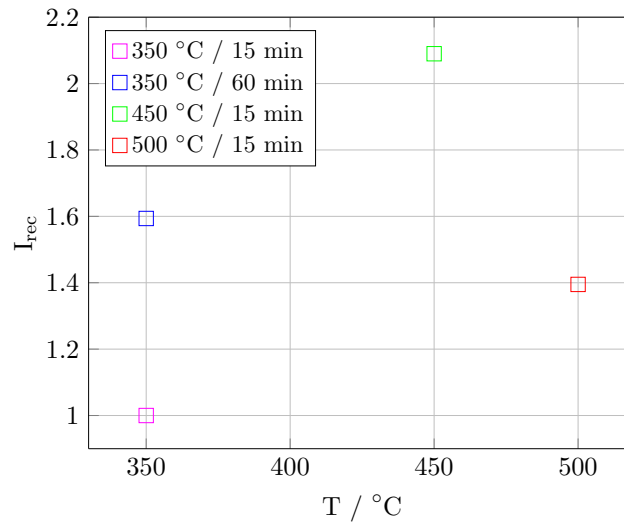


**Figure 4.19:** Recombination currents of sample 2 in terms of the annealing parameters. The values for the recombination current have all been normalised to result for the sample annealed at 350 °C for 15 min.

To conclude the essential findings from the EDMR measurements of sample 1, the striking similarities with the results of the reference sample have to be emphasised. Even though sample 1 has been implanted with protons and therefore clearly differs from the reference sample concerning the SRP results, in the EDMR measurements mainly the same features can be obtained. The not annealed devices, both of the reference sample as well as from sample 1, provide a poor signal. However, the  $g$ -values do not deviate much from each other with the one of the reference sample at 2.0045 and the one of sample 1 at 2.0044. This leads to the assumption that these signals may have the same origin. A further accordance between sample 1 and the reference sample is the emergence of a defect with the annealing and the occurrence of a double peak for the devices annealed at 350 °C. The  $g$ -value of the second peak is assessed to be 2.0028 another very similar result compared with the one of the reference sample which was found to be 2.0026. Apparently, this defect also seems to exist in both types of devices, although the behaviour is different regarding the ratio of the relative intensities of the two peaks. The  $g$ -values of all annealed devices of sample 1 provide a value close to 2.0055, which was also found in the reference sample. This  $g$ -value is attributed to defect A that seems to occur in both cases. The question whether it is really defect A that occurs in sample 1 can be further confirmed by performing a tilt series.

### Tilt series of the sample 1

In order to evaluate the angular dependence of the  $g$ -value of defect A, a tilt series was performed with sample 1 annealed at 350 °C for 60 min. The device was rotated from 0 – 90 ° between the [100] axis and the magnetic field B. The results of the tilt series can be found in figure 4.20.

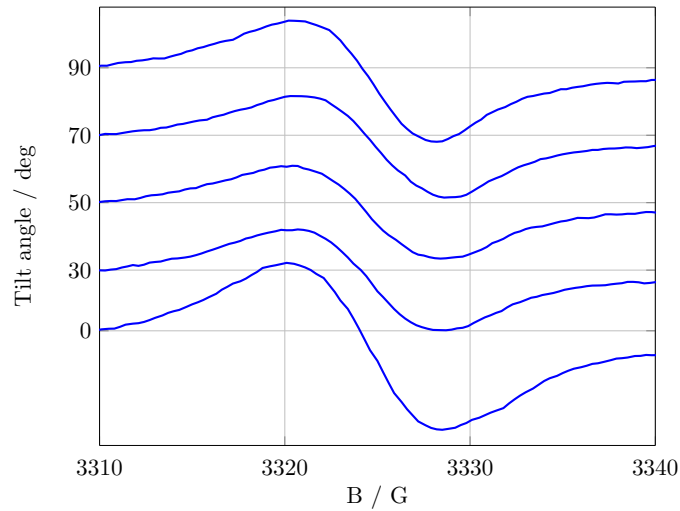


**Figure 4.20:** Tilt series of sample 1 annealed at 350 °C for 60 min. 0 deg corresponds to the [100] direction

In the EDMR signal for a tilt angle of 0 ° the shoulder peak is barely recognisable by the small deformation of the curve in the range of 3330 G. For higher tilt angles the second peak cannot be recognised anymore. Apparently, the two signals merge. This behaviour indicates that the second defect shows the same anisotropic behaviour as in the reference sample. This strengthens the presumption that it is the same defect as in the reference. The  $g$ -values that are attributed to defect A of the single curves of the tilt series are displayed in figure 4.21. From this evaluation, it becomes evident that the  $g$ -values are almost constant. This indicates an isotropic defect. Due to the  $g$ -values that are all found at about 2.0055, plus the fact that the symmetry dependence is isotropic, it is very likely that defect A is present in sample 1 as well as in the reference sample.

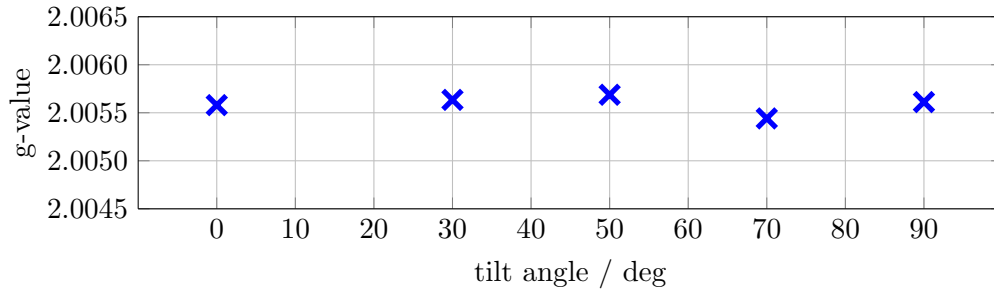


**Figure 4.21:**  $g$ -value dependence of defect A in sample 1.

### 4.3.3 Sample 2

In this section the results of the sample 2, where an implantation dose of  $10^{15}$   $\text{H}^+/\text{cm}^2$  was introduced, are presented. Featuring interesting results in the previous study on Si pn-junctions created by proton implantation [1], this sample is of particular interest. To determine the electrical characteristics of sample 2, IV-characteristics were recorded inside as well as outside the cavity as shown in figure 4.22.

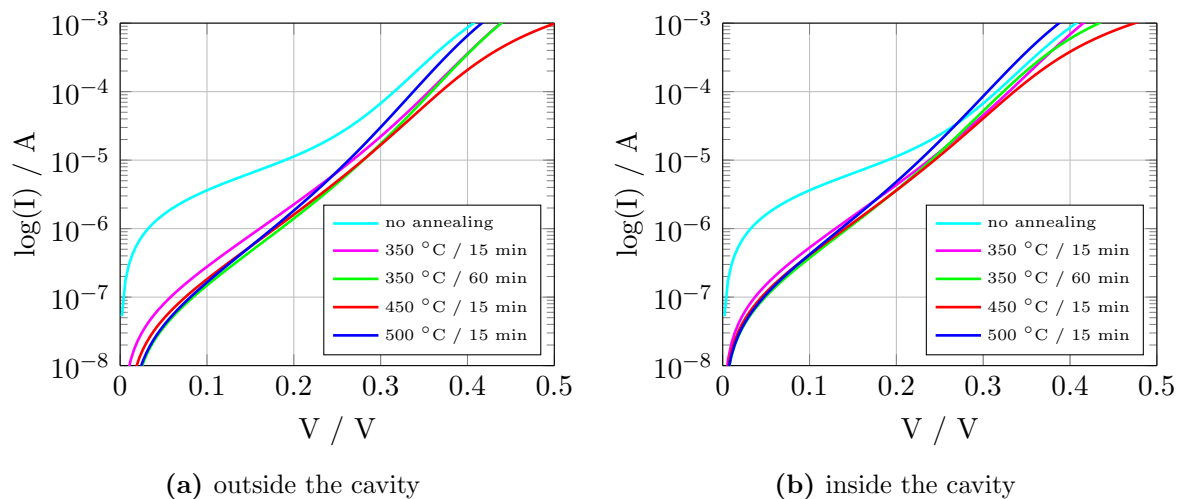


**Figure 4.22:** Logarithmic display of the IV-characteristics of sample 2 outside the cavity and inside the cavity (under measurement conditions).

The missing annealing step seems to strongly alter the electrical behaviour of the not annealed devices. By comparing the results of the IV-characteristics recorded inside and outside the cavity, a slight shift towards higher values of the curves recorded inside the cavity can be recognised. This observation is in accordance with the behaviour observed for sample 1 and the reference sample. The range for the optimal bias voltage is assumed to be between 100 mV and 300 mV. As it has already been the case in the other samples, a more accurate determination of the best biasing conditions is obtained by a voltage de-

pendent EDMR measurement. This measurement is performed with the sample annealed at 500 °C for 15 min. The applied voltages range from 85 mV up to 300 mV and 5 EDMR curves are averaged for each voltage. The result of the voltage dependent measurement is provided in figure 4.23. For the bias voltages of 155 mV and 183 mV the highest EDMR

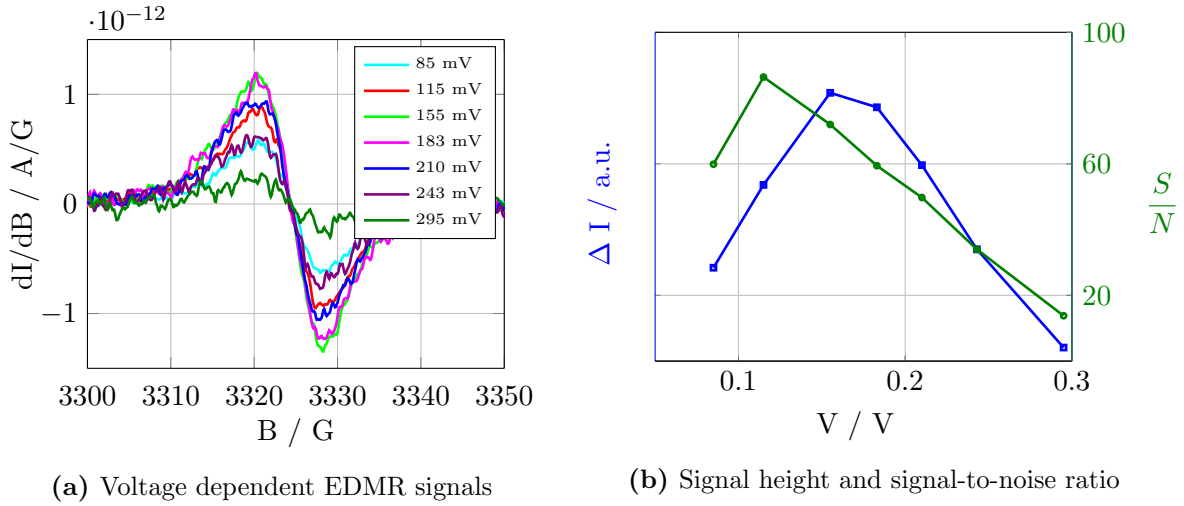


**Figure 4.23:** Dependence of EDMR signal height and signal-to-noise ratio on the bias conditions for sample 2 annealed at 500 °C for 15 min

signal can be obtained. By additionally considering the signal-to-noise ratio, the optimal bias voltage proves to be 155 mV. For this voltage a current of 5  $\mu A$  could be determined under measurement conditions. Based on this result, almost all devices of sample 2 are biased in a way to generate a current of 5  $\mu A$  through the device. Once more the exception is the not annealed device where a current of 10  $\mu A$  was found to generate the best output signal.

In figure 4.24 the EDMR results of sample 2 are presented. The EDMR results of the not annealed sample as well as the ones from the samples subjected to the four basic annealing steps are available.

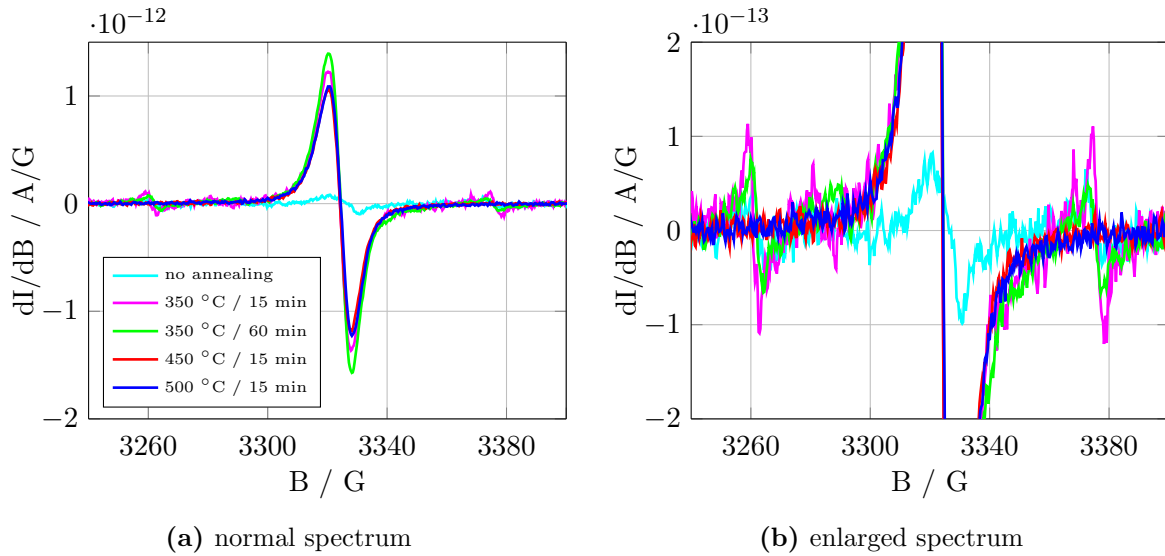


**Figure 4.24:** EDMR signals of the sample 2 subjected to the basic annealings and without annealing in a normal and enlarged representation.

Compared to the previously discussed EDMR results, sample 2 shows a richer spectrum which may be explained by the higher implantation dose. Apart from the signal in the middle of the spectrum, two signals on either side can be noticed that appear to be a doublet.

By considering the EDMR spectrum of the not annealed sample, a signal in the middle of the spectrum can be identified. For this signal a  $g$ -value of 2.0042(4) can be determined. Analogous to the reference sample and sample 1, this value is faulty because of the rather poor signal quality that can be achieved with this device. However, the result for the  $g$ -value matches with the analogous values obtained for the other samples. This finding strengthens the impression that the same defect is present in all not annealed samples indicated by the weak signal located in the middle of the spectra. In addition, the spectrum of the not annealed sample reveals a doublet signal with a hyperfine splitting of 114 G. With a rough estimation of the  $g$ -factor a value of 2.0088 can be determined. Sample 2 annealed at 350 °C for 15 min provides a similar spectrum although the overall intensity of the signal in the middle as well as the doublet on either side has increased. It seems reasonable to suppose that defect A also exists in sample 2, since the high signal in the middle of the spectrum is arising with the annealing step. This assumption is further strengthened by the fact that the  $g$ -value equals 2.0057(3). For the doublet, a hyperfine splitting of 115 G and a  $g$ -value of 2.0093(4) can be determined. The spectrum of the sample annealed at the same temperature of 350 °C but with a longer annealing time of 60 min provides a very similar picture. The high signal of defect A has a  $g$ -value of 2.0056(3) and the doublet delivers a  $g$ -value of 2.0091(4). The hyperfine splitting remains constant. In the spectrum of the sample annealed at 450 °C the doublet is not recognisable

anymore. Apparently, the defect generating the doublet is disappearing in a temperature range between 350 °C and 450 °C. Whether this defect dissolves or it transforms into another defect species that is simply not electrically active anymore remains uncertain. In order to determine the temperature range where the doublet disappears more accurately, a further investigation was performed. Its results are presented in the following section. To complete the interpretation of the EDMR spectra in figure 4.24 the sample annealed at 500 °C for 15 min has to be discussed. As expected, the doublet is not present anymore and the signal of defect A provides a  $g$ -value of 2.0056(3).

To sum up these results, a defect is already present before the annealing revealing a  $g$ -value of 2.0042. More importantly, a doublet is observed in the not annealed sample as well as in the samples annealed at 350 °C. For this doublet a  $g$ -value of about 2.0092(4) can be assigned with a hyperfine splitting of 115 G. The emergence of a doublet is traced back to the presence of a spin  $\frac{1}{2}$  atom. Hydrogen atoms exhibit a nuclear spin of  $\frac{1}{2}$  and since sample 2 has been implanted with a high dose of protons it can be assumed that this doublet is caused by a defect related to hydrogen. The doublet vanishes for annealing temperatures of 450 °C and 500 °C.

### **Evolution of the doublet**

In order to limit the temperature region where it comes to the disappearance of the doublet, a more extensive investigation was performed. As evident from the EDMR results displayed in figure 4.24 the doublet is already present without the annealing. It is detectable until a temperature of at least 350 °C. By comparing the EDMR results of the samples annealed for 15 min and 60 min at this temperature no significant difference can be observed. At a temperature of 450 °C the doublet is not recognisable anymore. For this reason it is the temperature range between 350 °C and 450 °C that has to be examined in more detail. Accordingly, three additional annealing steps (375 °C, 400 °C, 425 °C) were applied to sample 2 for 15 min each. The subsequently performed EDMR measurements provide the results presented in figure 4.25. As can be seen from this figure the doublet is also visible for 375 °C and 400 °C, but then vanishes for an annealing temperature of 425 °C. In figure 4.26 an enlarged representation of the doublet development in the course of the different annealing steps is provided.

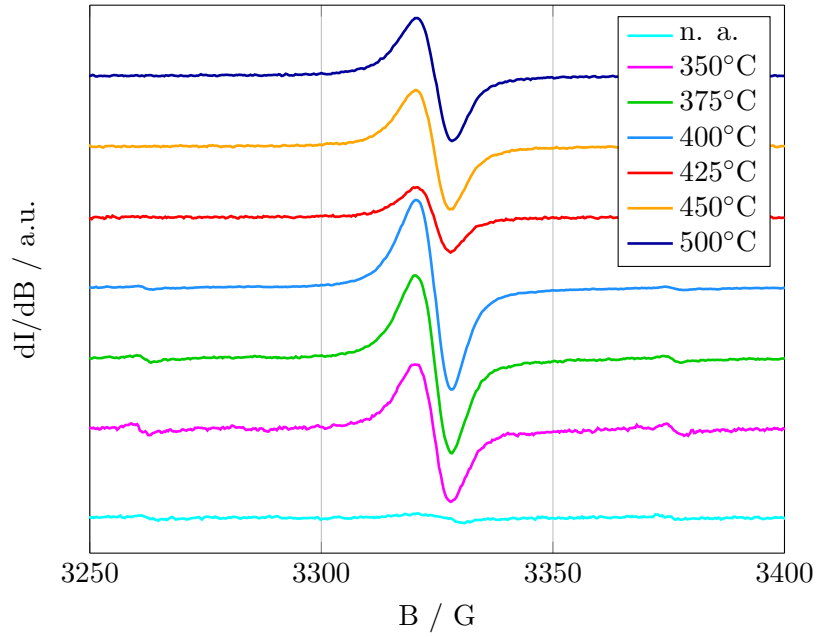


**Figure 4.25:** EDMR results of the annealing sequence applied to sample 2 to determine the evolution of the doublet.

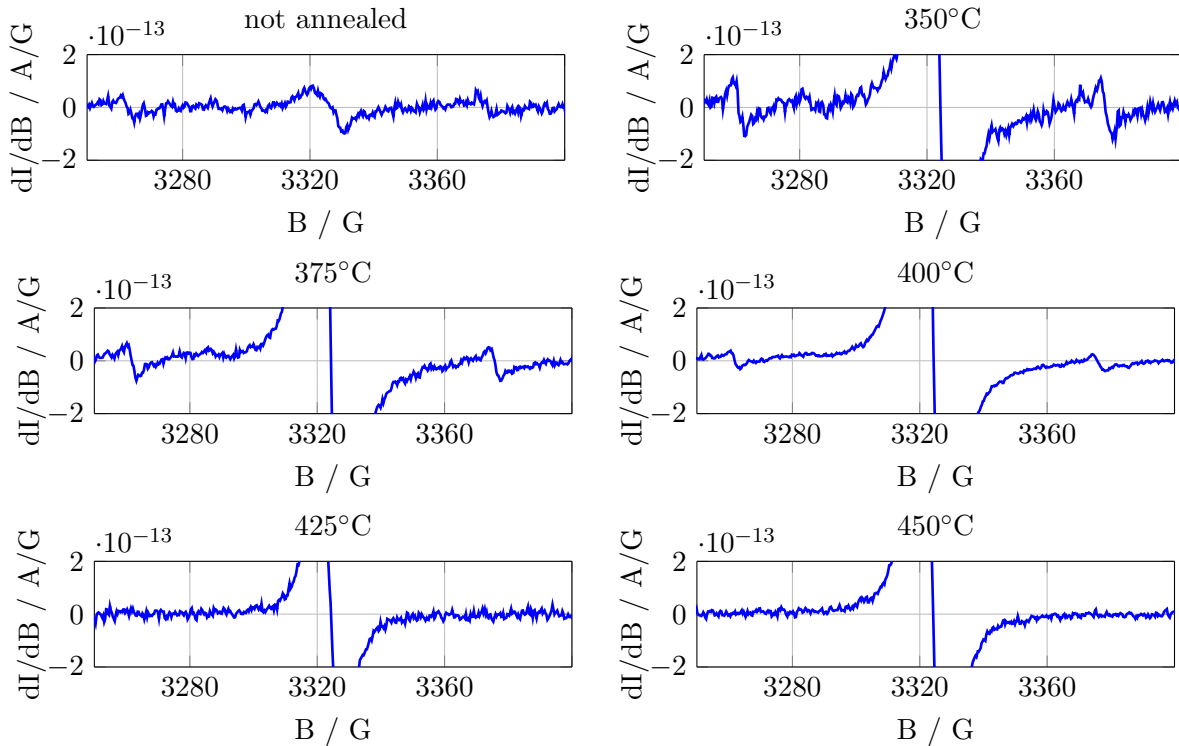


**Figure 4.26:** EDMR results of the annealing sequence applied to sample 2 in order to determine the evolution of the doublet in an enlarged representation.

Figure 4.26 illustrates that the intensity of the doublet seems to be highest for 350 °C. At 375 °C and 400 °C the doublet is still clearly visible, however, the intensity seems to decrease. Finally, for an annealing of 425 °C, no doublet signal can be observed which also applies for the 450 °C. Following this examination, it becomes clear that the vanishing of the doublet signal can be specified to a temperature range around 425 °C. Taking these results into consideration, it may be conceivable that the doublet is really hydrogen correlated whereby the hydrogen starts to diffuse or leak out of the material at temperatures above 400 °C. As a result, the defect complex may dissociate and is therefore not detectable with EDMR anymore. However, as these are just unconfirmed and vague assumptions, more information on the doublet associated defect has to be gained to strengthen these presumptions. In order to quantify the development of the doublet signal in the course of the different annealing temperatures, the associated recombination current is determined for each annealing step where the doublet is visible. In figure 4.27 the result is provided. The results for the individual recombination currents are all normalised to the value obtained for the sample annealed at 350 °C for 15 min. Unfortunately, the data from the not annealed curve could not be evaluated properly due to the poor quality of the signal.

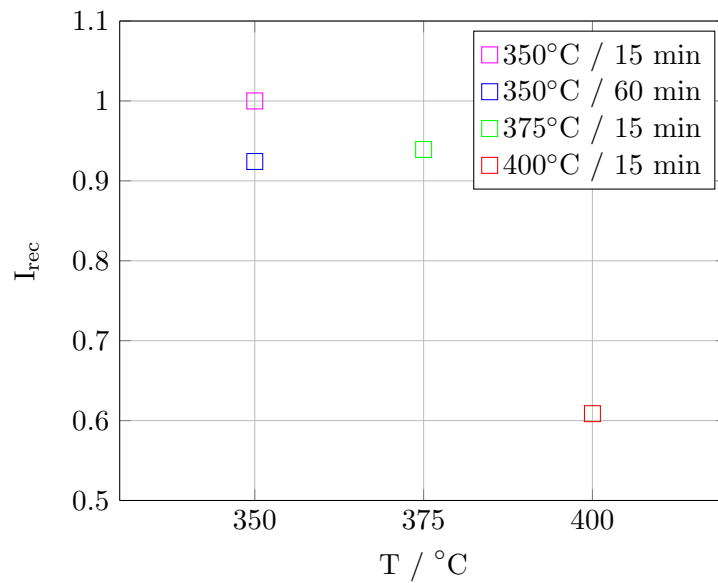


**Figure 4.27:** Recombination current corresponding to the doublet in sample 2 depending on the annealing parameters. All values for the recombination current have been normalised to the value for the sample annealed at 350 °C for 15 min.

The impression already gained by figure 4.26 is confirmed by the results of the recombination current analysis. The signal of the doublet appears to be the highest for an annealing at 350 °C and then decreases with higher temperatures. The reason why a longer annealing time for the same temperature (350 °C) leads to a decrease of the dou-

blet signal cannot be explained. However, it is just one sample that has been annealed and measured with these parameters. Nothing is known about the scattering range of these results and therefore it would be necessary to measure more samples with the same annealing parameters to ensure a reasonable statistical evaluation. From the results in figure 4.27 only a trend can be deduced.

In order to correlate the two appearing signals in the spectra of sample 2 with each other, the doublet signal (D) is normalised in relation to the signal in the middle (defect A). Subsequently, the resulting ratios are plotted in terms of the annealing parameters. In figure 4.28 the results are illustrated. It is unfortunately not possible to compare the EDMR results of different annealing temperatures with each other because nothing is known about the particular recombination efficiencies of the observed defects. It has to be recalled that the recombination efficiency is highest for defects located in the middle of the band gap. Nonetheless, also defects that are located higher or lower than the middle of the band gap contribute to the recombination current but with a lower efficiency. This lower efficiency results in a smaller EDMR signal. Therefore, it cannot be concluded that a lower EDMR signal automatically means that less of the defect is present. It could mean that this defect is simply less effective in the recombination process.

However, by comparing 4.27 with 4.28 the same dependences can be observed. According to this observation, it may be assumed that in the investigated temperature range (350 °C - 400 °C) the concentration of defect A remains almost constant while the concentration of the doublet is decreasing with higher annealing temperatures.

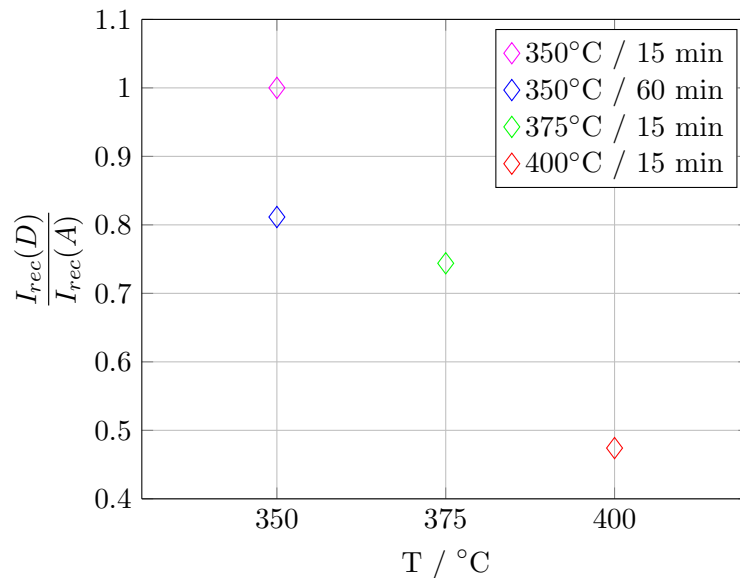


**Figure 4.28:** Ratio of recombination currents of defect A and the doublet in terms of the annealing parameters. All ratios have been normalised to the ratio for the sample annealed at 350 °C for 15 min.

### Tilt series sample 2

A tilt series of sample 2 was performed in order to get a better understanding of the doublet signal as well as to monitor the signal in the middle of the spectrum. The sample investigated under rotation was annealed at 350 °C for 60 min. The angles range from 0-90° between the [100] axis and the magnetic field B. The whole tilt series is presented in figure 4.29. A second representation 4.29b of the tilt series is provided where the signal in the middle has been cut out. Thereby the small features of the EDMR spectra can be displayed in more detail.

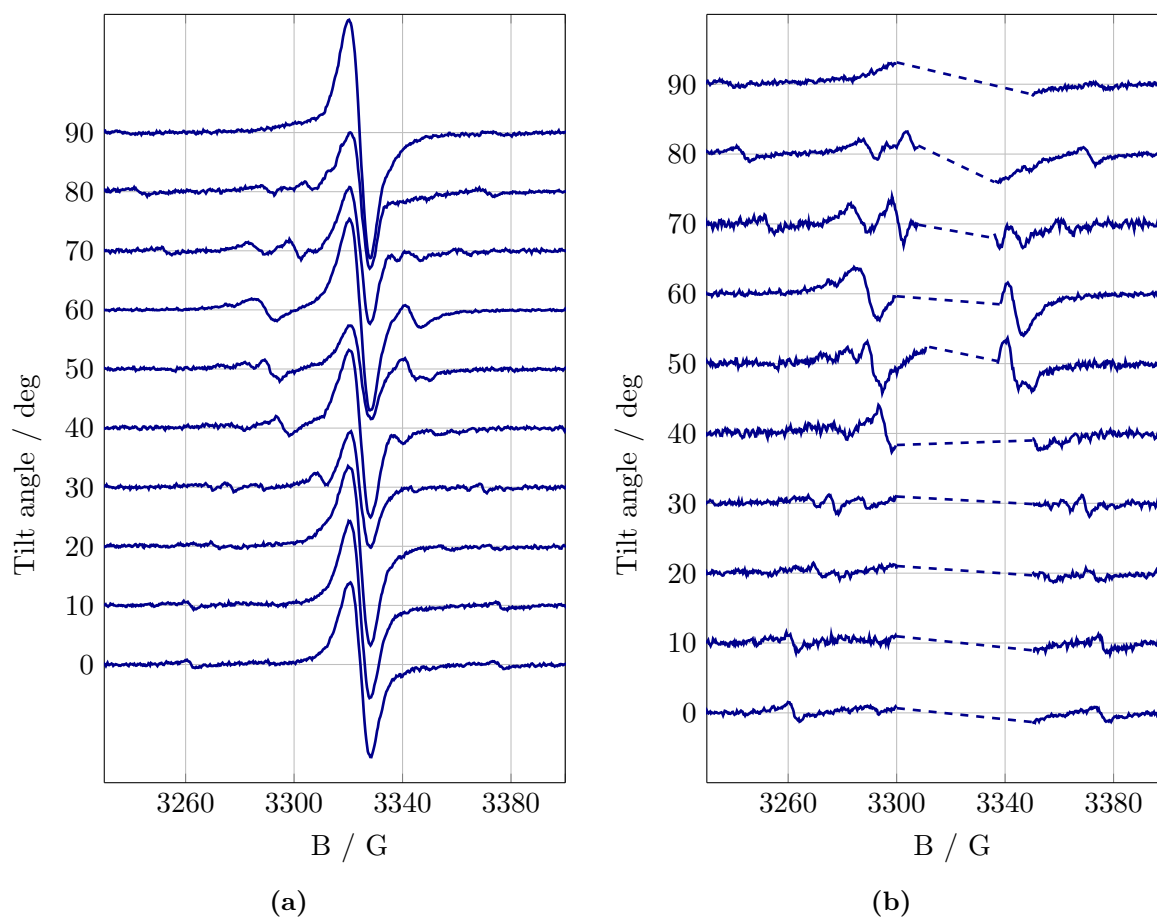


**Figure 4.29:** Tilt series of sample 2 annealed at 350 °C for 60 min. 0 deg corresponds to the [100] direction. In the left figure the whole tilt series is shown. In the right figure the tilt series without the signal in the middle is provided to show the side features in more detail.

The first outcome that follows from this tilt series is that a defect with an isotropic symmetry dependence in the middle of the spectrum is also present in sample 2. Thus, there is a strong suspicion that it is the same signal and thereby defect that has already been observed in the reference sample and in sample 1, namely defect A. By evaluating the  $g$ -values of each rotation angle this impression can be confirmed. All  $g$ -values are

found to be around a value of 2.0055 as it was the case for the analogues evaluation of the tilt series of sample 1 and the reference sample. The  $g$ -values for the respective rotation angles can be found in figure 4.30.

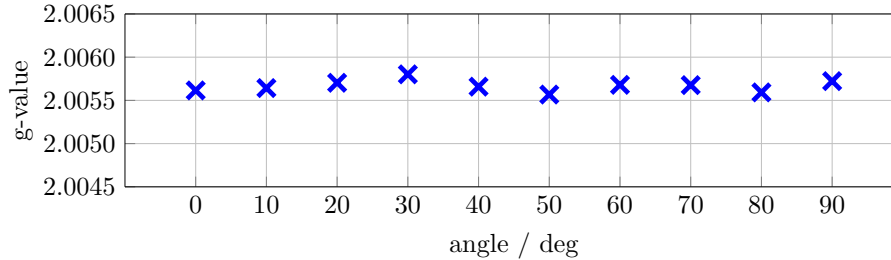


**Figure 4.30:**  $g$ -value dependence of defect A in sample 2.

By considering the behaviour of the doublet under rotation, a further interesting feature can be observed. The doublet shows some strongly anisotropic hyperfine interaction and apparently shifts towards the centre of the spectrum. For  $0^\circ$  and  $10^\circ$  no significant change can be noticed. However, for angles between  $20^\circ$  and  $90^\circ$  the doublet is not traceable anymore since many more features arise in the spectrum. It appears as if there were actually more defects present that are simply not detectable under  $0^\circ$  rotation. Unfortunately, the resolution of the spectra in the tilt series is not high enough to receive clearly resolved peaks for all angles. Whether all the features observed belong to the doublet that was detected in the standard EDMR measurement or if they indicate the presence of further defects remains uncertain. However, it is known that the doublet disappears for annealing temperatures around  $425^\circ\text{C}$ . It is therefore reasonable to perform a further tilt series with sample 2 annealed at a higher temperature to see whether or not the additional features also disappear. For this purpose the sample annealed at  $450^\circ\text{C}$  for 15 min is measured under four different tilt angles. The resulting tilt series is illustrated in figure 4.31. In the tilt series of sample 2 annealed at  $450^\circ\text{C}$ , only four different rotation angles were investigated due to time reasons. However, the tilt angles of  $30^\circ$ ,  $50^\circ$  and  $70^\circ$  are suitable for a comparison between the spectra of both samples. In contrast to the tilt series in figure 4.29 where many features were clearly visible at these angles, they are not recognisable in the tilt series of the higher annealed sample anymore. Following this finding, it can be probably assumed that all signals that occur under rotation in sample 2 annealed at  $350^\circ\text{C}$  belong to the doublet related defect. A further possible explanation would be that the signals observed under the rotation do not belong to the doublet but rather exhibit a similar annealing behaviour. Thus, they are also gone at  $450^\circ\text{C}$ .

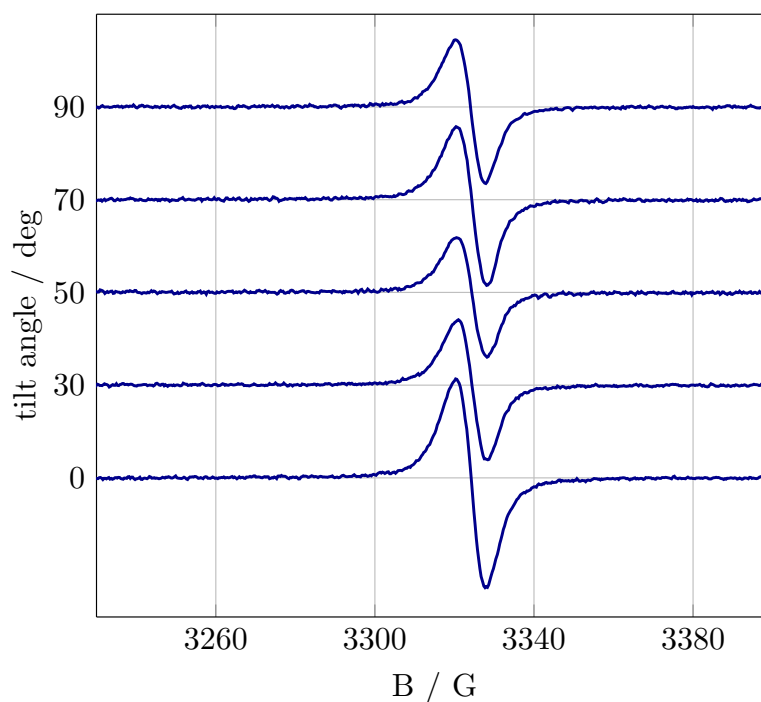


**Figure 4.31:** Tilt series of sample 2 annealed at 450 °C for 15 min. 0 deg corresponds to the [100] direction

#### Emergence of defect A in sample 2

In sample 2 a high EDMR signal can be obtained with a  $g$ -value of about 2.0055 that seems to arise with temperature. This signal also occurs in the spectra of the reference sample as well as in sample 1. For the reference sample it was found that the signal of defect A arises at a temperature of about 325 °C. In order to determine the temperature where this signal occurs in sample 2 more precisely, a more extensive annealing study was carried out. For this reason, additional annealing steps were applied to sample 2 between 200 °C and 350 °C. The resulting EDMR signals are displayed in figure 4.32 together with the EDMR signals that have been recorded before. It is the region of interest in the middle of the spectrum that is displayed exclusively.

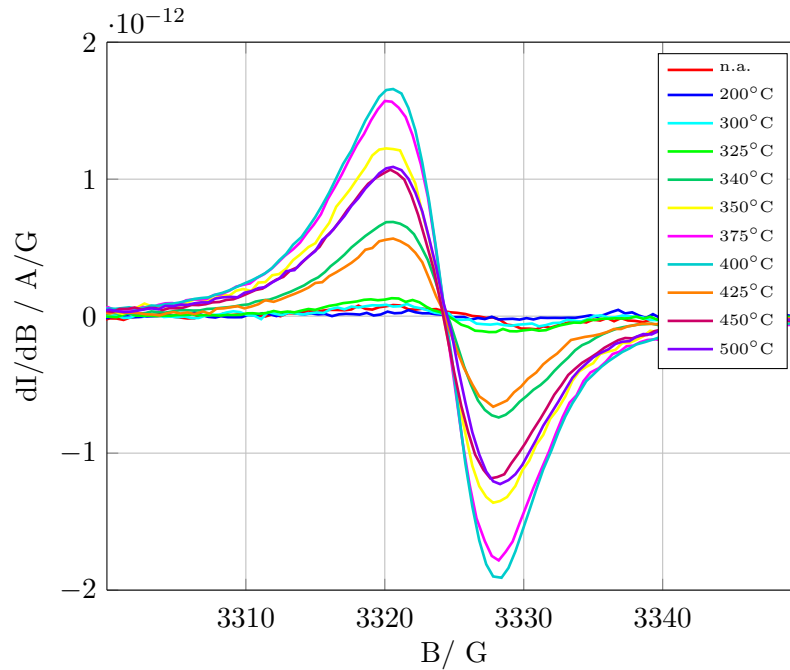


**Figure 4.32:** EDMR spectra of sample 2 for various annealing steps to determine the emergence of defect A

All signals in figure 4.32 were integrated twice to obtain the corresponding recombination currents. The first annealing step, where a reasonable result for the recombination current could be observed, was at a temperature of 300 °C. For the annealing steps below this temperature no clear EDMR signal could be obtained. In order to analyse the development of the EDMR signal in the course of the annealing sequence, a display of the recombination currents received, in terms of the annealing parameters is presented in figure 4.33. All values have been normalised to the recombination current result of the annealing temperature of 350 °C. According to figure 4.33 the EDMR signal of defect A arises between 325 °C and 340 °C. This finding is in accordance with the result of the reference sample where the increase of the signal of defect A was specified to a temperature range around 325 °C as well. The signal appears to be the highest for an annealing of 400 °C and subsequently drops. The result of the sample annealed at 400 °C that is explicitly lower than the others does not really fit into the dependence observed. It seems unlikely that the concentration of a defect firstly grows, then suddenly drops to a much lower value and finally increases again with increasing annealing temperatures. It is more likely that the result of the sample annealed at 400 °C represents an outlier. A more accurate statistical analysis would be necessary to give a reasonable statement on the development of defect A under different annealing temperatures.

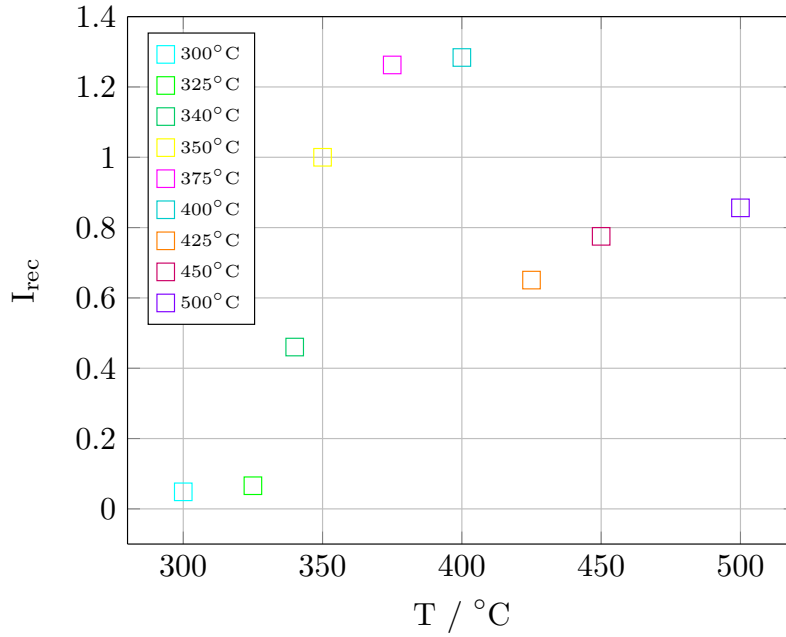


**Figure 4.33:** Recombination currents corresponding to sample 2 annealed at various annealing temperatures. All values for the recombination current have been normalised to the result for the sample annealed at 350 °C for 15 min.

Summing up the essential findings from the investigation of sample 2, there is one defect present in the device that has not been annealed. The  $g$ -value of this defect can be determined to a value of 2.0042. As it was the case in sample 1 and the reference sample there is a defect arising with the annealing exhibiting a  $g$ -value of about 2.0055. On the basis of the tilt series an isotropic symmetry behaviour for this defect could be determined. These results leave little doubt that it is actually defect A that also exists in sample 2. In addition to defect A, a doublet is recognisable in sample 2 which is probably a hydrogen related defect. On the basis of the implementation of a more extensive annealing sequence it could be determined that the doublet disappears for temperatures around 425 °C. In the tilt series it could be observed, that under angles different than 0 °C many more features can be obtained in the EDMR spectra. Unfortunately, it cannot be stated whether these features belong to the doublet related defect or not even though they also seem to disappear in the same temperature range as the doublet.

#### 4.4 Discussion of electrical characteristics

To supplement the EDMR results presented in the previous sections, IV-characteristics of each device were determined in the course of this study. It was found that there is a difference in the IV-curves depending on whether they were recorded outside the resonator cavity or inside the cavity, thus under measuring conditions. A slight shift of the curves towards higher values was observed for the IV-characteristics recorded inside the cavity. Under measuring conditions the diodes in the cavity are exposed to a magnetic field on the one hand, and to microwave radiation on the other hand. As an influence of the magnetic field on the IV-curves could not be determined, an influence of the microwave radiation on the diode characteristic is supposed. Diodes can rectify an alternating signal and thereby it is conceivable that the microwave radiation in the cavity is rectified by the diodes leading to an enhanced current through the device. In order to examine and further investigate this assumption in more detail, several IV-curves were recorded at different microwave power settings. In all samples that were investigated the same behaviour could be determined. Therefore, only the result of one sample is presented in this context to illustrate the essential findings. Sample 1 annealed at 350 °C for 60 min serves as an example to present the outcome. According to figure 4.34, there is

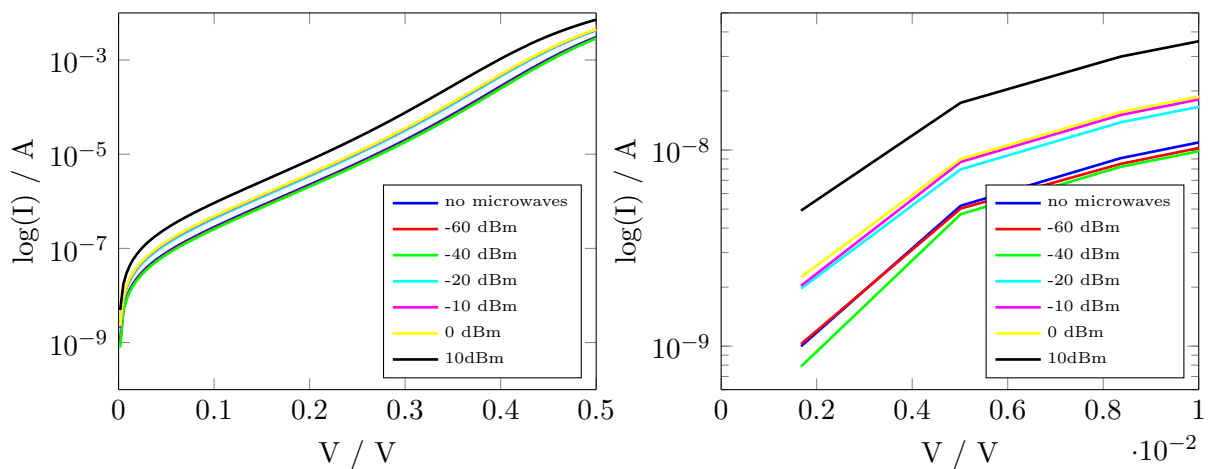


**Figure 4.34:** IV characteristics of sample 1 annealed at 350 °C for 60 min in a normal as well as in an enlarged representation.

in fact a dependence of the IV-curves on the microwave power settings. The IV-curves recorded without microwaves and with low microwave power settings (-60 dBm and -40 dB) do not greatly differ from each other. However, a jump in the electrical characteristics can be observed when the microwave power is set to a value of -20 dBm. Subsequently, the IV-curves remain almost constant (-10 dBm, 0 dBm) until a further jump can be noticed for a microwave power of 10 dBm. A rectification effect would be apparent if a

current through the device can be measured at zero bias voltage. Unfortunately, due to the sensitivity by which the IV-curves were determined, no values are available at exact zero bias voltage. However, at very small forward bias voltages differences for the various power settings can be observed (see 4.34). Therefore, a rectification effect seems to be present. By considering the IV-characteristics in the reverse bias condition another effect may be present. The rectification effect does not suffice to explain the dependence of the reverse bias current on the microwave power. However, a possible temperature dependent effect could be the reason for the dependence of the leakage current on the microwave power. Following figure 4.35, a reverse saturation current dependence similar to the one

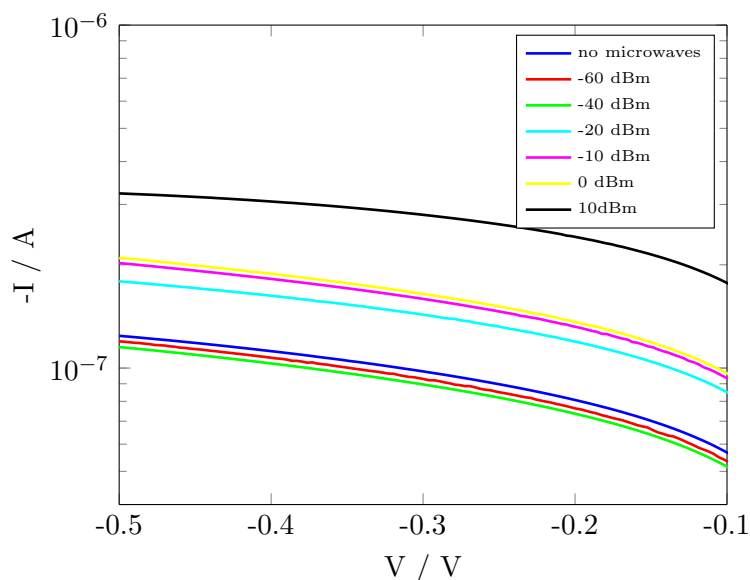


**Figure 4.35:** Logarithmic display of the reverse bias current for different microwave power settings of sample 1 annealed at 350 °C for 60 min

observed in the forward bias regime can be observed. Two jumps in the IV-curves are clearly visible and they appear at the same power settings as already discussed for the forward bias current. Therefore, it can be assumed that also the factor of temperature plays a role and influences the IV-characteristics. The higher the microwave power, the more energy is present in the cavity and as a result more heat is generated in the device.

## Discussion and Outlook

---

In this chapter, the defects that were observed by EDMR are discussed. The chapter starts with a section on the defect that exhibited the most prominent signal, namely defect A. Afterwards, the double peak structure recorded for certain annealing treatments in sample 1 and the reference sample are discussed. The final section treats the doublet signal that was observed in sample 2.

### 5.1 Defect A

In all the samples including the not implanted sample serving as a reference in this study, a strong EDMR signal arising after annealing was observed. The defect associated with this signal was termed "A". The corresponding  $g$ -value was found to be about  $g = 2.0055$  and by performing a tilt series the symmetry dependence proved to be isotropic. Interestingly, the same signal with identical properties could also be determined in the proton implanted samples, in the lower as well as in the higher implanted ones. By comparing the obtained  $g$ -values for defect A with an EPR database, where  $g$ -values of already known defects in semiconductors are listed [37], an accordance could be found, indicating that silicon dangling bonds are causing the signal corresponding to defect A. Through additional literature research it was found that signal A resembles the well-known Si dangling bond signal that has already been observed by EPR and EDMR measurements in amorphous silicon [38] [39], on single crystal silicon surfaces [32] [40], in silicon crystals damaged by mechanical stress [41], by implantation [42] and in polycrystalline silicon [43]. In addition, a  $g$ -value of 2.0055 with an isotropic behaviour could be determined in EDMR measurements on silicon diodes [35] [44] [45] [46] [30] and moreover in a  $n$ -

channel metal oxide field effect transistor [47]. The origin of the isotropic  $g = 2.0055$  signal has been generally accepted as recombination centres being silicon dangling bonds that are either embedded in an amorphous matrix or located on the silicon surface or at an interface. Furthermore, vacancy clusters are supposed to be a source of dangling bonds in the bulk of the material that can act as recombination centres. However, at first glance this picture does not apply to the pn-junctions that were investigated in this work. The occurrence of vacancy clusters would indeed be conceivable in the proton implanted samples where a high defect and thereby vacancy concentration was introduced, but since the signal also appears in the not implanted device the vacancy cluster approach remains unlikely. Beyond that, it is the depletion region of the diodes that is probed in EDMR measurements, which is entirely composed of a crystalline Si lattice, just varying in the respective doping concentrations. Therefore, no interface or surfaces states should be basically involved. A further interesting aspect regarding defect A is the fact that in the previous EDMR study on the identical samples performed by Gernot Gruber [1], no such signal was obtained neither in the implanted, nor in the not implanted samples. Apparently, defect A has been formed in the time period between the two scientific works where the samples were simply stored in the laboratory without specified conditions. In the course of the considerations made to identify the origin of defect A in the samples studied in this thesis, it was found that these test samples were fabricated without a proper edge termination. This means that the pn-junction extends over the whole sample size right to the edges where the sample terminates with a native oxide. This fact applies to the samples examined in the previous study by Gernot Gruber as well as to the samples investigated in the present work. Hence, this fact alone does not suffice to explain the origin of defect A as it was not detected in the previous work. However, a possible explanation for the formation of defect A could be found based on this missing edge termination. In the period of storage the samples were exposed to humidity that has probably adsorbed on the surface of the diodes. The fact that defect A could only be detected after an annealing treatment of at least  $325^{\circ}\text{C}$  leads to the assumption that thermal activation is a significant step in the formation process of defect A. Due to the annealing the adsorbed atoms or molecules may diffuse into the bulk and thereby change the composition or structure of the outer region of the diodes. In this way the edge regions may become more conductive and for this reason a larger proportion of the forward bias current flows over this edge regions. Assuming this to be the case, the silicon dangling bonds present at the interface between the silicon crystal and the native oxide would be detectable in the EDMR measurement as more of the current flows over this region. In order to verify this theory an attempt was made to restore the original conditions of the diodes as they were investigated in the previous study. On the one hand, some of the as-fabricated reference samples were newly cut with a diamond saw and on the

other hand, they were shortly dipped into a HF-solution. In both cases the intention was to remove the humidity modified oxide that is supposed to have formed over time and thereby restore the original conditions. In a further step all of these samples were annealed at 350°C for 15 min and subsequently an EDMR measurement was performed. A comparison of the resulting EDMR spectra is shown in figure 5.1.

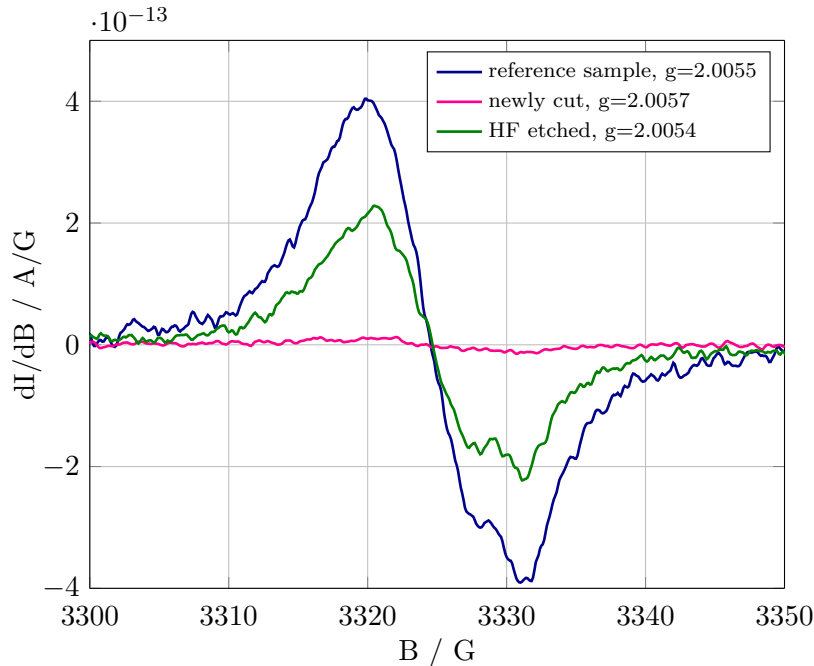


**Figure 5.1:** Comparison of the reference sample annealed at 350°C for 15 min with a newly cut and a HF etched analogous sample. The resulting  $g$ -value of each signal is indicated in the legend.

By comparing the resulting EDMR responses of the newly cut sample with the reference, a clear difference is recognisable: While in the reference sample a distinct EDMR signal with a double peak is visible, in the newly cut sample there is almost no EDMR response detectable anymore. Just a small transition with an intensity decreased by a factor of 10 can be noticed after averaging many curves. The  $g$ -value of this transition could be determined to a value of 2.0057 indicating that a small amount of defect A is probably still present. The theory that Si dangling bonds at the surface of the samples are responsible for the large EDMR signal that has been recorded in all annealed samples seems to be confirmed, at least for the reference sample. However, for a more substantial confirmation of this theory further investigations would be necessary to examine whether the large EDMR response also vanishes in newly cut devices of sample 1 and sample 2. Interestingly, by comparing the EDMR response of the etched sample with the reference, no such change can be observed. The EDMR signal of the etched sample still exhibits a high intensity signal with a  $g$ -value of 2.0054 and a double peak structure very similar to the one of

the reference. Obviously, the etching process did not really influence the EDMR response which leads to the assumption that the native oxide has not been removed properly. According to these results it can be concluded that defect A is probably a surface related defect, that could be almost removed by the formation of newly cut edges.

## **5.2 Double Peak in the reference sample and sample 1**

Besides signal A that was detected in all investigated samples some additional features could be observed in the recorded EDMR spectra. The striking similarities between sample 1 and the reference sample have to be emphasised in this context. In both samples a double peak is visible especially for the temperature of 350 °C. The existence of this additional peak leads to the assumption that at least two different defects are present in sample 1 and the reference sample. The  $g$ -values of the additional signal forming the double peak were determined to be  $g = 2.0026$  for the reference sample and  $g = 2.0028$  for sample 1. According to these results it may be supposed that the same defects are present in both samples.

The shape of the absorption line of a single defect can be approximated by using analytical formulas like lorentzian or gaussian lineshapes [26]. In the reference sample annealed at 350 °C for 60 min the double peak is clearly visible and an attempt was made to approximate this EDMR signal with the use of lorentzian derivatives. The intention of this attempt was to inspect whether it is possible to fit the obtained EDMR signal with two lorentzian derivatives according to the two assumed defects or if a larger number of lorentzian derivatives is necessary to fit the double peak signal. In figure 5.2 a sequence of fit attempts can be found ranging from a fit with one lorentzian derivative up to six lorentzian derivatives.

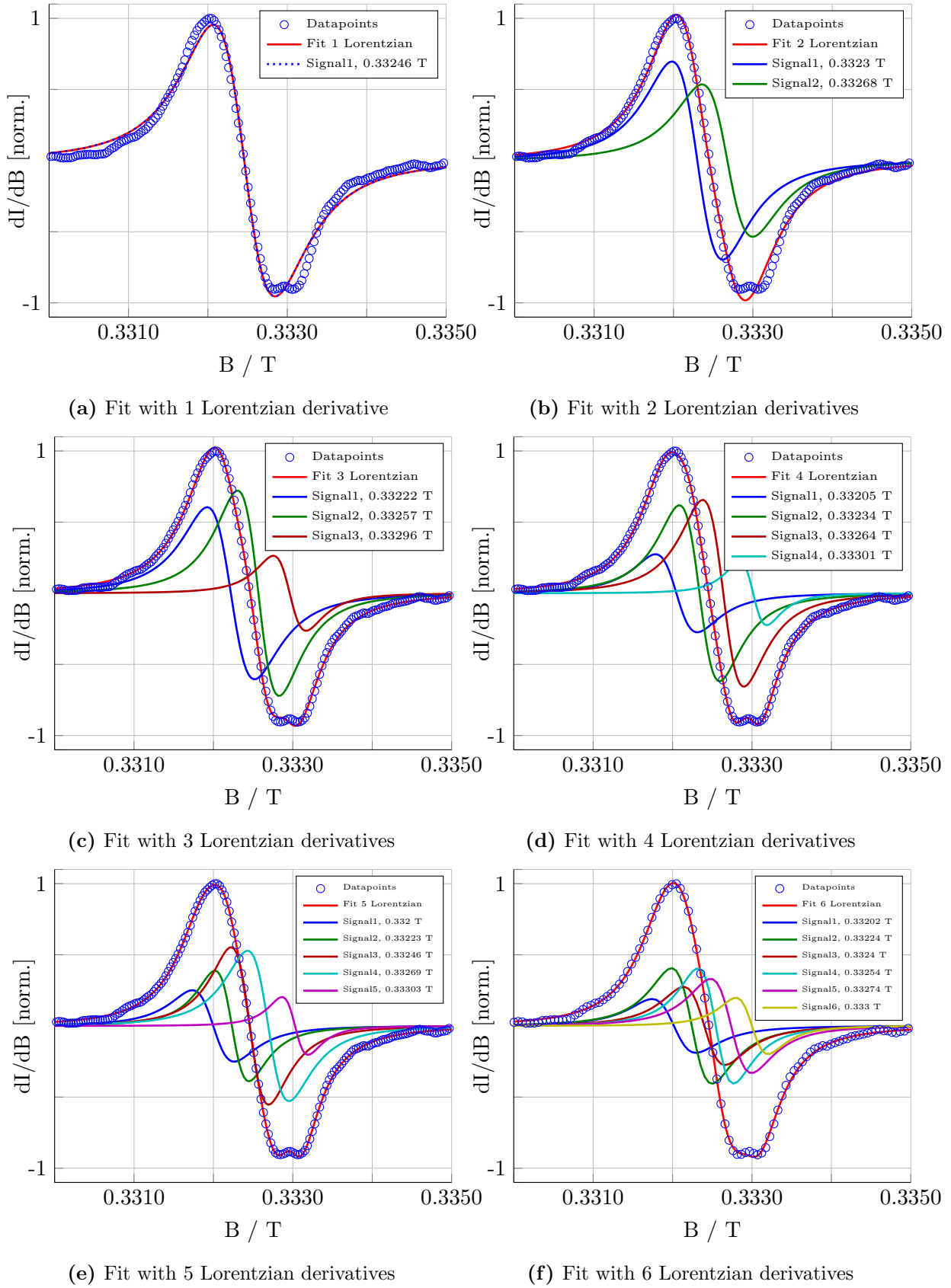
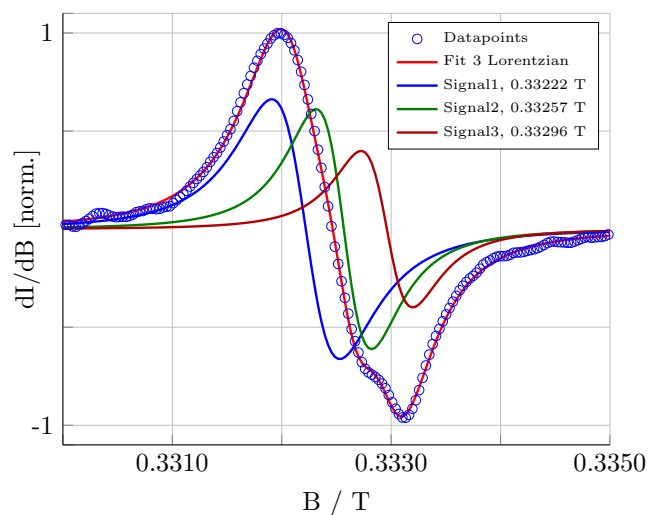


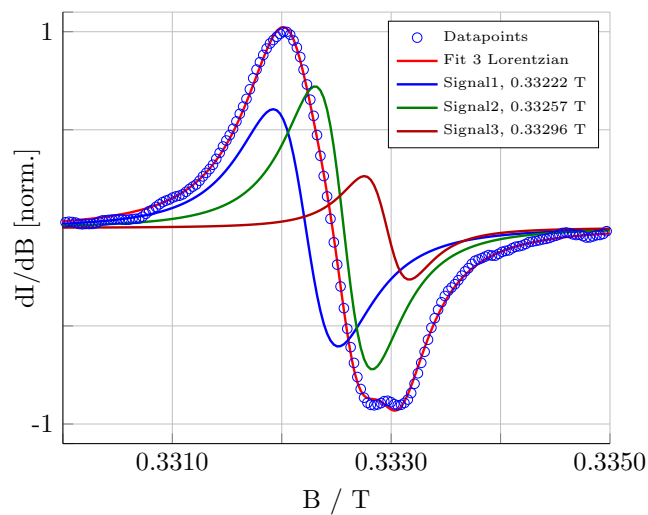
**Figure 5.2:** Fitting sequence to fit the double peak signal obtained in the reference sample annealed at 350 °C for 60 min with Lorentzian derivatives. The single Lorentzian curves as well as the resultant fit curve are displayed. In addition the zero crossings  $B_0$  of the single fit curves are indicated.

As can be seen in figure 5.2 a fit with a single lorentzian derivative does not suffice to explain the appearance of a double peak. Interestingly, also the fit with two lorentzian derivatives does not explain the double peak signal. Only when three lorentzian derivatives were used the double peak could be reproduced. For all higher numbers of fit functions the fit to the double peak improved. According to these results it is doubtful whether the spectrum can be explained by two defect peaks. However, this only holds true assuming that the observed spectra are pure lorentzian lineshapes, as assumed in the fitting model. Nonetheless it is remarkable that at least three lorentzian peaks are required to fit the spectrum.

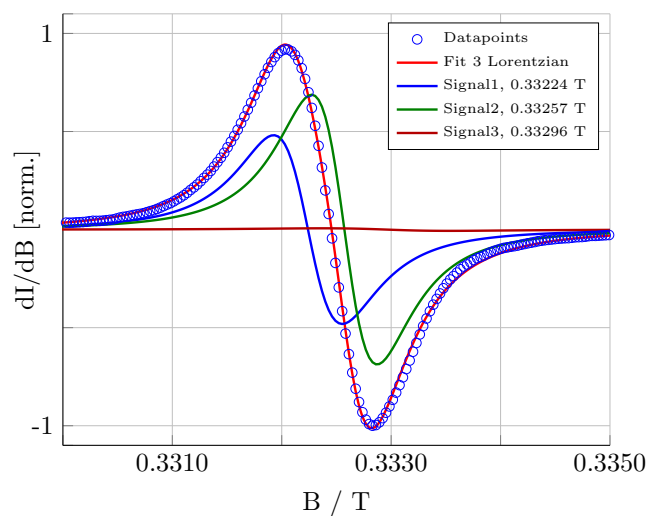
Since at least three lorentzian fit functions are required to receive a double peak, a further attempt was made to fit other EDMR signals of the reference sample with exactly these three lorentzian derivatives. Therefore, the values for the zero crossings were highly restricted to  $\Delta B_0 = 0.00001$  while the signal intensities as well as the line widths are varied in order to achieve the best possible correlation with the recorded EDMR signals. Apart from the already used reference sample annealed at 350 °C for 60 min, the fits were applied to the reference sample annealed at 350 °C for 15 min and to the one annealed at 450 °C. In figure 5.3 the resulting fit curves for the reference sample with three lorentzian derivatives can be found.



(a) 350°C for 15 min



(b) 350°C for 60 min



(c) 450°C for 15 min

**Figure 5.3:** Attempt to fit the recorded EDMR signals of the reference sample with 3 Lorentzian derivatives. The zero crossings  $B_0$  of the single fit curves are indicated.

From the results illustrated in figure 5.3 it can be concluded that the three lorentzian derivatives suffice to explain all three EDMR spectra. While in the reference samples annealed at 350 °C all three fit curves show similar intensities, the intensity of the third fit curve (red) strongly diminishes for the sample annealed at 450 °C. In table 5.1 the zero crossings for each fit curve together with the resulting  $g$ -values obtained with the resonance condition are listed. The values for the  $g$ -factor are calculated using the frequency of  $\nu = 9332$  MHz.

**Table 5.1:** Zero crossings and corresponding  $g$ -values of the three lorentzian fit curves to approximate the double peak EDMR signals of the reference samples

Sample	$B_0(1) / T$	$g$ -value(1)	$B_0(2) / T$	$g$ -value(2)	$B_0(3) / T$	$g$ -value(3)
350 °C / 15 min	0.33222	2.0070	0.33257	2.0048	0.33296	2.0025
350 °C / 60 min	0.33222	2.0070	0.33257	2.0048	0.33296	2.0025
450 °C / 15 min	0.33224	2.0068	0.33257	2.0048	0.33296	2.0025

Due to the striking similarity of the double peak signal observed in the reference sample with the one obtained in sample 1 it is assumed that the double peak has the same origin in both samples. Therefore, a further attempt was made to fit the EDMR signals of sample 1 with the same three lorentzian derivatives used in the fit of the reference sample. In order to achieve reasonable results and fit the EDMR signals of sample 1 best, the restriction of the zero crossing for each fit curve has to be slightly adjusted to a value of  $\Delta B_0 = 0.00005$ . In figure 5.4 the resulting fit curves for sample 1 with three lorentzian derivatives is illustrated.

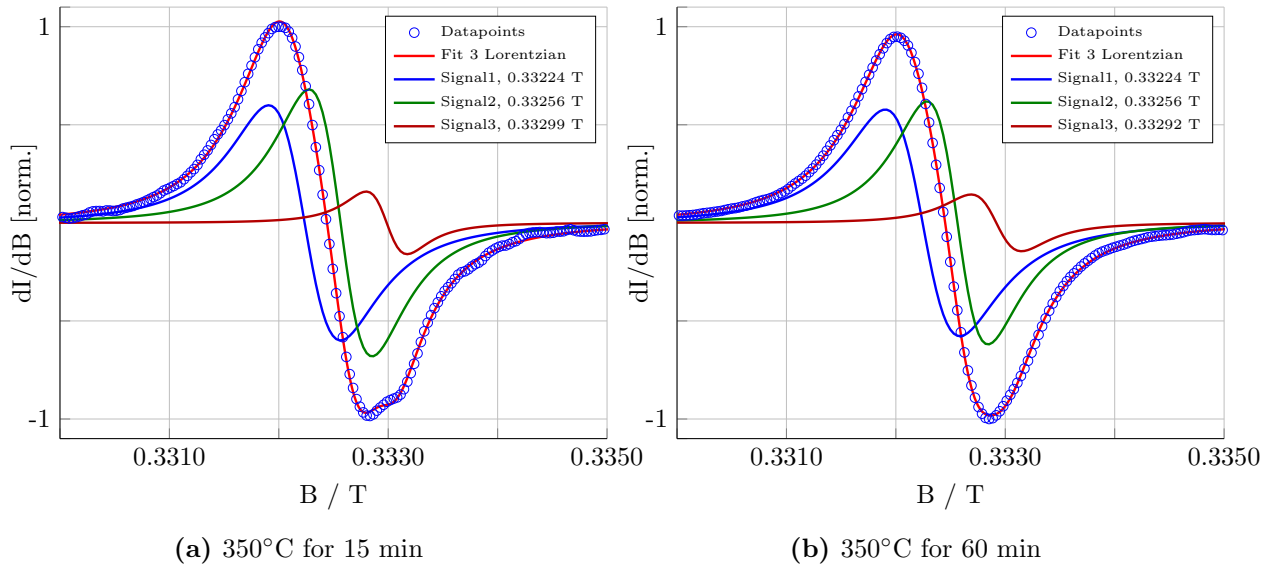


**Figure 5.4:** Attempt to fit the recorded EDMR signals from the sample 1 with 3 Lorentzian derivatives. The zero crossings  $B_0$  of the single fit curves are indicated.

As can be seen in figure 5.4, it is possible to fit the EDMR signals with the same three lorentzian derivatives used for the reference sample to a good degree. However, the zero crossings of the individual fit curves are slightly different as can be seen in table 5.2 where the zero crossings of each fit curve together with the resulting  $g$ -values are listed.

**Table 5.2:** Zero crossings and corresponding  $g$ -values of the three lorentzian fit curves to approximate the double peak EDMR signals of sample 1

Sample	$B_0(1) / T$	$g$ -value(1)	$B_0(2) / T$	$g$ -value(2)	$B_0(3) / T$	$g$ -value(3)
350 °C / 15 min	0.33224	2.0068	0.33256	2.0049	0.33299	2.0023
350 °C / 60 min	0.33224	2.0068	0.33256	2.0049	0.33292	2.0027

According to these results, it is most likely that the defects generating the double peak in the reference sample as well as in sample 1 are the same. However, the approximation of the EDMR results with the use of lorentzian derivatives is just an attempt to gain a better understanding of the EDMR signals obtained in the experiments. The fact that with three lorentzian derivatives the double peak signal can be reproduced does not necessarily mean that exactly three overlapping peaks generate the double peak. Of course it cannot be excluded that more defects participate. Future work would be needed to find out the origin of the double peak signal. One possibility to gain a better resolution of the double peak signals would be the performance of a W-band (94 GHz) EDMR measurement. Higher sensitivities as well as a better spectral resolutions can be achieved with the use of higher magnetic fields and higher microwave frequencies. It has been shown that resonance lines that remain unresolved in X-band measurements clearly separate in W-band measurements [48]. Therefore, it is very likely that also the double peak signals recorded in sample 1 and in the reference sample can be separated in a W-band measurement and in this way it would be possible to examine the resulting absorption lines in a more extensive way under W-band conditions.

### 5.3 Doublet defect

The EDMR response of sample 2 offered a richer spectrum compared to the other samples. Apart from the signal in the middle of the spectrum, two signals on either side were noticed that appear to be a doublet. The hyperfine splitting was found to be about 115 G and the  $g$ -value could be determined to a value of about  $g = 2.0092$ . The performance of a tilt series revealed many more features in the EDMR spectrum indicating that there are actually two or more doublets present changing their position and hyperfine splitting in the course of the rotation measurement. By comparing the result of the tilt series of sample 2 without the middle signal with the one performed in the previous study with a

comparable sample [1] several similarities can be noticed. Apart from the strong signal in the middle of the spectrum, the features on the sides seem to be the same. To allow for a better comparison, the data of the two tilt series are superimposed and displayed in figure 5.5.

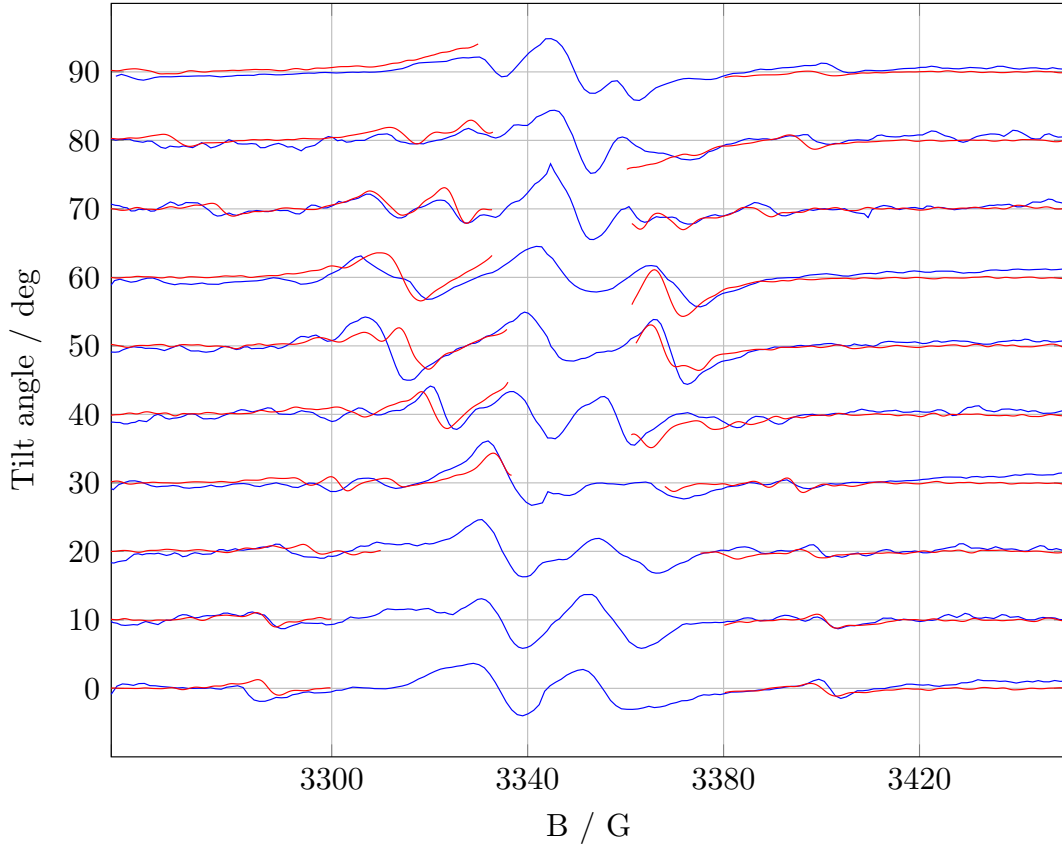


**Figure 5.5:** Comparison of the tilt series obtained for sample 2 annealed at 350°C for 60 min with the comparable tilt series published in [1]. The blue curves correspond to the results of the previous study whereas the result of the current study are indicated in red.

Even though the features do not exactly coincide they appear at almost the same magnetic fields and in addition exhibit similar shapes. In the previous study another scan coil was used where the calibration of the x-axis was not as good as in the current work. This is probably the reason for the discrepancy in the magnetic field values. It is supposed that the features visible in the middle of the spectrum of the previous tilt series (blue) are not visible in the tilt series performed in this work (red), since this region is dominated by the high intensity signal related to defect A. Therefore, it might be reasonably assumed that the defects causing the features in the EDMR spectra are the same in both cases. Already in the study of Gernot Gruber [1] the doublet signal as well as the arising additional features upon a tilt measurement were found to have a similar behaviour to defects observed by Gorelkinskii et al. [49] [50] [51]. The same statement applies to the currently recorded EDMR results. In order to obtain better resolved peaks it would be

again useful to repeat the measurements under W-band conditions.

Even though EDMR proves to be a powerful technique to investigate and characterise paramagnetic point defects within semiconductors, the interpretation of the EDMR spectra turns out to be challenging. A further way to facilitate the interpretation of the EDMR spectra and to recognise the underlying defects creating the spectrum of sample 2 under rotation would be the performance of extensive *ab initio* calculations [52].



## Conclusion

---

In the course of this study on proton implanted silicon pn-junctions, different EDMR responses could be observed for the different samples that were investigated. Changes in the EDMR spectra of the implanted samples could be determined in comparison to a not implanted sample. Obviously, the proton implantation leads to an introduction of recombination centres in the pn-junctions. Moreover, changes in the EDMR responses depending on the implantation dose as well as after different annealing treatments could be observed.

In all investigated samples, implanted as well as not implanted, a high intensity EDMR signal associated with a defect termed A was observed. The concentration of defect A increased with increasing annealing temperatures. The  $g$ -value of this defect was determined to a value of about  $g = 2.0055$  and by performing a tilt series the symmetry dependence proved to be isotropic. Because of the fact that the signal occurs in the implanted as well as not implanted devices, it must be independent of the proton implantation. The strong similarity in terms of  $g$ -value and symmetry dependence with the well-known Si dangling bond signal, leads to the assumption that signal A is related to surface defects that exist because of a missing edge termination.

A strong similarity between the EDMR spectra of the not implanted sample with the EDMR spectra of the sample implanted with an implantation dose of  $10^{14} \text{ H}^+ \text{ cm}^{-2}$  could be recognised. In both samples a double peak is visible upon annealing treatments between  $350^\circ\text{C}$  and  $450^\circ\text{C}$ . Therefore, besides the signal of defect A a second defect acting as a recombination centre seems to be present in these samples. The performance of a tilt series revealed an anisotropic symmetry dependence of this second defect and the  $g$ -values could be determined to  $g = 2.0026$  in the reference sample and  $g = 2.0028$  in the implanted sample. However, a more detailed analysis of the EDMR spectra led to the

conclusion that at least three different defects generate the double peak signal, making a clear interpretation difficult.

The sample implanted with an implantation dose of  $10^{15} \text{ H}^+ \text{ cm}^{-2}$  exhibited a richer EDMR spectrum compared to the other investigated samples. Apart from the signal of defect A, two additional EDMR signals could be detected appearing to be a doublet. The hyperfine splitting of the doublet signal was determined to be 115 G and the  $g$ -factor has a value of 2.0093(2). This doublet signal was found to disappear at annealing temperatures higher than  $400^\circ\text{C}$  and there is a strong suspicion that the underlying defect is hydrogen related. The performance of a tilt series revealed even more features that are very likely related to the doublet signal, as the same annealing temperature dependence could be observed for these features. Unfortunately, no clear identification of the defects causing the multiple EDMR response could be attained. However, these defects are most likely hydrogen-related.

In all not annealed samples, in the implanted as well as not implanted ones, a small and rather vague EDMR signal with  $g$ -values between 2.0042 and 2.0045 could be obtained. These results indicate the presence of the same defect in all three types of devices, thus independent of the proton implantation. However, no further statement can be made on the nature of this defect as the poor signal quality does not allow for a more detailed and accurate investigation of this defect with EDMR. The not annealed samples generally showed a weaker signal compared to the annealed ones combined with a much worse signal-to-noise ratio. In addition, the not annealed samples clearly differed from the annealed samples in terms of IV-characteristics and SRP profiles. It can be concluded that the unannealed samples have a much lower concentration of EDMR relevant defects and that the defects first form after the anneal.

Even though EDMR is a powerful technique to investigate and characterise paramagnetic point defects within semiconductors, the interpretation of the EDMR spectra turned out to be challenging. One way to facilitate the interpretation would be the performance of *ab initio* calculations where the defect symmetry as well as the hyperfine structure are used to identify the defects. Furthermore, the measurement of the proton implanted samples with other defect investigating techniques like SRP or DLTS (deep level transient spectroscopy) would be a quite useful supplement in order to extend the possibilities to identify defects.

# CHAPTER 7

## Appendix

### 7.1 Measuring parameters

**Table 7.1:** Measuring parameters of sample 1.

$I_{magnet}$ ...current through magnet,  $U_{bias}$ ...forward bias voltage,  $I_{forward}$ ...forward bias current,  $B_{mod}$ ...magnetic field modulation for lock-in detection, S1...sensitivity setting at pre-amplifier, S2...sensitivity setting at lock-in detector,  $f_{mod}$ ...modulation frequency of reference signal, phase...phase setting at lock-in detector, f...microwave frequency, P...microwave power, StN...signal-to-noise ratio, n...number of averaged curves,  $B_0$ ...zero crossing

	n. a.	350°C 15 min	350°C 60 min	450°C 15 min	500°C 15 min
$I_{magnet}$ / A	25.6	25.6	25.6	25.6	25.6
$U_{bias}$ / mV	80	155	163	157	150
$I_{forward}$ / $\mu$ A	10	5	5	5	5
$B_{mod}$ / G	3	3	3	3	3
S1 / nAV <sup>-1</sup>	100	100	100	100	100
S2 / $\mu$ V(10V) <sup>-1</sup>	500	200	200	500	200
$f_{mod}$ / Hz	900	900	900	900	900
phase / °	-136	-136	-136	-136	-136
f / MHz	9331.83	9332.62	9331.658	9332.066	9331.824
P / dBm	0	0	0	0	0
StN	13	207	378	238	227
$\Delta I/I$	1.96e-08	3.00e-07	4.95e-07	7.12e-07	4.82e-07
n	52	96	106	16	131
g-value (1)	2.0044	2.0056	2.0056	2.0057	2.0056
$B_0$ (1) / G	3326.4	3324.6	3324.4	3324.3	3324.5
g-value (2)		2.0028			
$B_0$ (2) / G		3329.1			

**Table 7.2:** Measuring parameters of the reference sample.  
 $I_{magnet}$ ...current through magnet,  $U_{bias}$ ...forward bias voltage,  $I_{forward}$ ...forward bias current,  $B_{mod}$ ...magnetic field modulation for lock-in detection,  $S1$ ...sensitivity setting at pre-amplifier,  $S2$ ...sensitivity setting at lock-in detector,  $f_{mod}$ ...modulation frequency of reference signal, phase...phase setting at lock-in detector,  $f$ ...microwave frequency,  $P$ ...microwave power,  $StN$ ...signal-to-noise ratio,  $n$ ...number of averaged curves,  $B_0$ ...zero crossing

	n. a.	350°C 15 min	350°C 60 min	450°C 15 min	500°C 15 min	400°C 15 min	200°C 15 min	300°C 15 min	325°C 15 min	335°C 15 min
$I_{magnet} / A$	25.6	25.6	25.6	25.6	25.6	26.22	26.34	26.34	26.34	26.22
$U_{bias} / mV$	92	155	150	157	157	200	181	184	186	191
$I_{forward} / \mu A$	5	5	5	5	5	5	5	5	5	5
$B_{mod} / G$	3	3	3	3	3	3	3	3	3	3
$S1 / nAV^{-1}$	100	100	100	100	100	100	100	100	100	100
$S2 / \mu V(10V)^{-1}$	200	200	200	500	200	200	200	200	200	500
$f_{mod} / Hz$	900	900	900	900	900	900	900	900	900	900
phase / °	-136	-136	-136	-136	-136	-136	-136	-136	-136	-136
$f / MHz$	9332.286	9332.880	9331.620	9331.806	9331.812	9332.852	9332.514	9332.494	9332.356	9332.484
$P / dBm$	0	0	0	0	0	0	0	0	0	0
$StN$	136	91	104	403	329	65	10	18	46	33
$\Delta I/I$	2.85e-08	1.59e-07	1.95e-07	3.00e-07	6.03e-07	1.91e-07	1.36e-08	3.24e-08	5.36e-08	3.59e-08
$n$	117	74	50	85	70	102	100	65	326	290
g-value (1)	2.0045	2.0055	2.0055	2.0056	2.0057	2.0055	2.0052	2.0053	2.0052	2.0055
$B_0$ (1) / G	3326.4	3324.9	3324.5	3324.4	3324.3	3325	3325.3	3325.1	3325.1	3324.8
g-value (2)		2.0026	2.0026							
$B_0$ (2) / G		3329.4	3329.4							

**Table 7.3:** Measuring parameters of sample 2.

$I_{magnet}$ ...current through magnet,  $U_{bias}$ ...forward bias voltage,  $I_{forward}$ ...forward bias current,  $B_{mod}$ ...magnetic field modulation for lock-in detection, S1...sensitivity setting at pre-amplifier, S2...sensitivity setting at lock-in detector,  $f_{mod}$ ...modulation frequency of reference signal, phase...phase setting at lock-in detector, f...microwave frequency, P...microwave power, StN...signal-to-noise ratio, n...number of averaged curves,  $B_0$ ...zero crossing

	n. a.	350°C 15 min	350°C 60 min	450°C 15 min	500°C 15 min	400°C 15 min	375°C 15 min	425°C 15 min	200°C 15 min	300°C 15 min	325°C 15 min	340°C 15 min
$I_{magnet}$ / A	25.6	25.6	25.6	25.6	25.6	25.6	25.6	25.55	26.22	26.22	26.22	26.22
$U_{bias}$ / mV	140	190	163	175	155	178	178	222	167	183	188	212
$I_{forward}$ / $\mu$ A	20	5	5	5	5	5	5	5	5	5	5	5
$B_{mod}$ / G	3	3	3	3	3	3	3	3	3	3	3	3
S1 / nAV <sup>-1</sup>	100	100	100	100	100	100	100	100	100	100	100	100
S2 / $\mu(10V)^{-1}$	500	200	200	1000	200	200	200	100	200	200	200	200
$f_{mod}$ / Hz	900	900	900	900	900	900	900	900	900	900	900	900
phase / °	-136	-136	-136	-136	-136	-136	-136	-136	-136	-136	-136	-136
f / MHz	9331.522	9332.516	9332	9331.914	9331.94	9332.848	9333.062	9333.05	9332.142	9332.36	9332.55	9332.752
P / dBm	0	0	0	0	0	0	0	0	0	0	0	0
StN	16	175	376	296	343	772	366	103	7	12	22	52
$\Delta I/I$	9.06e-09	5.18e-07	5.93e-07	4.51e-07	4.64e-07	7.16e-07	6.71e-07	2.46e-07	1.65e-08	3.27e-08	5.10e-08	2.86e-07
n	113	22	92	75	88	334	81	80	92	57	267	430
g-value (1)	2.0042	2.0057	2.0056	2.0057	2.0056	2.0056	2.0057	2.0057	-	2.0053	2.0055	2.0056
$B_0$ (1)	3326.5	3324.5	3324.4	3324.1	3324.5	3324.7	3324.7	3324.7	-	3325	3324.8	3324.8
g-value (2)		2.0093	2.0091			2.0090	2.0091					



---

## Bibliography

---

- [1] G. GRUBER, S. KIRNSTOETTER, P. HADLEY, M. KOCH, T. AICHINGER, H. SCHULZE, W. SCHUSTEREDER. Electrically detected magnetic resonance study on defects in Si pn-junctions created by proton implantation. *physica status solidi (c)* **11** (2014) 1593
- [2] P. HAZDRA, K. BRAND, J. RUBE, J. VOBECK. Local lifetime control by light ion irradiation: impact on blocking capability of power PiN diode. *Microelectronics Journal* **32** (2001) 449
- [3] Y. ZOHTA, Y. OHMURA, M. KANAZAWA. Shallow donor state produced by proton bombardment of silicon. *Japanese Journal of Applied Physics* **10** (1971) 532
- [4] S. ROMANI, J. EVANS. Platelet defects in hydrogen implanted silicon. *Nuclear Instruments and Methods in Physics Research Section B: Beam Interactions with Materials and Atoms* **44** (1990) 313
- [5] J. Z. HU, L. D. MERKLE, C. S. MENONI, I. L. SPAIN. Crystal data for high-pressure phases of silicon. *Phys. Rev. B* **34** (1986) 4679
- [6] P. PICHLER. *Intrinsic Point Defects, Impurities, and Their Diffusion in Silicon*. Computational Microelectronics. Springer Vienna, 2012
- [7] G. GOTTSTEIN. *Physikalische Grundlagen der Materialkunde*. Springer-Lehrbuch. Springer Berlin Heidelberg, 2013
- [8] G. SCHUMICKI, N. BÜNDGENS, P. SEEGBRECHT, T. EVELBAUER, H. FEHLING, J. FOCK, J. FRICK, R. SCHNEIDER, B. STRYCHARCZYK, F. ZIMMERMANN. *Prozesstechnologie: Fertigungsverfahren für integrierte MOS-Schaltungen*. Mikroelektronik. Springer Berlin Heidelberg, 2013
- [9] R. HULL. *Properties of crystalline silicon*. 20. IET, 1999

- [10] J. CZOCHRALSKI. Ein neues Verfahren zur Messung der Kristallisationsgeschwindigkeit der Metalle. *Z. phys. Chemie.* **92** (1918) 219
- [11] H. THEUERER. Method of processing semiconductive materials, 1962. US Patent 3,060,123  
<https://www.google.com/patents/US3060123>
- [12] M. MOLL. *Radiation damage in silicon particle detectors*. Dissertation, University of Hamburg, 1999
- [13] K. SUMINO, H. HARADA, I. YONENAGA. The origin of the difference in the mechanical strengths of Czochralski-grown silicon and float-zone-grown silicon. *Japanese Journal of Applied Physics* **19** (1980) L49
- [14] R. MAZUR, D. DICKEY. A spreading resistance technique for resistivity measurements on silicon. *Journal of the electrochemical society* **113** (1966) 255
- [15] J. LAVEN. *Protonendotierung von Silizium: Untersuchung und Modellierung protoneninduzierter Dotierungsprofile in Silizium*. Springer Fachmedien Wiesbaden, 2014
- [16] C. FULLER, J. DITZENBERGER, N. HANNAY, E. BUEHLER. Resistivity changes in silicon single crystals induced by heat treatment. *Acta Metallurgica* **3** (1955) 97
- [17] H. J. STEIN, S. K. HAHN. Hydrogen accelerated thermal donor formation in Czochralski silicon. *Applied Physics Letters* **56** (1990) 63
- [18] R. WILLARDSON, E. WEBER, A. BEER, F. SHIMURA. *Oxygen in Silicon*. Semiconductors and Semimetals. Elsevier Science, 1994
- [19] G. H. SCHWUTTKE, K. BRACK, E. F. GOREY, A. KAHAN, L. F. LOWE. Resistivity and annealing properties of implanted Si:H<sup>+</sup>. *Radiation Effects* **6** (1970) 103
- [20] S. SZE, K. NG. *Physics of Semiconductor Devices*. Wiley, 2006
- [21] V. PALANKOVSKI. Shockley-Read-Hall and Surface Recombination, 2001. [Online; accessed 5-July-2016]  
<http://www.iue.tuwien.ac.at/phd/palankovski/node53.html>
- [22] H. RYSSEL, I. RUGE. *Ion Implantation* John Wiley & Sons, 1986
- [23] <https://de.wikipedia.org/wiki/Ionenimplantation>. [Online; accessed 14-July-2016]
- [24] E. ZAVOISKY. Spin-magnetic resonance in paramagnetics. *J Phys USSR* **9** (1945) 211

- 
- [25] C. C. LO. *Electrical detection of spin-dependent transport in silicon*. Dissertation, Citeseer, 2011
- [26] J. WEIL, J. BOLTON. *Electron Paramagnetic Resonance: Elementary Theory and Practical Applications*. Wiley, 2007
- [27] A. LUND, S. SHIMADA, M. SHIOTANI. *Principles and Applications of ESR Spectroscopy*. Principles and Applications of ESR Spectroscopy. Springer, 2011
- [28] M. STUTZMANN, M. S. BRANDT, M. W. BAYERL. Spin-dependent processes in amorphous and microcrystalline silicon: a survey. *Journal of non-crystalline solids* **266** (2000) 1
- [29] Stanford Research Systems. *MODEL SR830 DSP Lock-In Amplifier*
- [30] T. WIMBAUER, K. ITO, Y. MOCHIZUKI, M. HORIKAWA, T. KITANO, M. BRANDT, M. STUTZMANN. Defects in planar Si pn junctions studied with electrically detected magnetic resonance. *Applied Physics Letters* **76** (2000) 2280
- [31] C. COCHRANE, P. LENAHAN, A. LELIS. An electrically detected magnetic resonance study of performance limiting defects in SiC metal oxide semiconductor field effect transistors. *Journal of Applied Physics* **109** (2011) 014506
- [32] D. J. LEPINE. Spin-Dependent Recombination on Silicon Surface. *Phys. Rev. B* **6** (1972) 436.  
DOI: 10.1103/PhysRevB.6.436
- [33] KAPLAN, D., SOLOMON, I., MOTT, N.F. Explanation of the large spin-dependent recombination effect in semiconductors. *J. Physique Lett.* **39** (1978) 51
- [34] A. BARABANOV, O. TRETIAK, V. L'VOV. Complete theoretical analysis of the Kaplan-Solomon-Mott mechanism of spin-dependent recombination in semiconductors. *Physical Review B* **54** (1996) 2571
- [35] I. SOLOMON. Spin-dependent recombination in a silicon p-n junction. *Solid State Communications* **20** (1976) 215
- [36] J. KRZYTEK, A. SIENKIEWICZ, L. PARDI, L. BRUNEL. DPPH as a Standard for High-Field EPR. *Journal of Magnetic Resonance* **125** (1997) 207
- [37] EPR in Semiconductors, Spin-Hamiltonian parameter database for defects in semiconductors, 2016  
<http://www.kc.tsukuba.ac.jp/div-media/epr/inplist.php?category=Si>

- [38] T. UMEDA, S. YAMASAKI, J. ISOYA, K. TANAKA. Electron-spin-resonance center of dangling bonds in undoped a-Si:H. *Physical review B* **59** (1999) 4849
- [39] M. BRODSKY, *et al.* Electron spin resonance in amorphous silicon, germanium, and silicon carbide. *Physical Review Letters* **23** (1969) 581
- [40] D. HANEMAN. Electron paramagnetic resonance from clean single-crystal cleavage surfaces of silicon. *Physical Review* **170** (1968) 705
- [41] G. WALTERS, T. ESTLE. Paramagnetic resonance of defects introduced near the surface of solids by mechanical damage. *Journal of Applied Physics* **32** (1961) 1854
- [42] K. BROWER, W. BEEZHOLD. Electron paramagnetic resonance of the lattice damage in oxygen-implanted silicon. *Journal of Applied Physics* **43** (1972) 3499
- [43] W. SCHUBERT, P. LENAHAN. Spin dependent trapping in a polycrystalline silicon integrated circuit resistor. *Applied Physics Letters* **43** (1983) 497
- [44] B. STICH, S. GRUELICH-WEBER, J.-M. SPAETH, H. OVERHOF. Electrically detected electron paramagnetic resonance of a deep recombination centre in a silicon diode. *Semiconductor science and technology* **8** (1993) 1385
- [45] Z. XIONG, D. MILLER. Identification of the common electrically detected magnetic resonance signal from a Si diode. *Journal of applied physics* **78** (1995) 4895
- [46] F. RONG, E. POINDEXTER, M. HARMATZ, W. BUCHWALD, G. GERARDI. Electrically detected magnetic resonance in pn junction diodes. *Solid state communications* **76** (1990) 1083
- [47] T. UMEDA, Y. MOCHIZUKI, K. OKONOJI, K. HAMADA. Electrically detected magnetic resonance of ion-implantation damage centers in silicon large-scale integrated circuits. *Journal of applied physics* **94** (2003) 7105
- [48] V. LANG, C. LO, R. GEORGE, S. LYON, J. BOKOR, T. SCHENKEL, A. ARDAVAN, J. MORTON. Electrically detected magnetic resonance in a W-band microwave cavity. *Review of Scientific Instruments* **82** (2011) 034704
- [49] Y. V. GORELKINSKII, N. NEVINNYI. Electron paramagnetic resonance of hydrogen in silicon. *Physica B: Condensed Matter* **170** (1991) 155
- [50] Y. V. GORELKINSKII, N. NEVINNYI. EPR of interstitial hydrogen in silicon: Uniaxial stress experiments. *Materials Science and Engineering: B* **36** (1996) 133
- [51] Y. V. GORELKINSKII, N. NEVINNYI. Low-symmetry EPR center in hydrogen-implanted silicon. *Physics Letters A* **99** (1983) 117

- [52] J. COTTOM, G. GRUBER, P. HADLEY, M. KOCH, G. POBEGEN, T. AICHINGER, A. SHLUGER. Recombination centers in 4H-SiC investigated by electrically detected magnetic resonance and ab initio modeling. *Journal of Applied Physics* **119** (2016) 181507